ABSTRACT

Title of Dissertation: MAGNETIC NANOPARTICLE INKS FOR SYRINGE PRINTABLE INDUCTORS

Rebecca Fedderwitz, Doctor of Philosophy, 2023

Dissertation directed by: Professor & Chair, Peter Kofinas, Chemical and Biomolecular Engineering

Direct Ink Writing (DIW) additive manufacturing (AM) has the transformative potential to construct complex shapes and devices with a single apparatus by exchanging the printable material at the print head. Iron cobalt (FeCo), permalloy ($Ni_{80}Fe_{20}$), and iron (II, III) oxide ($Fe_2O_3 \cdot FeO$) nanoparticles with varying magnetic properties were incorporated in resins to explore the influence of particle loading on printability and inductor device performance. It was generally found that increasing particle loading increased ink viscosity, with a loading maximum approaching 29 – 42 vol% depending on the particle type and resin mixtures due to differences in particle shape and size and resin viscosity. With more magnetic content, composites had higher magnetic permeability and inductance. Syringe printable, colloidal, aqueous magnetic inks were made using both stabilized iron oxide and MnZn doped ferrite nanoparticles with added free polymers. MnZn-doped ferrite inks are printed into toroids, sintered to improve magnetic permeability and mechanical robustness, and constructed into an inductor device. Inductors with high magnetic permalloy nanoparticle content were also syringe printed into toroids and hand-wound to demonstrate their viability in fabricating three-dimensional inductors. The effect of particle size on stability and printability was observed. The research presented in this thesis investigates various methods for formulating magnetic nanoparticle inks and evaluates the contributions of particle stabilization, free polymer content, solvent composition, and particle loading on the rheological behavior required for syringe printing. Material properties and device performances were characterized using methods such as zeta potential and settling studies to observe particle functionalization and stability, rheology to study viscoelastic flow behavior, and vector network analysis to measure inductance and device efficiency to showcase the viability of this technique to manufacture passive electronic devices.

MAGNETIC NANOPARTICLE INKS FOR SYRINGE PRINTABLE INDUCTORS

by

Rebecca Fedderwitz

Dissertation submitted to the Faculty of the Graduate School of the
University of Maryland, College Park, in partial fulfillment
of the requirements for the degree of
Doctor of Philosophy
2023

Advisory Committee:
Professor Peter Kofinas, Chair
Associate Professor Siddhartha Das
Professor Srinivasa Raghavan
Professor Robert Briber
Associate Professor Isabel Lloyd
Associate Professor Luz Martinez-Miranda

Acknowledgments

I would like to thank my advisor Dr. Peter Kofinas for seeing something in me at the beginning of my graduate research journey and then for his patience, guidance, and dedication to my success throughout.

I would like to thank my committee and the weekly group meeting for their listening ears and advice, scientific or otherwise. Thank you to my lab mates for their companionship in the lab and to the undergraduate students who worked on my project with me for letting me practice mentorship.

I would also like to thank the Printed Hybrid Electronics group at the Laboratory of Physical Sciences for providing me with my research scope and trusting me with their expensive equipment, especially Jason and Donghun who never seemed to be bothered by my countless questions.

Thank you to my classmates who supported me through difficult classwork, research strife, and all the other aspects of life. Thank you to my friends and family who encouraged me even if they didn’t know what I was talking about. Thank you to all my therapists who provided me with the tools to cope when the experiments didn’t go as planned.

Thank you to my parents, who taught me to try hard but were always there for me even if it didn’t work out. And thanks to Abi, who has been right by my side through everything.

Table of Contents

List of Tables

List of Figures

Chapter 1: Introduction

1.1 Broader Impacts

To maximize the storage capabilities of an inductor, a magnetic core is included within the coils. The motivation for this research is to utilize additive manufacturing to create a magnetic core in an appropriate geometry at small scales (within a few mm). Printing magnetic inks has been a challenge, especially when it comes to the percentage of magnetic material within the final printed product. Mixing magnetic particles within a thermoplastic filament requires a large percentage of polymer to retain desirable flow properties for printing. Adding magnetic particles in a curable resin increases the viscosity of the ink and limits the particle loading. Creating a high-density magnetic nanoparticle ink for an additive manufacturing system, especially for the application of high-frequency inductors, has not yet been extensively explored. Easily printed, shape-retentive AM of highly concentrated ceramic nanoparticle solutions has been demonstrated for syringe systems. The transference of ceramic material to another type of material, namely metallic and magnetic nanoparticles, will allow the fabrication of complex shaped and nonconformal prints that can be applied to electronic devices.

The intricate and complex shapes possible through additive manufacturing (AM) facilitate the tailoring of parts to the desired application. The ability to do shape iterations leads to the rapid development and optimization of a prototype. This simplified fabrication process, especially for direct ink writing (DIW) was the capability of allowing the exchange of materials at the print head, giving the potential to enable the creation of parts on demand, even in remote, supply-limited locations. Simplifying additive manufacturing technology will increase accessibility and opportunity for creative problem-solving from end users of different backgrounds and perspectives. The ability to expand this technique to magnetic materials will accelerate material discovery and advancement to produce passive electronics, increasing the speed of communication in electronics to keep up with the current integrated circuit advancements.

The rapid material development of integrated circuit technologies to nanometer dimensions has allowed operating frequencies to approach THz, as the operating frequency is inversely proportional to device size. Such high-frequency circuits allow for improved optical fiber communications in television broadcasting, automotive radar and sensor communications, personal radio services such as Wi-Fi and Bluetooth, satellite communication such as GPS, military targeting and tracking, and inter-space satellite communications. As operating frequencies increase, circuit topology requires a design change, affecting the technology generation, type, size, and bias current of all the passive components. Magnetic devices such as inductors, transformers, and transistors have operating frequencies inversely proportional to their size. As the demand for higher operating frequencies increases, so does the demand for smaller components.

An important consideration of device fabrication is to maximize operating bandwidth and efficiency while minimizing power consumption and component size and cost, which means choosing circuit components with low loss at targeted frequencies. A common additively manufactured inductor geometry is the planar spiral due to its easy two-dimensional fabrication. The operating frequency (f_R) of an inductor is inversely proportional to the product of its inductance (L) and capacitance (C) ($f_R = \frac{1}{\sqrt{LC}}$). While a high value of inductance is necessary for increased energy storage, the capacitance must be minimized to maintain low loss. The insulating substrate is largely responsible for capacitive behavior; hence a planar geometry increases the capacitive losses and ultimately decreases operating frequency. A more suitable geometry is one that is oriented away from the substrate instead of directly in contact with it, which can be easily fabricated using three-dimensional AM technologies.

1.2 Intellectual Merit

AM has the potential to construct complex shapes using a single apparatus by exchanging the printable material at the print head, simplifying the fabrication process and making this technology accessible to the end user at any physical location. Formulating printable magnetic inks has been a challenge, especially when trying to make a final product with high particle content. Previous efforts to additively manufacture electronic devices containing magnetic composite materials have required a large weight fraction of polymeric material to provide mechanical integrity at the cost of a reduced volume fraction of magnetic material and inferior device performance. Colloidal stabilization of the magnetic nanoparticles using particle coatings enables the fabrication of an ink with tunable rheological behavior that allows the printed part to retain its shape after extrusion with minimal organic additives, maximizing its magnetic content. This technique has been successful for dense ceramic and silver suspensions. This research aims to enable its transition to the fabrication of AM electronic devices with magnetic components.

Though research on colloidal printing of ceramic nanoparticle inks is robust, the colloidal printing of metal nanoparticles – specifically magnetic nanoparticle inks – is nascent to the field. Further insight into the extent of particle stability and degree of flocculation or agglomeration within a magnetic nanoparticle ink allows deliberate rheology control to enable printing easily extrudable through a fine-tipped nozzle, retaining its shape after deposition and solvent evaporation. Dynamic light scattering and sediment measurements will be used to quantify order within the ink.

Demonstrating printable inks of varying particle types, sizes, stabilization methods, and ink components will illustrate the interrelationship between the degree of flocculation and optimal print while understanding the influence of ink composition on magnetic properties and device performance. Understanding the fundamental mechanism of what constitutes a successful, syringe-printable magnetic ink will allow this technique to span across several classes of electronic devices.

1.3 Significance

Additive manufacturing (AM) is the creation of 3-dimensional material layer-by-layer based on a digital model. This research aims to better understand how magnetic, mechanical, and rheological properties in AM influence printed electronic device performance. This research investigates the AM of passive electronic devices with a direct write syringe printing method that takes advantage of the shear-thinning properties of a stabilized nanoparticle ink. This method is used to print magnetic elements, such as inductor cores, into customizable shapes with minimal organic additives. Magnetic nanoparticles (iron cobalt (FeCo), iron (II, III) oxide ($Fe_2O_3 \cdot FeO$), MnZn doped ferrite, and permalloy ($Ni_{80}Fe_{20}$)) with low hysteresis loss and high permeability of varying sizes (between 20-250 nm) are either synthesized or purchased commercially and coated with various polymers to stabilize in solution. Differing particle surface properties influence magnetic behavior, printability, and packing printable ink formation for high weight fraction nanoparticle inks. Higher magnetic material content in the composite results in a larger magnetic response and high inductance and energy storage capability. This is accomplished through a characterization of the nanoparticles' surface properties, which influence their stabilization within the ink. High particle loading affects the print properties and drying of the ink. Additionally, magnetic, mechanical, and rheological properties determine the printability of the overall device and the final inductor performance.

Magnetic nanoparticles with a rapid magnetic response and low loss are used and stabilized in water with various polymers, depending on the type of particle used. A balance of repulsive and attractive forces produced shear-thinning fluids, allowing flow through the nozzle without clogging it, and then ceasing to flow after it is deposited on the substrate. A stability map is created to determine the optimal concentration and coating behavior of the polymer on the particle surface and observe how this concentration changes with the size and metallic composition of the magnetic nanoparticle.

1.4 Project Description

AM has the transformative potential to construct complex shapes with one machine by exchanging the printable material at the print head, simplifying the fabrication process, and making this technology accessible to the consumer population in any physical location. Printing magnetic inks has been a challenge, especially when it comes to the high-volume fraction of magnetic material within the final product. More magnetic material in the composite results in a larger magnetic response and high inductance and energy storage capability of magnetic inductor cores. Previous efforts to additively manufacture magnetic composite materials have required a large weight fraction of organic material to provide mechanical integrity at the cost of a reduced volume fraction of magnetic material. Colloidal stabilization of the magnetic nanoparticles using particle coatings enables the fabrication of an ink with tunable rheological behavior that allows the printed part to retain its shape after extrusion with minimal organic additives, maximizing its magnetic content. This technique has proved successful when fabricating dense ceramic and silver suspensions, and this research aims to understand how this technique can be transferred across material classes.

Below is a summary of the direct research contributions covered in this thesis:

1. Determined the relationship between solvent pH, polymer coating, and particle surface charge on the degree of stabilization, exhibited by settling behavior and zeta potential for iron (II, III) oxide, MnZn doped ferrite, and permalloy ink systems.
2. Deciphered the role of excess polymer as a rheology modifier on ink printability and shape retention after deposition. Particle stability and ink yield stress directly affected rheology and cracking behavior, with an optimal ink composition displaying a yield stress high enough to support its weight after deposition and exhibiting minimal cracking after solvent evaporation.
3. Evaluated how the printed device composition affects the efficiency of a printed inductor. in full configuration. The magnetic cores were connected to a transmission line with printed conductive windings and characterized by a vector network analyzer to record inductance and operating frequency.

1.5 Ph.D. Thesis Organization and Research Contributions

1.5.1 Chapter 3: Inductors fabrication from mixed magnetic particles in curable resin

Iron cobalt (FeCo), permalloy ($Ni_{80}Fe_{20}$), and iron (II, III) oxide ($Fe_2O_3 \cdot FeO$) magnetic particles with varying magnetic properties were incorporated in different resins to explore the influence of particle loading on printability and inductor device performance. It was generally found that increasing particle loading increased ink viscosity, with a loading maximum approaching 29 – 42 vol% depending on the particle type and resin mixtures due to differences in particle shape and size and resin viscosity. With more magnetic particles, composites had higher magnetic saturation and permeability. Coercivity was not affected by particle loading because there was no change in crystal structure with increased particle loading. Increased particle loadings of up to 80 wt% were attainable by mixing volatile solvent into the particle-resin formulas to decrease the viscosity of the ink. Various compositions of toroids were both molded and printed and then hand-wound to investigate the influence of particle loading on inductor device performance. Generally, increasing particle loading increased inductance due to the increase in magnetic saturation and permeability. The operating frequency does decrease with particle loading due to compounding magnetic hysteresis loss. Inductors were constructed into both a toroid and a cone using 75 wt% FeCo in NEA121 to showcase the difference in behavior with core shape, showing a higher operating frequency with a conical structure due to its orientation away from the substrate minimizing stray capacitance. From these initial studies, it was of interest to explore magnetic inks with higher particle loadings to increase inductance.

1.5.2 Chapter 4: Magnetic ferrite nanoparticle inks for syringe printable inductors

In this chapter, syringe printable, colloidal magnetic inks are made using both iron oxide and MnZn doped ferrite nanoparticles by stabilizing them with poly(acrylic acid) (PAA) and adding a free polymer polyethylene oxide (PEO) of various molecular weights and glycerol to control ink viscosity and evaporation rates. Printability is further explained using complex rheology. MnZn-doped ferrite inks are printed into toroids and sintered at 1400°C to increase magnetic permeability. A sintered toroid is constructed into an inductor device and characterized using a Vector Network Analyzer (VNA), which exhibits an inductance of 4.26 μH at 8.5 MHz. This study lays out a template for ferrite inks with the potential to be fabricated into useful passive electronic devices.

1.5.3 Chapter 5: Stabilization of permalloy nanoparticles for syringe printable inductors

This chapter investigates syringe printing parts with high magnetic permalloy ($Ni_{80}Fe_{20}$) nanoparticle content (> 35 vol%). Two different metal alloy particle sizes of 250 nm and 30 nm were synthesized to observe the effect of particle size on stability. Zeta potential was measured to discern a change in surface charge after coating procedures. Settling behavior was documented to perceive the success of coating procedures on particle stability in water. Permalloy nanoparticle inks were concentrated with polyethylene oxide (PEO) to increase viscosity and glycerol to decrease evaporation rates while printing. It was found that PEO and glycerol stabilize 30 nm permalloy in addition to increasing ink viscosity. Permalloy inks were printed into toroid shapes to demonstrate their viability in fabricating three-dimensional magnetic structures and were processed into inductors that exhibited an inductance of 180 nH and 30 MHz.

Chapter 2: Background Information

2.1 Additive Manufacturing with a Focus on Direct Ink Writing (DIW)

Additive manufacturing has fewer size and shape limitations in comparison to subtractive manufacturing methods. Subtractive manufacturing involves specialized machinery that cuts away from a solid block of material, creating more waste and limiting the special resolution of fabricated parts [1]. Additive manufacturing has advantages over traditional manufacturing in rapid prototyping, complicated design, and material sustainability [1], [2]. Comparing different printing techniques that can print particles in 3-dimensional structures, stereolithography (SLA) has a high resolution and material utilization rate, but the process is complicated and takes a long time. Stereolithography techniques require vats of photopolymer resins in which particles can scatter the light required for polymerization. Filament printing uses thermoplastic filaments that can only incorporate so many particles until the integrity of the filament is compromised. Electrohydrodynamic printing (EHD) has high resolution and can print many types of materials, but the process is complex and inefficient. Powder bed fusion (PBF) has high resolution, but also is complex to prepare and is not very efficient [3]. Powder bed diffusion can print typically metal or ceramic particles; however, the bed of powder is susceptible to aging and especially when working with precious metals, can become costly. Direct ink writing (DIW) allows printing inks with various compositions and a range of ink viscosities, but its resolution is typically lower. Direct ink writing, including syringe printing, is much more versatile and introduces the possibility of multi-material extrusion on a single tool [4]. Among recently developed AM techniques, extrusion-based ones such as DIW are the most versatile due to simple printing mechanisms and low-cost fabrication processes. DIW also allows broad material selection including ceramics, metal alloys, polymers, and even edible materials [4]. Other AM technologies outside of DIW are limited in the type and particle loading of materials that can be printed.

The successes in nanomaterial development increase the possible materials used with AM, making this fabrication technique available to create a vast array of functional materials, including electronics. Particle/polymer composites enhance material properties, however, the large influence of particle loading, microstructure, and orientation means there are endless avenues of study [5]. Understanding the interaction of the nanoparticles with each other, the solvent, and the additives in the ink is pertinent because there is great potential in the tunability of parts by altering particles and their interactions. DIW filaments need to flow under shear stress and behave as a liquid during extrusion. For fabricating metal or ceramic parts at low processing temperatures, this means mixing metal or ceramic particles into a liquid solution. An inherent requirement for DIW filaments is a liquid-like flow under shear stresses present during extrusion. For low-temperature DIW fabrication of metals or ceramic parts requires a solution of these components in particle form. Methods of stabilizing particles in solutions have been in practice for hundreds of years, for example with clay and pottery. However, the desire for a shape-retentive part with shear-thinning behavior to enable 3-dimensional material fabrication from a filament extruded through a fine-tip nozzle requires very careful rheological control. The challenge then is to create a filament with high enough particle loading to develop desirable functional properties, uniformity in print, and sufficient structural strength while preventing agglomeration and clogging[6].

In the case of magnetic material, the more concentrated the inorganic material in the ink, the better the performance properties. Defined in 1998 by Sandia National Labs based on a ceramic ink system, Robocasting (another name for DIW) is a method of additively fabricating 3D structures by extruding high-density colloidal solutions consisting of typically more than 50 vol % nanoparticle content, < 1 vol % particle coatings or binder, and the remaining amount is a volatile solvent that will be removed from the final product [7]. The rheology of the colloid must lend itself to its ease of extrusion, requiring it to exhibit shear-thinning behavior, while still maintaining mechanical integrity after deposition of several layers. Robocasting allows intricate patterns to be fabricated with an automated computer-aided design (CAD) program. Alternatively, traditional printing methods such as screen-printing and inkjet printing produce features that rely on a supportive substrate [8]. However, there are hurdles to using ceramic three-dimensional (3D) printing for printing metals due to poor resolution, low printing accuracy, pore formation during burnout binders, and complex postprocessing [9].

2.2 Rheological Requirements for DIW

This specific rheological behavior is influenced by the interaction between the dominant particle forces. The particle structure’s assembly is a result of hydrophobic interactions, hydrogen bonding, and electrostatic attraction, which competes with electrostatic repulsion and solvation [10]. Inks that have decreasing viscosity with increasing shear stress are shear-thinning fluids, easily flowing through a syringe nozzle under pressure but resisting flow under low shear stresses, therefore, retaining their shape after deposition. Shear-thinning occurs because these forces are weak against applied shear stresses [11]. Particle and solvent interactions are controlled by tuning particle size and distribution and the method of stabilization by modifying the particle surface chemistry and its interactions with one another.

Interparticle forces influence suspension behavior. The degree of stabilization of solutions alters the printability of the ink and the final shape of the product after the solvent is evaporated. Important parameters of a syringe printable ink include viscosity (at shear rates experienced during printing), yield stress, and the complex shear moduli. Most inks solidify by liquid evaporation, which requires control of the liquid-to-solid rheological transition to match that of deposition. This is done by tuning the balance between repulsive, stabilizing forces and attractive networking forces within the ink solution, as well as choosing an appropriate solvent that evaporates within a reasonable time frame. Repulsive forces prevent clogging at the nozzle while attractive forces produce a yield stress allowing shape retention and the possibility of spanning elements [12]. Yield stress is defined as the stress at which the ink begins to flow. Viscosities around 10^4 Pa $\cdot$ s at low shear stresses have been reported as a viscosity high enough to maintain shape after deposition [13]. At shear stresses experienced in the nozzle during extrusion, the paste must behave as a liquid, or have a loss modulus larger than the storage modulus at frequencies representing rest, around 1 Hz. In this way, the liquid is extrudable through a fine-tipped nozzle [14].

Suspensions typically used to explore robocasting ink development consist of a nanoparticle powder, a polyelectrolyte dispersant, and a rheology modifier. Control of ink viscosity becomes more dependent on coating efficiency as the solid loading fraction increases. A stability map can be created to visualize how polyelectrolyte coating and solution pH changes the stabilization of the colloidal solution [15]. An optimal degree of flocculation (particle aggregation) is required for the ink to exhibit its yield stress. A completely stabilized solution with no yield stress will not retain its shape after deposition and is not desirable for printing [16], [17]. Free-polymers, which are not physically or chemically adsorbed to any particle, either promote flocculation or stabilization (dispersion) depending on the initial conditions of particle stability and operate similarly to solvation at length scales of several nanometers [18]. For printable inks, it is intended to use free-polymers to induce slight flocculation as a result of an osmotic pressure difference attributed to its absence between particles [19].

Printed inks with uncoated, unstable particles require higher pressures for extrusion and clog at the nozzle more easily than inks with coated, stabilized particles. The resulting data of this study will provide design parameters for producing concentrated (> 30vol%) magnetic inks that effectively separate the stability effect of polymer adsorbed to the surface and the flocculation caused by the excess polymer in solution. Polyelectrolytes are common stabilizing agents that have successfully coated and dispersed ceramic particles in aqueous systems, specifically for high-density (> 30 vol%) continuous syringe printing due to their charge providing an electrostatic repulsion effect [15]. Neutral polymers can alternatively provide a steric stabilization effect. For either, an optimum concentration is required, where excess polymer in the solution can induce flocculation [16]. Below the saturation limit, the repulsion between particles may not be enough to prevent flocculation. Polymer coatings combine both repulsive and attractive forces to form a suspension, are easily controlled, and can be applied to particles of many types of materials [20]. The surface energy of the nanoparticles determines which polymer is appropriate to use as a coating, and the adsorption efficiency is influenced by concentration, solution pH, and salt concentration. When using polyelectrolytes, the nanoparticles must have enough adsorbed dissociated or charged polyelectrolytes to enhance the electrostatic effects and enable stability. The design route of using stabilized particles in solution with minimal organic additives is an attempt to create a final shape with the highest possible solids loading.

The additional polymer will not adsorb to the surface of a nanoparticle if its concentration exceeds a level of saturation. The polymer chains will instead exist freely in the solution. Flocculation is induced by the free polymer possibly due to a bridging effect, where polymer chains adsorb to multiple particles. For the application of printing, slight flocculation is desired [21]. This interaction is more suitable for printing than a simply unstable particle solution because it induces enough of a yield stress without completely aggregating the particles in the solution, making it suitable to print while minimizing the amount of polymer required to experience shape retention [22], [23]. Alternatively, if particles are not adequately coated with polyelectrolyte, the excess polymer can induce a less reversible bridging flocculation by attaching to multiple particles. As an example, polyvinylpyrrolidone (PVP) is a commonly used rheology modifier for dense ceramic aqueous suspensions and has been shown to improve flow properties during deposition whose yield point can be controlled by varying its content and molecular weight [12], [22], [24], [25].

Flocculation due to a free-polymer induces a high yield stress without significantly altering the viscosity. An insufficiently coated particle comparatively induces irreversible flocculation that results in a much higher viscosity but insufficient yield stress [22]. The rheological behavior desired for printing is that of a shear-thinning fluid with a yield stress, a result of the slight flocculation of the particles. Rheology studies are used to quantify the optimal shear rate and yield stresses that result in minimized slumping behavior of the printed part, measured as the percent change in ideal shape [24]. With a sufficient attractive potential between particles, printed parts have displayed a mechanical integrity that withstands machining [26]. It is expected that the yield stress of the ink and the mechanical strength of the green printed part will increase for inks with increasing concentrations of added free polymer. The challenge arises in understanding repulsive and attractive potential effects in concentrated solutions and drying stresses, as well as ink flow in reduced nozzle diameters.

2.3 Inductors

An inductor is used to store energy within an induced magnetic field. Changes in current flow induce a perpendicular magnetic field according to Maxwell's equations, which in a coiled wire, concentrates the field within the windings. Inductors are essential circuit components used to store and release energy as current fluctuates. Including a magnetic material within the looped wire generates significantly higher magnetic field densities. There are many types of inductors, made into varying shapes, using a wide range of magnetic materials, and oriented in numerous constructions depending on the application. The unit for inductance is the Henry [H], which equals an induced voltage of 1 V when the current is varying at a rate of 1 A·s^{-1} [27].

$$H = \frac{V}{A \cdot s^{-1}} \tag{1}$$

Inductor operation is described by the relationship between Ampere's and Faraday's laws [28]. These Maxwell equations couple the magnetic and electrical phenomenon that makes energy storage possible in this system. Ampere's Law relates a magnetic field around a closed loop to the electric current passing through. Total magnetic force is proportional to the applied field along the length of a wire.

$$F = \oint Hdl = NI \approx Hl \tag{2}$$

Faraday's law of induction states that any change in the magnetic environment induces a voltage, and vice versa. Flux changes with time.

$$\frac{d\phi}{dt} = -\frac{E}{N}; \;\; \Delta\phi = N \int Edt \tag{3}$$

Energy storage and removal can be understood by integrating the applied field in terms of the time-dependent magnetic response. This area describes the total energy, while the area before the hysteresis describes energy stored and the area within the hysteresis curve describes energy lost with each direction change of current.

$$\frac{W}{m^3} = \int HdB \tag{4}$$

Magnetic permeability, a material characteristic, is defined as the amount of flux a field can push through a unit volume of material. Permeance applies the material characteristic to a defined area and length. Finally, inductance is the permeance coupled among all the conductive windings.

$$\mu = \mu_0\mu_r = B/H \tag{5}$$

$$P = \frac{\phi}{F} = \frac{BA}{Hl} \tag{6}$$

$$L = N^2P = \frac{\mu N^2 A}{l} \tag{7}$$

The performance of an inductor is measured by its inductance, L. Its energy efficiency is defined by the quality factor, or Q-factor, the ratio of the energy stored to the energy dissipated in the inductor, or more specifically a ratio of the component's inductance to its equivalent resistance. The range of frequencies in which it may effectively operate, defined as its bandwidth, is a function of the circuit's resonant frequency and quality factor, with the resonating frequency being dependent on the inductance and capacitance experienced in the circuit.

$$f_r = \frac{1}{2\pi\sqrt{LC}} \tag{8}$$

2.4 Magnets

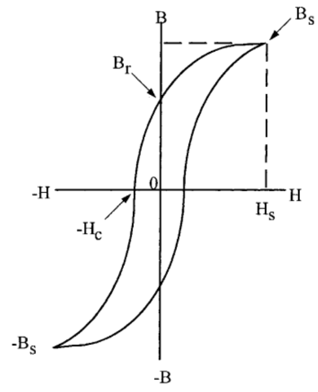

Figure 2.1: Typical B-H curve for magnetic material

A magnet is defined by its saturation (B_{sat}), permeability (μ), resistivity (ρ), remanence (B_r), and coercivity (H_c), all of which are notated in Figure 2.1. A hysteresis loop (or B-H curve) can be recorded using a Vibrating Sample Magnetometry device (VSM). The material is exposed to a sweep of applied magnetic field, and the strength of the magnetic response is measured. Saturation is defined as the state in which all the magnetic domains within the material are aligned, which occurs after enough of a magnetic field is applied to encourage alignment. Permeability is the ability of the magnetic field to be supported throughout the material and is illustrated as the slope of the hysteresis curve. Domain alignment is not a linear response; therefore permeability varies with the applied magnetic field. Resistivity is a measure of the energy barrier necessary to overcome to align the magnetic domains. Magnetic remanence is the magnetic strength of the domains aligned after the applied field has been removed. Coercivity is the magnitude of the opposing applied field required to cause a net magnetic moment of zero [29].

2.5 Magnets in inductors

Including a magnet within the core of the turns of an inductor increases its inductance by providing an easy path for magnetic flux, the quantity of which is defined by the magnet's permeability. The core is magnetized by the current passed through the windings. The time dependence of the flux change is a function of the voltage applied. These three items sum up the energy acting within the core. Inductance must remain constant throughout a range of applied currents. This requires the magnetic permeability to remain constant over a range of magnetizing forces and the effective resistance of the coil and the core losses to be minimized [1]. Recoverable energy is stored in non-magnetic inclusions of the core, such as the polymer binder holding magnetic particles together. Too much of the polymer, however, can reduce the beneficial magnetic properties by preventing magnetic flux coupling between particles [30].

Losses are a result of eddy current production and magnetic hysteresis, both of which are influenced by frequency. Eddy currents are produced as a result of the finite resistivity of the magnetic material and are compounded to the low-frequency hysteresis loss. Ferrite materials are highly resistive and are therefore often the material of choice for high frequency because eddy currents cannot conduct throughout the material. Alloyed ferrous magnets are engineered to have permeabilities magnitudes larger than ceramic iron oxide, maximizing at 100,000 for bulk nickel-iron alloys, but their resistivity is significantly lower and conducive to eddy current production, and they are therefore not suitable for high-frequency use without further modification. Typically, this involves laminating layers of magnetic material, or more recently, coating particles with an insulating shell [7]. Losses of the inductor can be modeled in an equivalent circuit with a resistor in parallel, which encompasses winding losses, core eddy current losses, and magnetic hysteresis losses [10].

The inclusion of magnetic materials in structures enhances some properties just as it has for planar inductors. A 3D-printed solenoid by the means of filling in microfluidic channels with conductive liquid metal paste has been characterized with a varying number of turns with and without the inclusion of a magnetic bar. The results are a 300-600% inductance enhancement (corresponding to 2-6 turns) after including the magnet in the same geometry [31]. The core material used is a commercially produced NiZn soft ferrite magnet, typically used for frequency ranges above 200 MHz. This comparison has been made again using microchannels filled with two different kinds of ferrofluids as the magnetic core within the inductor windings. The inductance is enhanced 1.3 - 2.6 times with the ferrofluids. The quality factor remains the same for low frequencies while becoming more lossy at higher frequencies. Their operating limit, however, remains relatively unchanged. The ferrofluids used in this study have the composition of magnetite suspended in hydrocarbon with permeabilities ranging from 3.6-19.6. The higher permeability material shows the highest increase in inductance [32].

2.6 High-frequency device operation

Higher frequency waves provide information faster; however, the signal attenuates faster and must be modulated to transport over long distances. A bias-tee is a circuit topology that couples a high-frequency signal containing information with a lower-frequency power wave, with a parallel inductor passing the lower-frequencies. The role of an inductor, when connected to a capacitor, is to act as a filter to decouple modulated signals and generate sinusoidal signals.

As semiconductor devices become more efficient, passive components such as inductors and capacitors and their topologies become the limiting factors in frequency performance with losses exacerbated at faster time domains. Passive electronics exhibit losses when operating at high frequencies and irretractable energy dissipates through the material as heat. Losses are a result of eddy current production and magnetic hysteresis, both of which are accumulated with increasing frequency. Minimizing these losses will increase the frequency range in which the device can be used efficiently. Eddy currents are produced because of the finite resistivity of the magnetic material and are compounded by the low-frequency hysteresis loss.

Ferrite materials are highly resistive and are therefore often the material of choice for high-frequency. Alloyed ferrous magnets are engineered to have relative permeabilities magnitudes larger than ceramic iron oxide, maximizing at 100,000 for bulk nickel-iron alloys, but their resistivity is significantly lower and conducive to eddy current production, making them unsuitable for high-frequency use without further modification. Typically, this involves laminating layers of magnetic material, or more recently, coating particles with an insulating shell [29]. Losses of the inductor can be modeled in an equivalent circuit with a resistor in parallel, which encompasses winding losses, core eddy current losses, and magnetic hysteresis losses [33].

2.7 Review of printed electronics

Printed electronics, including passive components such as the inductor (without a magnetic core), have been produced since the 1950s when conductive inks were discovered and first utilized [34]. Since then, significant research efforts have been made in the additive manufacturing of electronic components, with a focus on conductive traces [35], [36]. 3D printing can create stretchable and flexible electronics, considering the same fundamental principles of allowing the extrudability of particles in polymer solution can be used to pattern the filament into deformable geometries [37]. Electronic devices [38] that have been printed using DIW include electrodes [39], conductive wiring for electric circuitry [40], [41], and other functional components such as sensors [42] and quantum dynamic light emitting diodes (QDLEDs) [43]. The underlying principles of controlling printability are the same but are accomplished with specific types of particles focusing on efficient current flow. A major hurdle in the fabrication process of conductive inks is converting the ink from a non-conductive state to an optimized, efficient conductive state. Often, heat is used to remove organic surfactants and densify parts.

2.8 Printing inductors

The employment of additive manufacturing techniques to fabricate magnetic composites, specifically inductors, is a relatively recent research interest. Inductors are the major size-limiting component in power converters. Decreasing size increases the frequency range of the device. However, with increasing frequency, there are more compounding losses. Inductors are typically the largest components of a circuit board

[44]. Typical, non-additive methods of fabricating a magnetic core for inductors involve using high-pressure powder-compaction, followed by sintering, and then hand winding [45]. There is a need to develop fabrication technology to reduce the size of inductor parts. The traditionally printed inductor is in the form of a planar spiral, printed directly on the circuit board substrate with the same conductive ink used for interconnects. An inductor's performance is hindered by its geometry and size-dependent parasitic capacitances [46]. Parasitic capacitances are a result of capacitive behaviors in neighboring materials that cause the operating component to veer from ideal performance. These parasitic capacitances become increasingly more important at higher frequencies [47]. To optimize the self-resonant frequency (SRF), parasitic capacitances must be minimized or eliminated. Typically, printed planar inductors have a large substrate contact area and are plagued by substrate capacitances and leading to the exploration of different 3D geometries [48], [49]. Solenoid inductors achieve a higher inductance density with reduced substrate parasitic losses compared to planar inductors due to confined parallel magnetic field lines to the substrate [50]. External magnetic fields from inductors can cause electromagnetic interference issues. Toroids have a weaker external magnetic field compared to solenoids and planar structures [51]. Solenoid inductors have a higher efficiency and inductance density compared to planar inductance by better confining the magnetic field lines. Many magnetic core solenoid inductors have been fabricated in many ways (electroplating, manual filling, spin spraying, enclosing in polymer, or hand winding a commercial part), but not by 3D printing [52]. All of these processes have disadvantages, but the greatest disadvantage is the increased time and cost of processing. Ahn et al. claim using fabricating an

inductor on a planar substrate is "an extremely difficult task", and requires "quasi-three-dimensional micromachining techniques [53]." Most of the efforts in 3D printing an inductor have been focused on the quality of 3D printed conductive traces, and in that realm, there have been significant achievements. The inclusion of the magnetic core is far less studied. The challenge arises in fabricating a core with optimized permeability. Efforts to print a core often include inserting a traditionally manufactured core into printed windings [54] or printing the core separately and then hand-winding it to form the final inductor device [55].

2.9 Printing magnetic inductors

The 3D fabrication of the magnetic core itself has yet to be extensively studied. Some examples of ferrite–thermoplastic composites have been demonstrated to print using the traditional fused deposition modeling (FSDM) printing process. A study of NiZn ferrite in ABS demonstrates printed products with low volume fraction (< 25 vol%) and therefore low relative permeability (< 3) [56]. A commercially available metal powder – PLA composite provided by the company Proto-pasta displays similar results [57].

Another effort to incorporate magnets into an inductor device is to coat a thin layer of magnetic ink onto a planar spiral. A reported printed planar inductor with 1.5-3.5 turns and a 42 mm^2 footprint has a maximum inductance of 75 nH, Q of 3.3. A 10 nH inductor has a resonant frequency slightly below 1 GHz. No magnetic material is involved [45]. Another planar printed inductor has an added layer of NiZn doped ferrite ink to improve inductance and operates to 1MHz with an inductance near 200 nH [58]. In another study, printed micro inductors were fabricated on top of a flexible polyimide substrate. The magnetic core was screen printed using an MnZn-doped ferrite magnetic ceramic mixed in a thermoplastic resin with solvent. Conductive copper windings are planar, with the screen printed magnetic film on the front and back to shield [59]. In another study, iron oxide nanoparticles were synthesized and functionalized with oleic acid and mixed into a commercially available, proprietary UV-curable polymeric resin (SU-8) at a particle loading of 50 wt% to screen print a "free-standing" magnetic substrate. Functionalized particles were suspended in water to inkjet print a thin film in which a silver ink planar inductor was printed on top [60]. In another study, NiZn ferrite inks were coated with a dispersant (proprietary) and mixed in dimethylformamide (DMF) at 30 wt% to inkjet print a thin film [61].

Only a few studies report printing three-dimensional inductor cores or printing non-planar inductors with included magnets. This study by Bellaredj et al. reports fabricating an entirely 3D-printed inductor, including the core, insulating materials, and windings. The core is made of a NiZn ferrite epoxy composite made in-house by mixing functionalized magnetic particles in a formulated curable epoxy binder at an 85 wt% particle loading [62]. The curing occurs at 180°C. The final part has a volume of approximately 6.5 mm^3 and reports an inductance of 30 nH and a Q-factor of 6.4 at 100 MHz [52]. Yan et al. [55] have published about additive manufacturing of soft magnetics, using a 3D printer to extrude optimized magnetic pastes. A multi-extruder printer co-extruded a poly-mag (polymer magnetic composite) paste consisting of permalloy (NiFe) powder and benzocyclobutene for the core and a nanosilver paste for the windings. A stable permeability of 10 is reported up to 30 MHz with no discussion of inductance [63]. The same group then reports working with a NiCuZn ferrite-coated planar inductor that after sintering has a permeability near 100 up to 10 MHz [64]. Hodaei et al. report on ink made of iron oxide functionalized with a single block copolymer to attain an 81 wt% in water that is printed into a 3D toroidal structure for inductance characterization. These structures were robust and hand-wound without any additional heat treatment steps. A 1206 mm^3 volume toroid with 60 turns had an inductance of 20 μH up to 1 MHz [65].

The additive manufacturing of conductive traces for circuitry is an established practice used in modern-day electronics. For inductors, the most studied devices fabricated using AM technologies are planar spiral structures, but the 3D printing of magnetic cores for inductors has much room for investigation, especially for the application of high-frequency electronics.

Chapter 3: Inductors Fabricated from Magnetic Nanoparticles Mixed in Curable Resin

3.1 Introduction

The rapid material development of integrated circuit technologies to nanometer dimensions has allowed operating frequencies to approach THz, as the operating frequency is inversely proportional to device size. Such high-frequency (HF) circuits allow for improved optical fiber communications in television broadcasting, automotive radar and sensor communications, personal radio services such as Wi-Fi and Bluetooth, satellite communication such as GPS, military targeting, and tracking, and inter-space satellite communications. As operating frequencies increase, circuit topology requires a design change, affecting the technology generation, type, size, and bias current of all the passive components, including magnetic devices such as inductors, transformers, and transistors.

To maximize the storage capabilities of an inductor, a magnetic core is included within the coils. The motivation for this research is to utilize additive manufacturing to create a functional inductor magnetic core in an appropriate geometry. Printing magnetic inks has been a challenge, especially when it comes to the percentage of magnetic material within the final printed product, which directly affects its performance. Mixing magnetic particles within a thermoplastic filament requires a large percentage of polymer to retain desirable flow properties for printing. The ability to extend this technique to magnetic materials will accelerate material discovery and advancement to produce passive electronics with greater efficiency, increasing the speed of communication in electronics to keep up with current integrated circuit advancements.

There have been many efforts to manufacture magnetic polymer composites with the simplest and most common method being mixing just two ingredients – magnetic particles and a polymer matrix that gets crosslinked through thermal or UV curing[66]–[68]. This technique was explored initially here to understand the limitations of using this method and the balance between inductance and resonant frequency as a function of particle loading. The magnetic particles tested were spherical, 50-100 nm diameter iron oxide ($Fe_2O_3 \cdot FeO$, Sigma), and both cubic, 300 nm face length FeCo (1:1) and 250 nm permalloy ($Ni_{80}Fe_{20}$) synthesized in-house. The polymers used as the matrices in these studies were UV and thermally curable NEA121 (Nordland Adhesives), thermally curable polyimide, and the epoxy resin polydimethylsiloxane (PDMS, Gelest).

3.2 Results & Discussion

3.2.1 Printability as a function of particle loading

Particle loading drastically influences ink viscosity (Figure 3.1). Particle mixtures were tested at various weight fractions to determine the maximum particle loading that can still be extruded through an 18 G nozzle. At the maximum particle loadings, printed parts had enough strength to retain their shape after deposition and before curing.

Toroids of iron oxide in NEA121 were printed at 50, 60, 70, and 80 wt%. The 50 wt% compositions flowed too easily, and a shape was retained by using UV to cure the skin and maintain shape between layers. 60 wt% composition printed part looks identical to the toroid shape that had been molded. Beyond 70 wt% composition requires a solvent (methylene chloride) to reduce viscosity enough for extrusion. Particles appear to be distributed evenly throughout the cured resin (Figure 3.2).

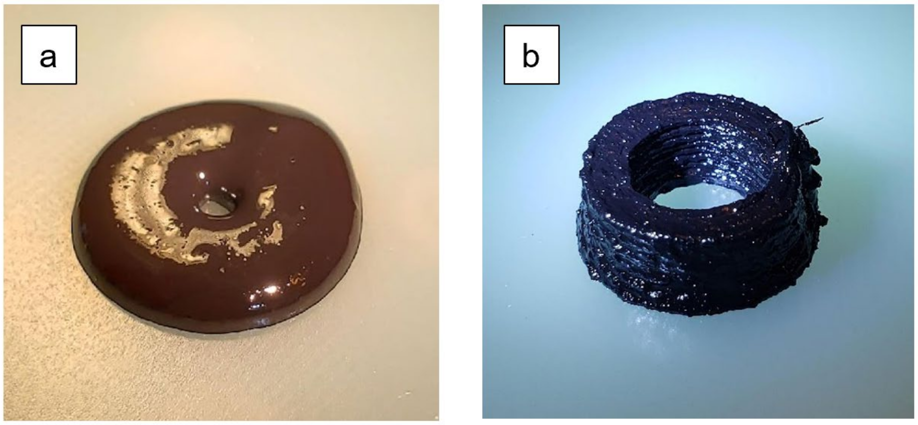

Figure 3.1: (a) 50 wt% and (b) 75 wt% particle loading of iron oxide in polyimide

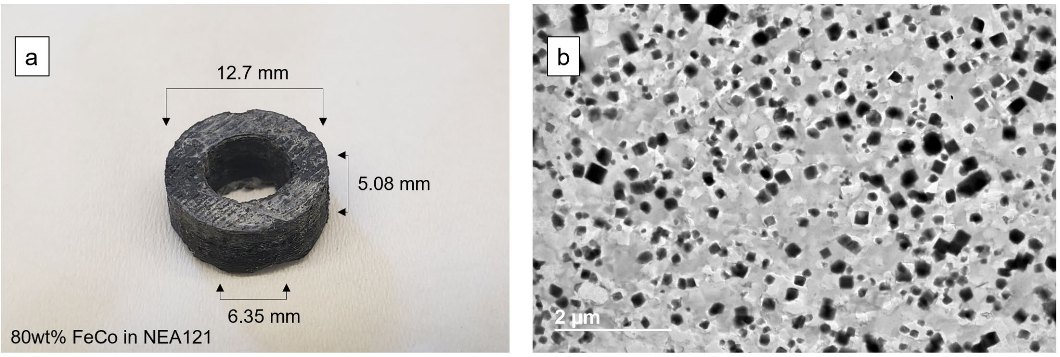

Figure 3.2: 80 wt% FeCo in NEA121 (a) molded into a toroid and its (b) cross-sectional TEM image displaying the particles dispersed in the cured resin

3.2.2 Printability and rheological study with solvents added to NEA121 ink mixtures

Uncured NEA121 was first evaluated for solubility in high-volatility solvents. It was found that NEA121 is soluble in tetrahydrofuran (THF), methylene chloride, methanol, and ether. Then it was determined whether the crosslinking process was affected by the addition of these solvents. THF and methylene chloride were the only solvents that did not inhibit the curing behavior or final morphology of the cured part when using both oven heating or UV light to cross-link. FeCo in NEA121 is printable below 80 wt% but requires 30 wt% of solvent (solvent: resin) to extrude at 80 wt% particles in resin. The resulting shape is self-supporting, and the resulting material is completely oven curable with no observable bubbling or discoloration. For iron oxide mixed in NEA121, the ink mixture becomes difficult to extrude at 70 wt% but is printable at 80 wt% (33 vol%) with the addition of methylene chloride as a solvent. Attempts to print at 50 vol% were made by increasing the addition of solvent to allow extrusion, but extreme volume change was experienced during the oven cure due to the large volume of solvent that evaporates during the oven curing process. Moreover, the particles were not stable in the solvent and the mixture was not truly homogeneous. These results led us to investigate alternative ink formulation methods to achieve higher particle loadings.

The rheology of inks with FeCo in NEA121 was evaluated with and without methylene chloride as a solvent. The 75 wt% ink with no added solvent (Figure 3.3 (a)) has a zero-shear rate viscosity of 750 Pa·s, while the sample with added solvent (Figure 3.3 (b)) has a zero-shear rate viscosity of 230 Pa·s. Both still exhibit shear thinning behavior as evidenced by the decreasing viscosity with increasing shear rate.

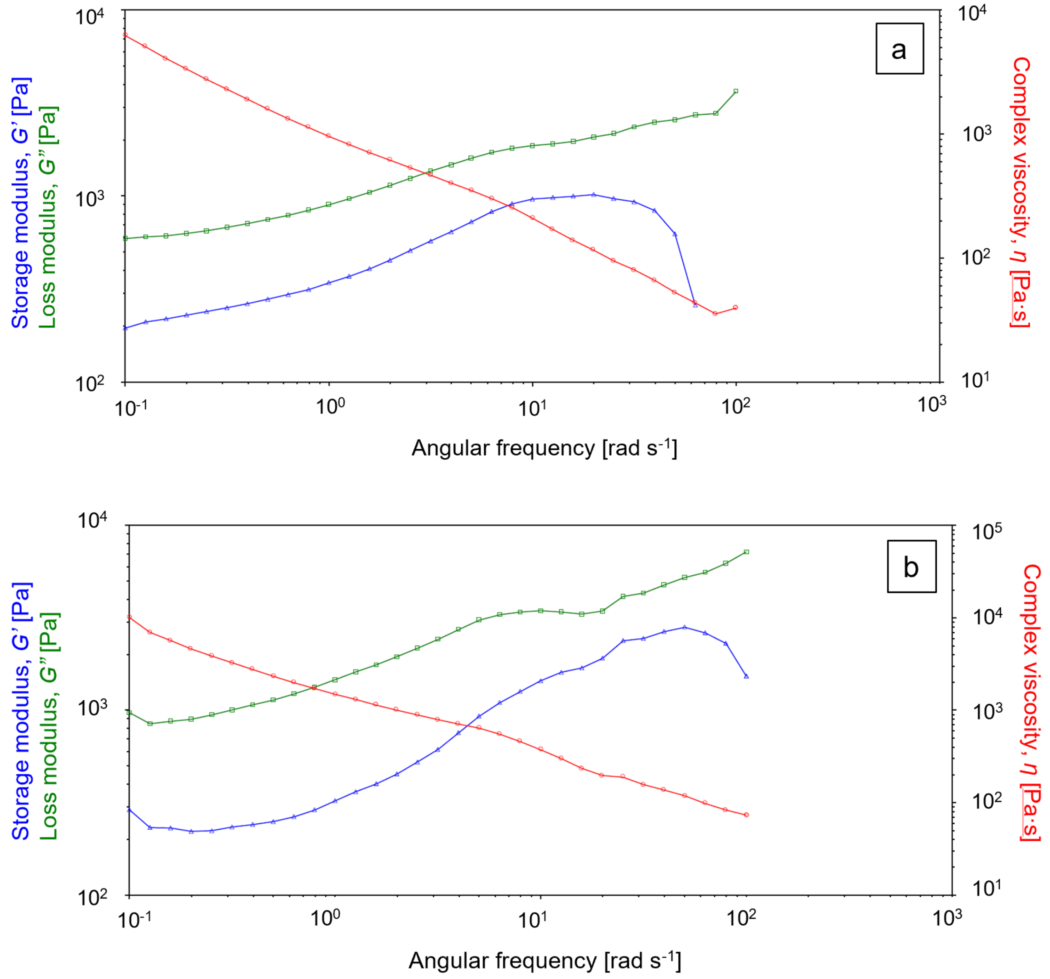

Figure 3.3: Rheology of (a) 75wt% FeCo in NEA121 without solvent (b) 80wt% FeCo in NEA121 with methylene chloride as a solvent.

The addition of low-viscosity solvent improves printability as long as it does not influence the curing behavior or morphology of the resin. Too much solvent causes a large volume change as the solvent evaporates. 80 wt% FeCo with the addition of 30wt% methylene chloride (solvent:resin) allowed a flow rate of 0.45 mm^3s^{-1} at 80 psi. The curing of the composite is not hindered, and the solvent evaporates with no volume change.

3.2.3 Magnetic characterization using vibrating sample magnetometry (VSM)

Molded or printed samples with various particle loadings are mounted to a VSM for magnetic characterization. The hysteresis curve recorded with this device provides insight into the behavior of an inductor constructed with the magnetic composite material as the core. From the hysteresis curve, the maximum magnetic saturation, relative permeability, coercivity, and hysteresis loss can be interpreted. All of these values hold some significance to the performance ability of the final constructed device. Magnetic saturation is the point at which all of the magnetic domains within the material are aligned, and this determines the limit of current or voltage that can be stored within the inductor. If exposed to current beyond the saturation limit, the inductor is less efficient and behaves more like a resistor than an inductor. The relative permeability is the ratio of magnetism to the applied magnetic field. The higher the value, the more responsive the material is. For an inductor, this value should be maximized, as it is directly related to the inductance. Coercivity is the magnetic field strength required for the magnetic domains to switch to the opposite direction. Ideally for an inductor, this value is nearly zero. The magnetic field is what is being stored within the material, and if it is spent switching domain direction then it is lost in operation. The hysteresis loss is the energy that is wasted in the form of heat when the magnetic direction is switched. This is calculated as the area within the forward and backward curves. An ideal inductor would have no hysteresis loss. Figure 3.4 exemplifies how to interpret these values from the VSM curve for 80wt% FeCo in NEA121.

From the hysteresis curve recorded by VSM, we can compare the bare FeCo powder (Figure 3.5) to FeCo particles mixed in resin (Figure 3.6). For the bare powder, the magnetic saturation approaches 200 emu/g, which is consistent with the literature values. The coercivity is approximately 210 Oe. The maximum relative permeability calculated from the slope of the curve is 8.96 (a relative, unitless value). After mixing in resin at an 80wt% particle loading, the magnetic saturation of the composite approaches 180 emu/g, a decrease from the bulk value due to isolation between particles in the polymer resin. The coercivity is similar to bulk values indicating that the resin does not alter the magnetic field strength required to switch directions of the magnetic domains within the material. The maximum relative permeability calculated from the slope of VSM is $\mu_r = 3.93$, which is less than the pure powder due to the inclusion of the polymeric material. Since permeability is directly related to inductance, we can predict that the more magnetic material included in the composite, the higher the permeability and therefore inductance.

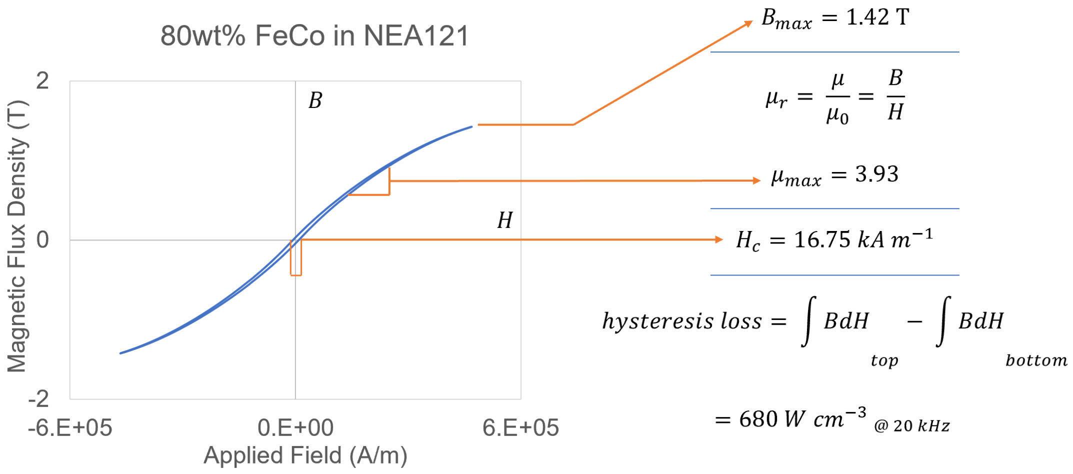

$B_{max} = 1.42$ T

$\mu_r = \frac{\mu}{\mu_0} = \frac{B}{H}$

$\mu_{max} = 3.93$

$H_c = 16.75\ kA\ m^{-1}$

$hysteresis\ loss = \int_{top} BdH - \int_{bottom} BdH$

$= 680\ W\ cm^{-3}\ _{@\ 20\ kHz}$

Figure 3.4: Interpretation of magnetic hysteresis acquired with VSM to calculate magnetic saturation, relative permeability, coercivity, and hysteresis loss of 80 wt% FeCo in NEA121.

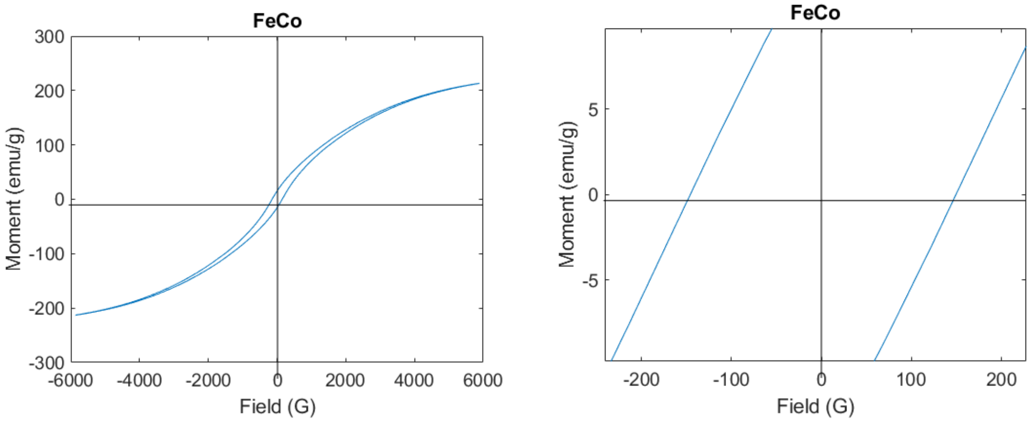

Figure 3.5: VSM of FeCo bare powder showing its magnetic response. The graph to the right is zoomed in to make the coercivity clearer.

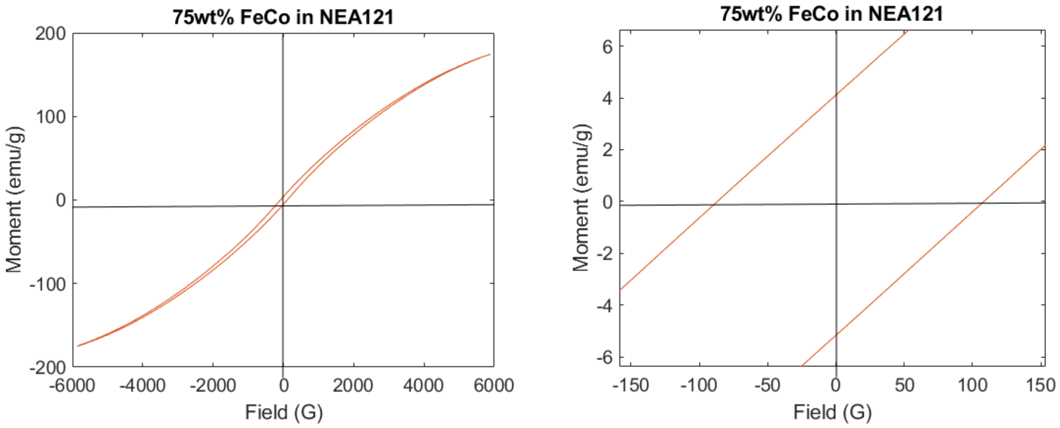

Figure 3.6: VSM of 75 wt% FeCo in NEA121 showing its magnetic response. The graph to the right is zoomed in to make the coercivity clearer.

3.2.4 Construction into an inductor mounted to a transmission line

Toroids were printed or molded into a target dimension of 12 mm outer diameter, 6 mm inner diameter, and 5 mm height. A thin copper was carefully hand-wound around the toroids at least 15 times, making sure they were tight around the composite material. The wire was then soldered to an SMA ("sub-miniature version A" coaxial cable connection) connection part for attaching to the VNA for measurement (Figure 3.7). When comparing directly, the same number of windings were used between samples. At a high enough particle loading, the uncured ink was sufficiently viscous and shape-retentive to resemble the desired toroid dimensions. Only a few ink compositions per system fit these criteria because if the ink viscosity was too low the printed shape had no semblance to a toroid and was unusable.

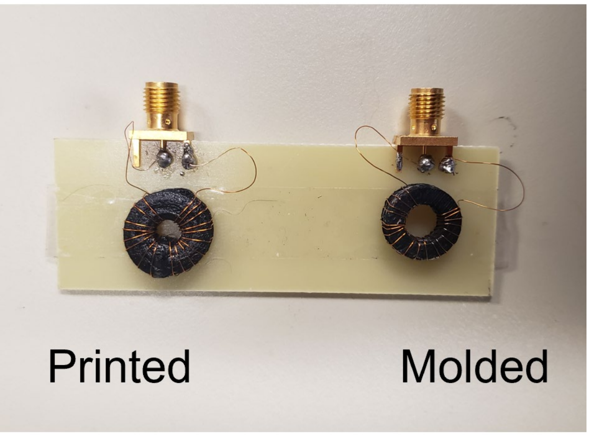

Figure 3.7: Printed and molded 75 wt% FeCo in NEA121 inductors hand wound and soldered to an SMA for connection to a VNA for inductance measurements.

One composite ink formulation was successfully printed into a cone instead of a toroid to reduce stray capacitances and achieve higher bandwidths. The results of this study have been published [69]. FeCo was mixed into NEA121 at 75wt% and printed through an 18 G nozzle with the syringe printer without a tool path but by manually lifting the nozzle in the z-direction at increasing speed while maintaining a constant extrusion pressure. The printed cone was then thermally cured, removed from its substrate, and mounted onto an AJ printer. The conductive windings were AJ printed using a silver nanoparticle (NP) ink using the tool path as shown in Figure 3.9 and mounted onto a transmission line at a fixed angle by resting onto a dielectric mount. Interconnects were AJ printed using the same silver NP ink to complete the circuit and reflectance parameters were measured using the VNA (Figure 3.8, 3.9).

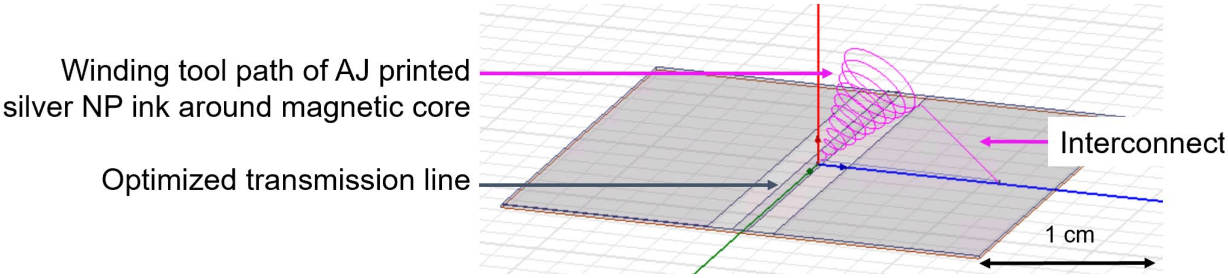

Figure 3.8: The plan for printing windings around the magnetic cone core.

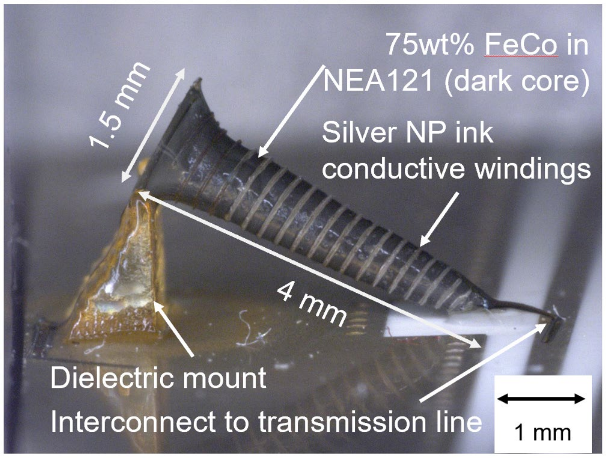

Figure 3.9: Syringe printed 75wt% FeCo in NEA121 magnetic core mounted to a transmission line with AJ printed silver NP conductive windings and interconnects.

3.2.5 Inductance characterization using a vector network analyzer (VNA)

A Vector Network Analyzer (VNA) from Agilent Technologies that sweeps between 1 kHz to 1.5 GHz using an SMA connection is used to measure reflectance at high frequencies, in which complex impedance and therefore total resistance and inductance can be calculated. Hand wound toroids of various compositions either syringe printed or molded were soldered to an SMA connection so that reflectance parameters can be measured and compared as a function of particle loading and magnetic composition.

From reflectance data, we can observe the resonant frequency and calculate the value of inductance at frequencies below resonance. Below the resonance frequency, we can assume predominant inductive behavior and negligible capacitive behavior. We can also calculate the Q factor, which is the ratio of stored to dissipated energy, or the ratio of imaginary to real impedance.

$$Z_L = R + jX_L, where\ X_L = \omega L, and\ Q = \frac{X_L}{R} \tag{1}$$

R is the resistance, ω is the angular frequency, X_L is the inductive reactance, L is the inductance, and Q is the quality factor. The resistance measured using this method includes the resistance of the entire circuit system and should not be attributed entirely to the magnetic core material.

Effective permeability can be calculated as a function of frequency from inductance data, as well. The following equation is used specifically for a cylindrical structure:

$$\mu_{eff} = \frac{L\,l}{\mu_0\,N^2 A} \tag{2}$$

Where L = inductance, l = length of flux path, μ_0 = permeability constant, N = number of turns, A = cross-sectional area of flux.

The inductance is measured as a function of frequency for hand-wound toroidal inductors with two different particles loading of FeCo in NEA121. The higher particle-loaded sample (75wt%) has a higher inductance of 960 nH at a frequency of 20 MHz compared to the 50wt% which has an inductance of 620 nH at the same frequency (Figure 3.10). The decrease in inductance is due to the lower concentration of magnetic material which reduces the magnetic coupling, minimizing the inductance. The resonant frequency, however, increases with decreased particle loading, with the

75wt% sample experiencing resonance at 83 MHz while the 50 wt% experiences it at 160 MHz. This is due to the less magnetic loss with the reduced magnetic particle loading. These measured device performances are supported by the magnetic behavior observed with VSM. Increasing the polymer content reduces the magnetic response or permeability of the composite material, which reduces the inductance.

The resonant frequency observed for the toroids made with added solvent was higher than the ones made without added solvent. A possible explanation can be that bubbles formed while the solvent evaporated, and the resin cured. The particle concentration is nearly the same, but there is isolation provided from the void space that inhibits eddy current losses.

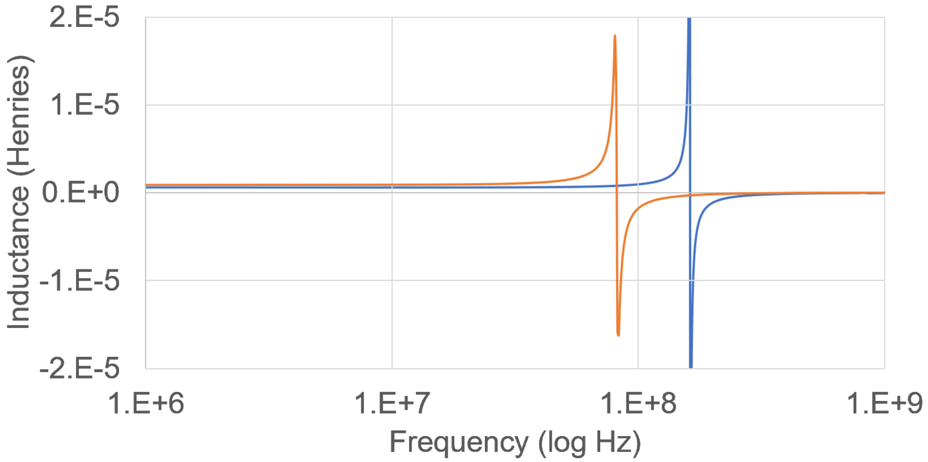

Figure 3.10: Inductance as a function of frequency for 50wt% (blue) and 75wt% (orange) FeCo in NEA121 toroids.

The conical inductor of 77.5 wt% (30 vol%) FeCo in NEA121 had a resonant frequency of 20 GHz due to its size, geometry, and orientation. The inductance of the conical inductor was 100 nH at 20 MHz, which normalized to volume comes to 50 nH mm^{-3}. The toroid comparatively has a normalized inductance to volume of 2 nH mm^{-3}. This speaks to the better efficiency of the conical inductor which can more effectively produce inductance than the toroid due to its shape.

The type of particle (FeCo or iron oxide) also impacts the performance of the constructed inductor device due to their different magnetic properties. Two samples with the same particle loading of 75wt% in NEA121 but different magnetic materials were created, hand-wound, and analyzed as an inductor using VNA (Figure 3.11). The iron oxide composite core inductor had a lower inductance of 820 nH (measured at 20 MHz) compared to 960 nH of the inductor with the FeCo composite core. The permeability measured from the magnetic hysteresis of iron oxide is $\mu_r = 6.5$ which is lower than that of FeCo which is measured to be $\mu_r = 9$. Due to the lower permeability of iron oxide, the inductance of the composite is lower than that of the FeCo composite core at the same particle loading. The resonant frequency, however, is higher for the iron oxide composite measured at 135 MHz compared to the FeCo composite. The self-resonance of the circuit is inversely proportional to the inductance, and therefore with a lower inductance, the circuit experiences a higher resonant frequency. This allows the iron oxide composite core inductor to behave efficiently at a broader range of frequencies compared to the FeCo composite core inductor which has a higher permeability and inductance and lower resonance.

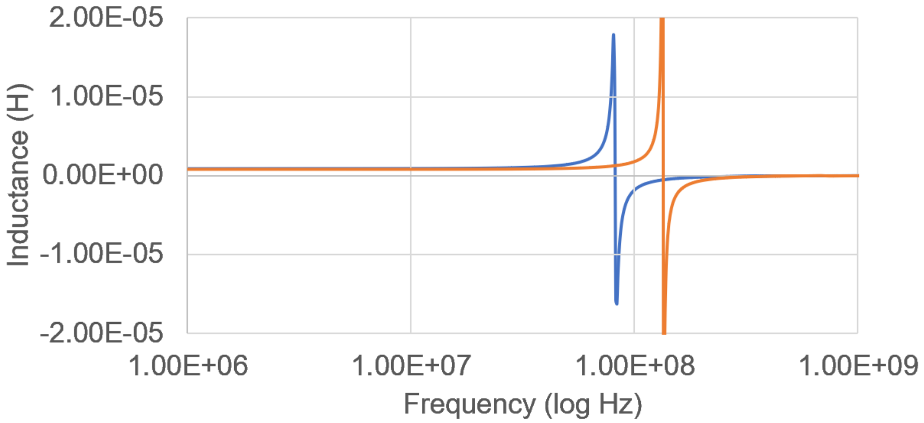

Figure 3.11: Inductance as a function of frequency for iron oxide (orange) and FeCo (blue) at the same particle loading of 75 wt%.

Only a couple of compositions were able to be tested with the FeCo material because it was made in-house and had a low yield per synthesis. To better understand the impact of particle loading on device performance, a study was conducted with a larger particle concentration range of iron oxide in PDMS molded toroids (Figure 3.12). The general trend of nominal inductance (inductance normalized to the number of windings squared) is that it increases with increasing magnetic particle concentration. This is due to the increasing magnetic response with increased magnetic material. The resonant frequency has a decreasing trend with increasing particle loading. The resistance measured does not appear to have a trend but is relatively unchanging with particle loading. The quality factor does increase due to the increase in inductance and consistent resistance with increasing particle loading. From this information, we can conclude that increased magnetic material increases inductance and efficiency but limits the frequency range of operation of the constructed magnetic inductor device.

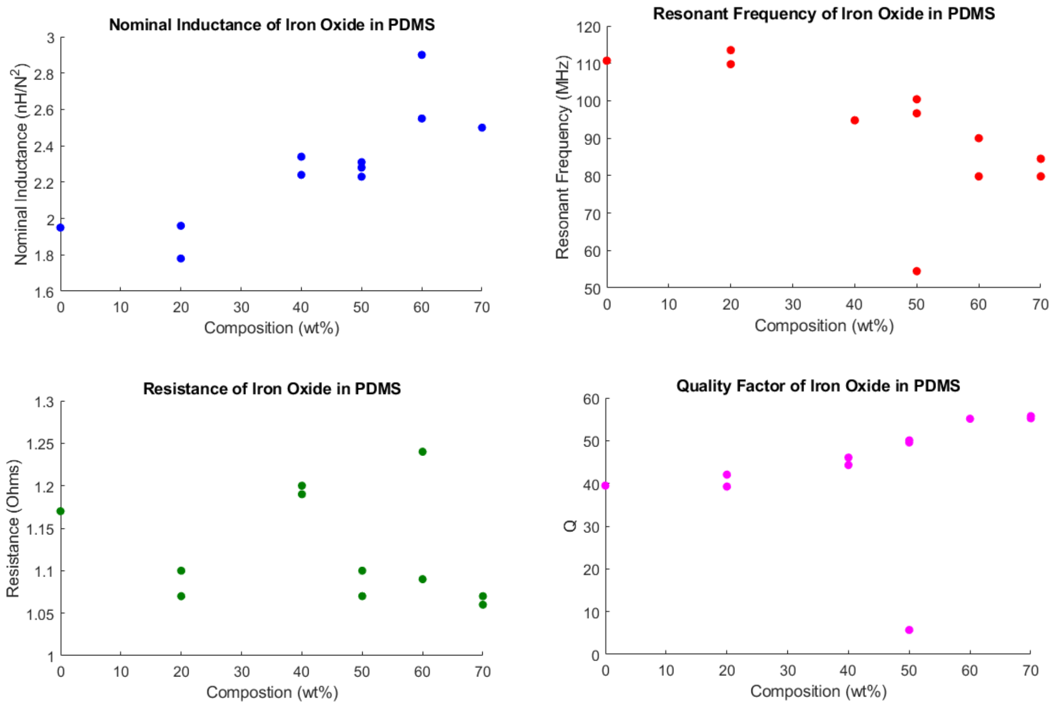

Figure 3.12: Nominal inductance, resonant frequency, resistance, and quality factor of iron oxide in PDMS at various particle loadings as calculated from reflectance data.

3.2.6 FEM modeling of a composite inductor

Effective medium theory (EMT) describes the macroscopic properties of composite materials by averaging the properties of their constituents. EMT can be used to predict permeability- and permittivity-dependent behaviors of a composite device, such as inductance (L) and self-resonant frequency (SRF). There are a few widely known models used for EMT calculations, the Maxwell-Garnett model and the Bruggeman model[28]. The Maxwell-Garnett model is only good for homogeneous medium, which assumes particles are anisotropic and uniformly dispersed in a matrix and ignores interactions between inclusions. It is therefore most accurate for extremely dilute composites. The equation used for this model is as follows:

$$\varepsilon_{eff} = \varepsilon_d \left[1 + 3c_m \frac{\varepsilon_m - \varepsilon_d}{\varepsilon_m + 2\varepsilon_d - c_m(\varepsilon_m - \varepsilon_d)} \right] \tag{3}$$

where ε_d is the permittivity of background medium, in this case, the polymer matrix, ε_m is the permittivity of individual inclusions, in this case, the magnetic nanoparticles, and c_m is the vol% of inclusions (particles). This calculation applies to both permittivity and permeability. To calculate permeability, all cases of permittivity are replaced by permeability.

The Bruggeman model is claimed to be more accurate than the Maxwell-Garnett model by accounting for interparticle interactions. The model has many modifiers to consider isotropic, high aspect ratio particles, although that is not necessary in the case of this study. The model was developed to model metallic particles <10nm in diameter. The equations used for this model are as follows:

$$\varepsilon_{eff} = \frac{H_b + \sqrt{H_b^2 + 8\varepsilon_m \varepsilon_d}}{4} \tag{4}$$

$$H_b = (2 - 3c_m)\varepsilon_d - (1 - 3c_m)\varepsilon_m \tag{5}$$

Where ε_d is the permittivity of the background medium (polymer), ε_m is the permittivity of individual inclusions (particles), and c_m is the vol% of inclusions (particles). This calculation also applies to both permittivity and permeability. To calculate permeability, all cases of permittivity are again replaced by permeability [70].

Using bulk electromagnetic properties of the magnetic material the nanoparticles are made of predictions of the permeability of the composite can be calculated using these EMT models and compared to experimental values.

Table 3.1. Comparison of permeability calculated from EMT with experimental results. The max permeability used in the calculations are from experimental VSM data of pure powder. The permeability of the polymer matrix is assumed to be 1. The samples tested in this chart are of the highest possible syringe printable particle loading in NEA121 ink.

Material	**Permalloy**	**FeCo**	**Iron Oxide (II, III)**
Particle size	**250 nm**	**250 nm**	**130 nm**
Max permeability	**$\mu = 10$**	**$\mu = 9$**	**$\mu = 6$**
wt%	**85 wt%**	**75 wt%**	**70 wt%**
vol% particle loading	**42 vol%**	**29.4 vol%**	**34.1 vol%**
Maxwell-Garnett	2.38	1.82	1.81
Bruggeman	3.22	2.14	2.03
Experimental VNA	12.94	4.49	5.37
Experimental VSM	N/A	3.93	N/A

Permeability calculated from VNA which measures across a range of frequencies does not match values calculated from either the EMT model or from VSM data. The EMT models do not account for frequency and the VSM measures at very low frequencies, between 50-100 Hz. Typically, the permeability should decrease with increasing frequency. The permeability calculations from VNA data could be inflated because of inaccurate modeling of the equivalent circuit or incorrect assumptions made that there is no capacitive behavior below the resonance observed within the tested frequency range.

Finite element method (FEM) based simulation in COMSOL Multiphysics software is used to predict intrinsic material properties of magnetic-polymer composites of varying compositions. Composite geometries are drawn as spherical or cubic magnetic particles within a polymer block (Figure 3.13).

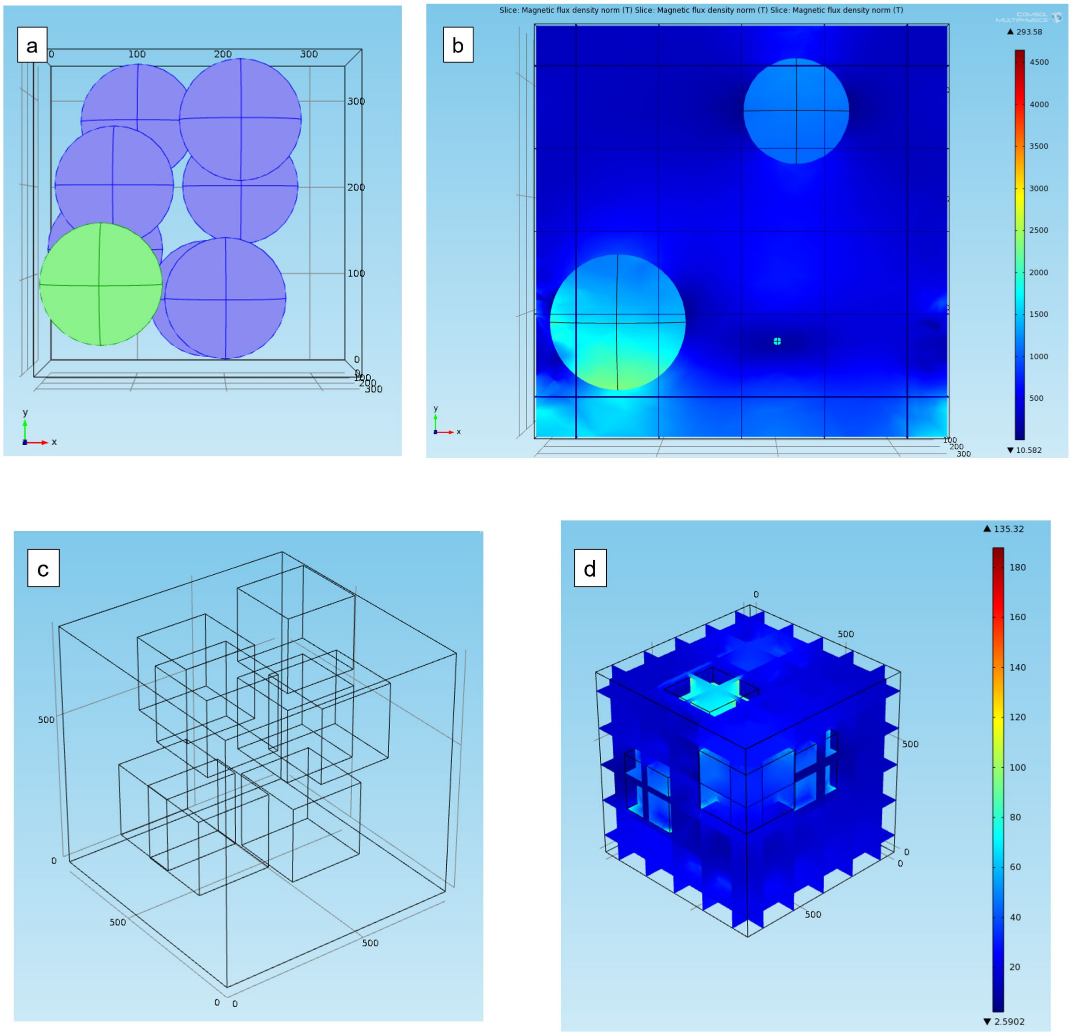

Figure 3.13: Geometries drawn in COMSOL of (a) random placement of spherical particles at 75 wt% and (b) their magnetic response in the presence of an electric field, and (c) random placement of 50 wt% cubic particles, and (d) their magnetic flux density distribution [T] in the presence of an electric field.

To calculate permeability and permittivity, COMSOL Multiphysics calculates an average volumetric response to an applied magnetic or electric field, respectively. One of the faces of the box is set as an input of the applied field, while its opposite boundary is set as an opposing field to create a potential difference. All other boundaries are made to be periodically continuous.

Polarization $\bar{P}$ is proportional to the total macroscopic field $\bar{E}$,

$$\bar{P} = \varepsilon_0 \chi_e \bar{E} \tag{6}$$

where ε_0 is the dielectric permittivity of free space and χ_e is the electric susceptibility. Dividing $\bar{E}$ form $\bar{P}$ provides the relative permittivity ε_r, where

$$\varepsilon_r = (1 + \chi_e) \tag{7}$$

Similarly, magnetic flux density $\bar{B}$ is proportional to the magnetic field $\bar{H}$,

$$\bar{B} = \mu_0 \mu_r \bar{H} \tag{8}$$

where μ_0 is the magnetic permeability of free space and μ_r is the relative permeability of interest.

To simulate, the electrical conductivity, permeability, and permittivity of the constituent materials are defined. Electrical conductivity and permittivity values are input as reported in the literature. The permeability of magnetic material is input from in-lab VSM measurements of dry powder samples.

Simulated results are compared to experimental data acquired from VNA and VSM measurements to confirm accuracy (Figure 3.14). Modifications to the simulation can be made to improve data fitting, as necessary. It could then be justified to use these simulations to predict the behavior of materials prior to fabrication, creating a more targeted and efficient approach to developing device structures.

COMSOL experiments of modeled composites with spherical particles with the magnetic properties of FeCo show no difference in whether particles are ordered within the matrix or randomly placed (Figure 3.13). The simulation does show an increase in permeability when the particles are modeled as cubes instead of spheres, which for the 75 wt% composite shows a closer semblance to the experimental VSM calculated permeability than the spherical particles. The FeCo particles measured with VSM are indeed cubic in shape and the model is truer to reality. The EMT Maxwell-Garnett (MG) and Bruggeman (Brugg) equations were developed to model spherical particles, and so they match the spherical particle COMSOL model values for permeability more than the cubic model. Only the random placement of cubic particles at 50 wt% was modeled in COMSOL because the MatLab code was unable to produce a random order of cubic particles that fit within the confined space. These modeling attempts can be improved with a more realistic design of the composite material. There is a limited picture drawn from the COMSOL simulation only at direct current or with no frequency dependence. The behavior of an inductor is complex and dependent on frequency. A model done with no frequency dependence can allow only a limited prediction of behavior at higher frequencies.

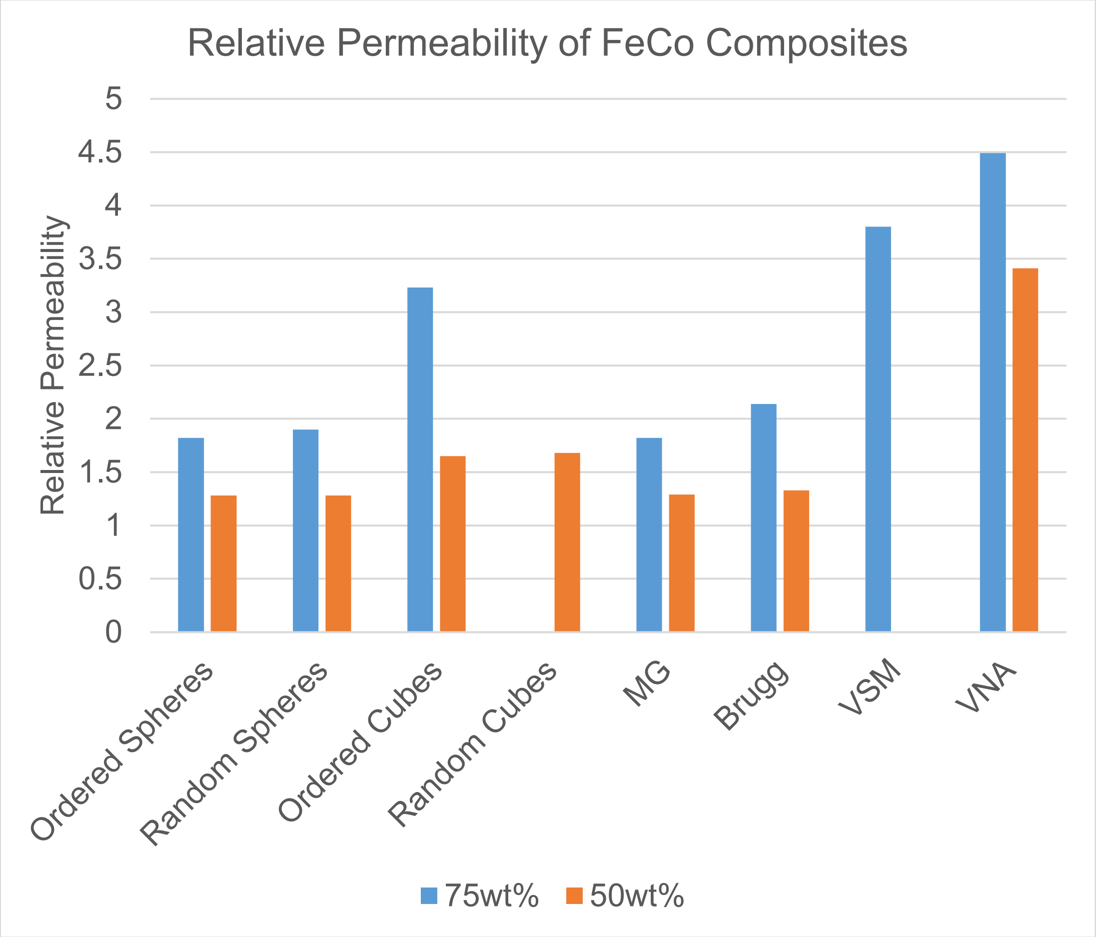

Figure 3.14: Relative permeability of FeCo in NEA121 at 75 wt% (blue) and 50 wt% (orange) calculated using COMSOL, EMT, and experimental methods.

3.3 Conclusion

FeCo, NiFe (permalloy), and iron (II, III) oxide magnetic particles with varying magnetic properties were incorporated in different resins to explore the influence of particle loading on printability and inductor device performance. It was generally found that increasing particle loading increased ink viscosity, with a loading maximum approaching 29 – 42 vol% depending on the particle type and resin mixtures due to differences in particle shape and size and resin viscosity. With more magnetic particles, composites had higher magnetic saturation and permeability. Coercivity was not affected by particle loading because there was no change in crystal structure with increased particle loading. Increased particle loadings of up to 80 wt% were attainable by mixing volatile solvent into the particle-resin formulas to decrease the viscosity of the ink. Various compositions of toroids were both molded and printed and then hand-wound to investigate the influence of particle loading on inductor device performance. Generally, increasing particle loading increased inductance due to the increase in magnetic saturation and permeability. The operating frequency does decrease with particle loading due to compounding magnetic hysteresis loss. Inductors were constructed into both a toroid and a cone using 75 wt% FeCo in NEA121 to showcase the difference in behavior with core shape, showing a higher operating frequency with a conical structure due to its orientation away from the substrate minimizing stray capacitance. From these initial studies, it was of interest to explore magnetic inks with higher particle loadings to increase inductance.

3.3 Experimental Methods

3.3.1 Materials

Polyethylene oxide (PEO, MW = 30k g/mol), FeSO4, CoCl2, sodium hydroxide, cyclohexane, hydrazine, argon, DI water, ethanol, acetone, iron (II, III) oxide, hydrous nickel chloride, hydrous ferrous chloride, sodium hydroxide, propylene glycol, NEA121, polyimide, polydimethylsiloxane, tetrahydrofuran (THF), methylene chloride, methanol, and ether.

3.3.2 Methods

FeCo was made in-house following a published protocol [71]. Namely, 8.256 g of polyethylene glycol (PEG-400), 1.251 g of $FeSO_4 \cdot 7H_2O$, 0.357 g of $CoCl_2 \cdot 6H_2O$, 2.964 g of sodium hydroxide, and 0.96 mL of cyclohexane were dissolved in 53.688 mL of DI water and stirred with a magnetic stir rod for 30 minutes at 80°C, capped and under argon. Then, 31.567 mL of 80 wt% hydrazine was quickly injected into the solution, turning the solution from a pink color to a brown, blue, then finally black color. The solution is then transferred to a Teflon-lined stainless-steel autoclave. The autoclave was heated at 120°C for three hours and air-cooled to room temperature. The result is a black magnetic sediment in a clear solution, which was separated using a strong permanent magnet and washed with DI water five times and ethanol five times, and placed in a desiccator to dry. The final product was about 2 g of single phase, cubic FeCo (3:1) with a face length of 150 nm (Figure 1 (a)). These particles were selected for use because of their high saturation magnetization, high permeability, and low coercivity.

Permalloy nanoparticles were synthesized using a procedure from Qin *et al* [72]. The procedure was quadrupled to produce a higher yield at a time, from approximately 0.5 g per synthesis to about 2 g. Hydrous nickel chloride and hydrous ferrous chloride were mixed at a 1:1 molar ratio with 32 g sodium hydroxide in 400 mL of polypropylene glycol. The kinetics of the reduction reaction was just so the final molar ratio of the crystallites is 4:1 nickel to iron ($Ni_{80}Fe_{20}$). The solution was mixed using a mechanical mixing arm at 1300 rpm. The synthesis solution is heated in an oil bath at 80°C for 2 hours to dissolve all the salts and then raised to 180°C for 2 hours for the particles to grow. After allowing it to cool overnight, a cleaning solution of 1:1:1 acetone, ethanol, and DI water was added to the flask and placed in a sonicating bath to dilute and decrease the viscosity of the synthesis solution. A magnet was used to collect the particles and the supernatant was discarded. The cleaning solution was added, and the solution was sonicated, using the magnet to collect the particles and discard the supernatant at least five times. Ethanol was then used an additional five times to wash the particles with the same sonicating and magnet collecting steps and dried in a desiccator overnight. The result was a spherical particle consisting of crystallites with a 250 nm diameter (Figure 3.1 (b)).

Ferrites such as iron (II, III) oxide (Sigma, SEM 50-100 nm) (Figure 3.1 (c)) were used for inductor applications due to their high resistivity, especially at increased frequencies. Purchased from a manufacturer, it was able to be used extensively in prototyping procedures that were then applied to other types of magnetic particles.

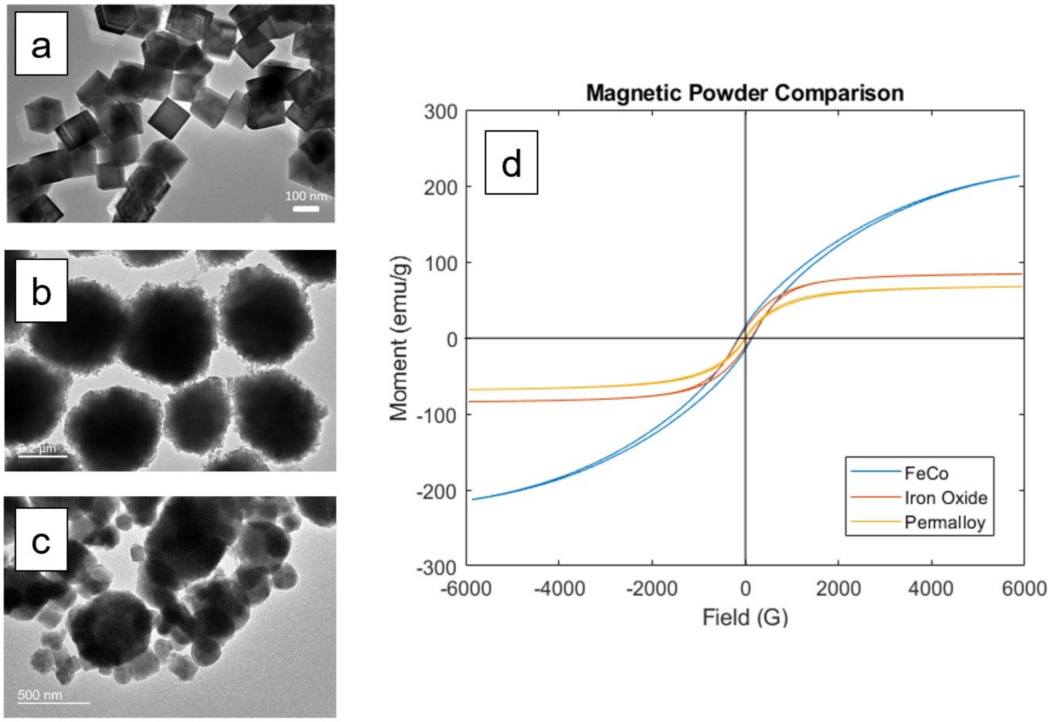

Figure 3.15: TEM images of (a) synthesized cubic FeCo, (b) synthesized spherical permalloy, (c) as purchased iron oxide, and (d) magnetic hysteresis of magnetic materials used in this study acquired with VSM.

NEA121 (Nordland Products, NJ, USA) is a UV and thermally curable electronics adhesive. It is used as an insulation material due to its high dielectric constant ($\varepsilon = 4.04$, $tan\delta = 0.045$ at 1MHz) [73]. It cures by exposing it to UV light or oven curing at 125°C for 16 hours.

Photo-definable polyimide coating (HD Microsystems HD4100) is a photosensitive polyimide resin used in printed packaging applications ($\varepsilon = 3.0 – 4.0$, $tan\delta = 0.02$)[74]. It cures with UV exposure or oven curing at 200°C for 8 hours.

Polydimethylsiloxane (PDMS), (Gelest) is an epoxy resin that cures with added activator at a 10:1 ratio. The reaction takes 24 hours in air to complete ($\varepsilon = 2.75 - 2.64$, $tan\delta = 0.017 - 0.048$) [75].

Mixtures of dry particles and uncured resin were mixed using a planetary centrifugal mixer (ARE-310, THINKY Corporation, Tokyo, Japan). This mixing device allows quick, homogeneous, bubble-free inks to be produced and ready for printing, even at low volumes such as 1mL of ink at a time. Various ratios of particles and resin were mixed to print with, ranging from 50 – 80 wt% until a limit was reached where the particles no longer were wet by the uncured resin after centrifugal mixing. High-volatility solvents such as acetone and methylene chloride were added to improve homogeneity and decrease viscosity to allow printing at higher particle loadings. Inks were loaded into a 3 mL syringe and either connected to a pressurized airline to attach to the 3D printer for automatic deposition or hand extruded into a mold.

3.3.3 Characterization

3.3.3.1 Transmission Electron Microscopy (TEM)

TEM (JEOL JEM 2100 LaB6) was performed to observe magnetic nanoparticle size and shape uniformity as well as the distribution of particles in cured resin. For the powder samples, particles were suspended in a dilute ethanol solution and dropped onto a carbon-coated copper grid. For particles in resin, the cured composite was cut using a microtome to produce a sample thin enough to allow the tunneling of electrons and produce a clear image.

3.3.3.2 Rheology

A rotational and oscillatory rheometer (TA Instruments AR2000, stress-controlled) was used to study the complex rheology of uncured composite inks. Measurements were performed at room temperature using a parallel plate geometry with a plate diameter of 10 mm and a gap size of 1 mm. A solvent trap was used to prevent evaporation of solvents. Complex shear modulus was recorded as a function of angular frequency in the linear viscoelastic regime which was determined by measuring complex modulus as a function of strain.

3.3.3.3 Vibrating Sample Magnetometry (VSM)

Magnetic properties were measured using Vibrating Sample Magnetometry (Hitachi, Japan). Dried powder or cured composite was measured with a magnetic field sweep between -6kG and 6kG. The interpretation of the hysteresis curve is discussed below.

3.3.3.4 Vector Network Analyzer (VNA)

A Vector Network Analyzer (VNA Agilent) was used to measure reflectance parameters (S_{11}) as a function of frequency. From these recorded values complex impedance was calculated. Assuming the constructed device behaves as an inductor and has negligible capacitance below the observed resonant frequency, resistance, inductance, and quality factor was calculated from the impedance. From inductance, permeability was calculated using an equation modeled for cylindrical cores. A discussion of the equations used is found below.

3.3.3.5 COMSOL Multiphysics simulations

Finite element method (FEM) based simulation in COMSOL Multiphysics software is used to predict intrinsic material properties of magnetic-polymer composites of varying compositions. This allows complex devices to be simulated with more accurate results, using manually defined material parameters from these COMSOL calculations. Composite geometries were drawn as spherical or cubic magnetic particles within a polymer block. Particles were placed to realistically resemble disorder within the matrix using MATLAB code to create random position points. The particle fill factor was varied by altering the dimensions of the box matrix.

Chapter 4: Magnetic Ferrite Inks for Syringe Printable Inductors

4.1 Introduction

The technique of additive manufacturing (AM) has the potential to simplify fabrication processes, constructing complex shapes using a single apparatus by exchanging the printable material at the print head. The ability to extend this technique to magnetic materials will accelerate material discovery to produce passive electronics with greater efficiency through rapid prototyping, increasing the speed of communication in electronics to keep up with current integrated circuit advancements. Electronic circuitry consists of various types of materials, such as conductive metal wiring, insulating plastic packaging, and magnetic components. Magnets specifically are essential in electronic devices, being used in applications for generators, transformers, inductors, and magnetic recording devices [76]–[78]. Subtractive manufacturing techniques can result in up to 25% material waste in addition to being limited in shape design [2]. Magnetic materials often include precious metals, for example, neodymium and cobalt, which are expensive and difficult to supply [79]. Through AM, money can be saved and material less wasted in fabricating these types of devices [2].

Formulating optimal samples and a procedure for printing magnetic inks is a challenge, especially when it applies to a high volume fraction of magnetic material within the final product. There are few extensive studies on high nanoparticle volume fraction magnetic inks and fewer with realistic commercial applications. Magnetic nanoparticle inks can be printed by incorporating them in a thermoplastic like polyamide or a curable epoxy resin such as polydimethylsiloxane which acts as a viscosity modifier or binder [80]–[82]. Chenglin Yi et al [69] report on the versatility of this method, showcasing cone-shaped inductors with multiple types of magnetic-polymer composites. However, the nanoparticle content is greatly limited by the high viscosity of those organic binders to a maximum final volume of 40 vol% magnetic material [69]. In an alternative fabrication method, magnetic particles are mixed in UV curable resins for vat polymerization, which is a method that additively manufactures (3D prints) by UV polymerization within a pool of liquid monomer, but the particle loading is once more limited due to light scattering [78]. Direct-write printing is a method of additively fabricating three-dimensional structures by extruding high-density colloidal solutions consisting of typically more than 50 vol % nanoparticle content, < 1 vol % particle coatings or polymer binder, and the remaining amount being a volatile solvent that is removed via evaporation from the final product [83]. The ink design presented here incorporates a high-density, syringe printable, magnetic ink that has a particle loading of 40 vol% while printing, where after extrusion the solvent evaporates to leave behind a high-density magnetic part with ~90 vol% magnetic material and only ~10 vol% polymer material.

Rheological studies are used to quantify optimal yield stresses that result in minimized slumping behavior and shape retention of the printed part [84]. The rheological behavior of the colloid must lend itself to its ease of extrusion while still maintaining mechanical integrity after the deposition of several layers, requiring it to exhibit shear-thinning behavior at the nozzle. This specific rheological behavior is influenced by the interaction between the dominant particle forces of these compositions. The particle assembly is a result of hydrophobic interactions, hydrogen bonding, and electrostatic attraction, which is competing with electrostatic repulsion [85]. Shear-thinning occurs because these forces are weak against applied shear-stresses [86]. Particle-solvent interactions are controlled by tuning the method of stabilization and modifying the particle surface chemistry. The degree of stabilization of solutions alters the printability of the ink and the final shape of the product after the solvent is evaporated.

Suspensions typically used to explore direct-write printing ink development consist of a nanoparticle powder, a polyelectrolyte dispersant that coats the nanoparticles, and a rheology modifier that increases the viscosity and allows printing of a defined shape. In this study, magnetic iron oxide ($Fe_2O_3 \cdot FeO$) and MnZn doped ferrite nanoparticles were stabilized with the anionic polyelectrolyte poly(acrylic acid) (PAA), which has been used before as a dispersant in colloidal inks [87]–[89]. The stabilized particles were then suspended in an aqueous polymer solution which acts as the rheology modifier, to achieve an ink that solidifies as the solvent evaporates after deposition. An optimal degree of flocculation is required for the ink to exhibit a yield stress. A completely stabilized solution with no yield stress will not retain its shape after deposition and is not desirable for printing [90], [91]. The rheological behavior desired is that of a shear-thinning fluid with a yield stress, which may be attributed to slight flocculation of the particles. J.A. Lewis et al. have shown that free polymers may either promote flocculation or stabilization (dispersion) depending on the initial conditions of particle stability [92] and that for printable inks, it is intended to use free polymers to induce slight flocculation [93]. Flocculation due to a free polymer induces a high yield stress without significantly affecting the viscosity. Particles coated insufficiently (< 75% coverage saturation limit) comparatively induce irreversible flocculation that results in a much higher viscosity but insufficient yield stress [94]. This could be a possible explanation for our print behavior, but it has not been able to be verified experimentally.

Tuning ink flow requires tuning the balance between repulsive, stabilizing forces and attractive networking forces within the ink solution. Repulsive forces prevent clogging at the nozzle while attractive forces produce a yield stress allowing shape retention and the possibility of spanning elements [95]. The challenge arises in understanding repulsive and attractive potential effects, and drying stresses in concentrated solutions, as well as ink flow in reduced nozzle diameters. The goal of this study is to elucidate the roles that particle stability and free polymer molecular weight have on the printability of magnetic polymer composites, using iron oxide as a template material and MnZn-doped ferrite to exemplify the possible translation of the ink formula used to other iron oxide materials for the ability to tune magnetic properties and device performance. The printed MnZn-doped ferrite device is tested as an inductor to exhibit potential applications of this fabrication technique. Understanding the fundamental mechanism of what constitutes a successful, syringe-printable magnetic ink will allow this ink formulation technique to span across several classes of electronic devices.

4.2 Results & Discussion

4.2.1 Fabrication of syringe-printed magnetic inks

Iron (II, III) oxide ($Fe_2O_3 \cdot FeO$), referred to in this work as iron oxide, and MnZn doped Ferrite nanoparticles were stabilized with an anionic polyelectrolyte (poly(acrylic) acid (PAA)) and suspended in aqueous polyethylene oxide (PEO)) and glycerol solution to produce a shear-thinning high-volume fraction ink that can be printed with a syringe printer. As water evaporated after deposition, the solidified part had a high concentration of magnetic material (>90 vol% solids loading) and minimal organic material (<0.6 vol% while printing and <10 vol% while dry) for an increased magnetic response when used as a magnetic inductor core.

4.2.2 Ink formulation and preparation

Iron oxide and MnZn doped ferrite particles were coated with PAA ammonium salt (PAA-NH_4) in excess using a process as shown in Figure 4.1 (a). The polymer layer formed on the particles is compact and uniform as observed by TEM (Figure 4.2 (b), (e)). It is important to have the optimal concentration of stabilizing polymer on the particle. If not enough PAA is used, then the coating will not be uniform and repulsion between particles will not be strong enough to stabilize them in the aqueous suspension. If too much PAA is used, the excess polymer will cause the particles to crowd and precipitate from the suspension. The particles did not homogeneously disperse until the excess PAA is removed (Figure 4.1 (b)). If the particles are not adequately coated and stabilized, clogging occurs at the nozzle and printing is impossible. The surface charge of the particles changes with the optimal adsorption of PAA as observed by zeta potential measurements (Figure 4.2 (c), (f)). At pH 7, the surface charge is -30 mV and -48 mV for iron oxide and MnZn doped ferrite, respectively. After the PAA coating procedure, the surface charge is -48 mV and -56 mV respectively. The PAA on the iron oxide and MnZn ferrite surface is dissociated at pHs beyond 7 to produce a stronger negative zeta potential. At increased magnitudes of surface charge, there is more electrostatic repulsion to repel the particles from one another and prevent flocculation. A possible explanation for the adsorption of PAA to iron oxide is by chemisorption, with the most probable interaction being from chelation [96].

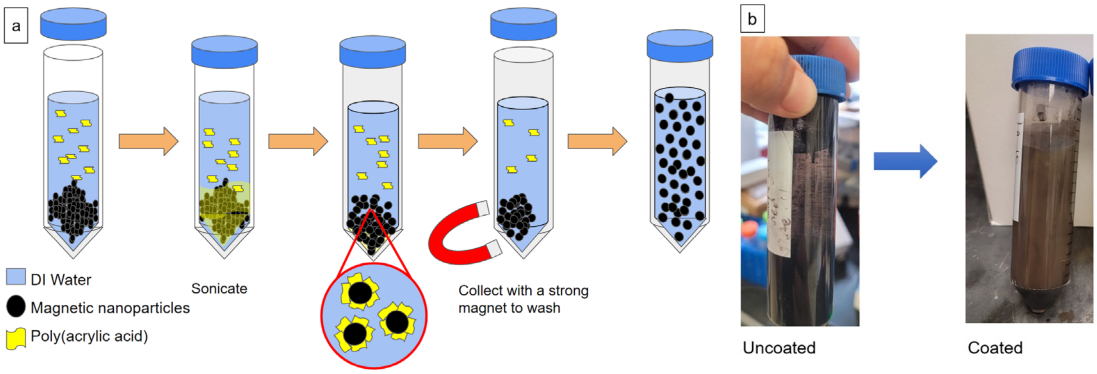

Figure 4.1: (a) Schematic of coating iron oxide with polyacrylic acid (Darvan), and (b) solution of uncoated iron oxide is inhomogeneous, but after sufficiently coating is stable in solution.

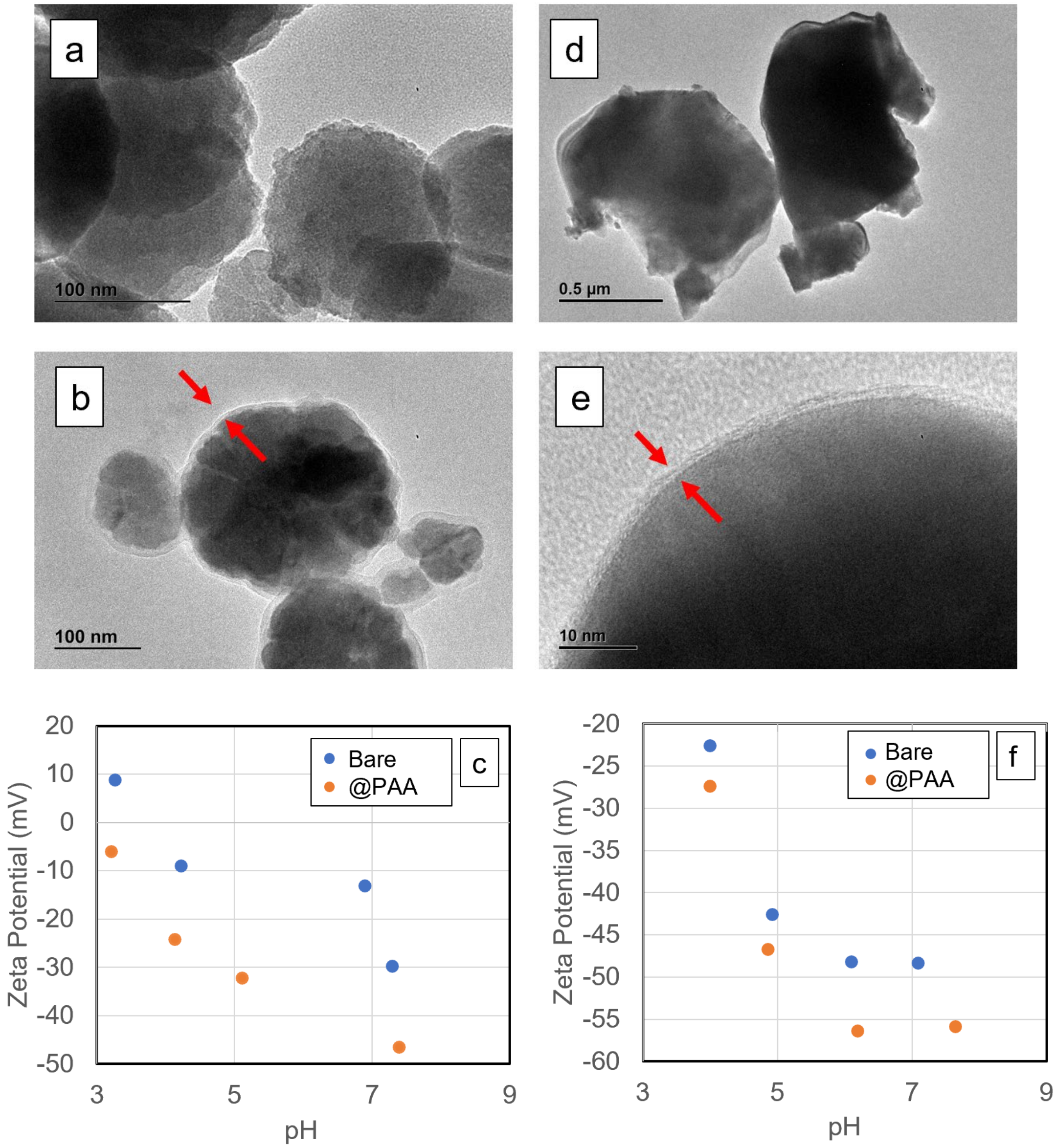

Figure 4.2: TEM image of (a) uncoated and (b) PAA-coated iron oxide and (c) its zeta potential without (blue) and with (orange) its PAA coating. TEM image of (d) uncoated and (e) PAA-coated MnZn doped ferrite and (f) its surface zeta potential without (blue) and with (orange) its PAA coating.

The PAA-coated iron oxide particles were resuspended in a solution of PEO, glycerol, and DI water (Figure 4.3 (a)), which produced a weakly flocculated suspension that was observed as a loose, fluffy sediment (Figure 4.3 (b)). The same behavior was observed with excess PAA in solution before the polyelectrolyte was washed in the previous coating step. This observed behavior could be the result of depletion flocculation [92], [97], [98], a volume exclusion effect that causes crowding of the particles, although more studies should be performed to confirm whether this phenomenon is the cause of its settling behavior. The polyelectrolyte layer was still sufficient to prevent particles from forming large clusters that would clog the nozzle during printing, but the weak flocculation formed an attractive network that kept the deposited part intact. The free polymer network was not rigid and was overcome to allow the print to flow with applied shear stress. To produce the ink, solutions were concentrated via centrifugation for a particle loading between 37.5-45 vol%. Inks were shear-thinning, remaining solid at rest and acting as a fluid after an applied stress beyond the threshold yield stress. The ink experienced a quick recovery due to the attractive interparticle network, allowing shape retention after deposition which was observed in the printed part as no sagging between layers.

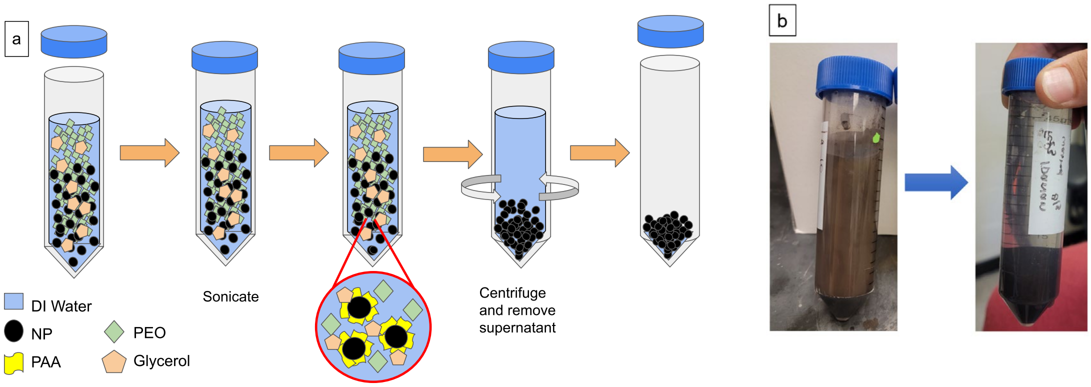

Figure 4.3: (a) Schematic of iron oxide ink-making process. NP refers to "nanoparticles", either iron oxide or MnZn-doped ferrite. (b) Iron oxide weakly flocculating with the addition of the PEO free polymer.

4.2.3 Ink flow properties

The ink must remain extrudable during the time required to print. Inks were prepared in an aqueous solution where water was the solvent, and water evaporated spontaneously in ambient air. Adding a solvent with a lower rate of evaporation can reduce the speed at which the solvent leaves the ink while printing. In this study, glycerol was included in the water solvent to slow down the evaporation rate and extend the window of time available for printing. Figure 4.4 shows photos of printed iron oxide toroids with varying concentrations of glycerol in the aqueous solvent. Increasing the glycerol concentration increased the viscosity and extrusion became more irregular. At a 50% glycerol concentration, the ink was stringy, resisted extrusion with applied pressure, and flowed once the pressure was removed. This inconsistent print flow was suspected to be because the ink is shear-thickening, resisting flow with applied pressure and then extruding uncontrollably once the shear stress was removed.

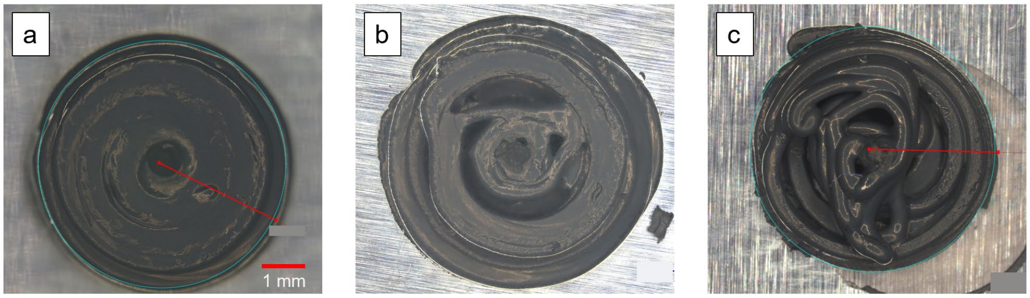

Figure 4.4: Five layers of iron oxide inks printed into a cylindrical shape with (a) 10% (b) 30% and (c) 50% aqueous glycerol solution as the ink solvent.

Rheological analysis was used to study the effect of the inclusion of glycerol in an iron oxide nanoparticle ink. The ink tested with no glycerol and a particle loading of 41 vol% (Figure 4.5 (a)) had a dominating shear storage modulus with a value approaching 10^7 Pa. Inks tested with 10% aqueous glycerol solution (Figure 4. 5 (b)) had a much lower and more easily displaced storage modulus between 10^3 – 10^4 Pa that was overcome by the loss modulus at the yield shear stress, despite having a higher particle loading than the ink tested with no glycerol (45 vol%). The ink with no added glycerol acted as a solid at all exposed shear stresses. Glycerol acts as a lubricant, allowing inks to print with higher particle loading compared to samples made without it. Inks with glycerol were much more easily extruded through the print nozzle while still having shape-retentive properties, and the issue of premature evaporation was addressed.

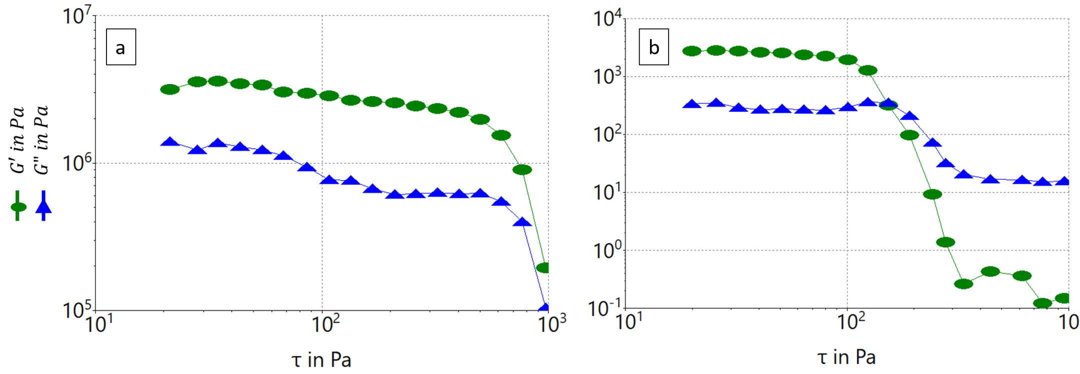

Figure 4.5: Rheological performance of (a) 41vol% iron oxide ink with no glycerol and (b) 45vol% iron oxide ink with 10% aqueous glycerol solvent under increasing shear stress.

Particle loading affects viscosity and retention of print shape. Inks with a 41 vol% iron oxide particle loading printed consistently, with no change in viscosity over time and no clogging at the nozzle tip. With added printed layers, there was no sagging. Each consecutive layer retained its original printed height (Figure 4.6 (a), (b)). Inks tested with higher particle loadings were not extrudable through 22 G or 18 G nozzles.

Samples with lower particle loadings did not retain their shape with added layers and deformed under the stress. (Figure 4.6 (e), (f)). The yield stresses of the inks were characterized using a shear rate ramp test. The ink with a higher particle loading had a higher yield stress (Figure 4.6 (c), (g)). The 41 vol% ink sample had a yield stress of 150 Pa compared to the 37.5 vol% sample which had a yield stress of 50 Pa. The creep test (Figure 4.6 (d), (h)) showed that the ink with a higher particle loading can recover after three minutes of constant deformation. The 41vol% sample only deformed 0.065% with 100 Pa constant shear stress and recovered to 0.03% after the stress was removed. The 37.5 vol% sample was sheared to only 50 Pa and deformed over 90%. The material did not recover after the removal of the stress. The higher particle loaded sample had a stronger internal network that repaired itself after displacement, while the lower particle-loaded sample was unable to recover, resulting in sagging.

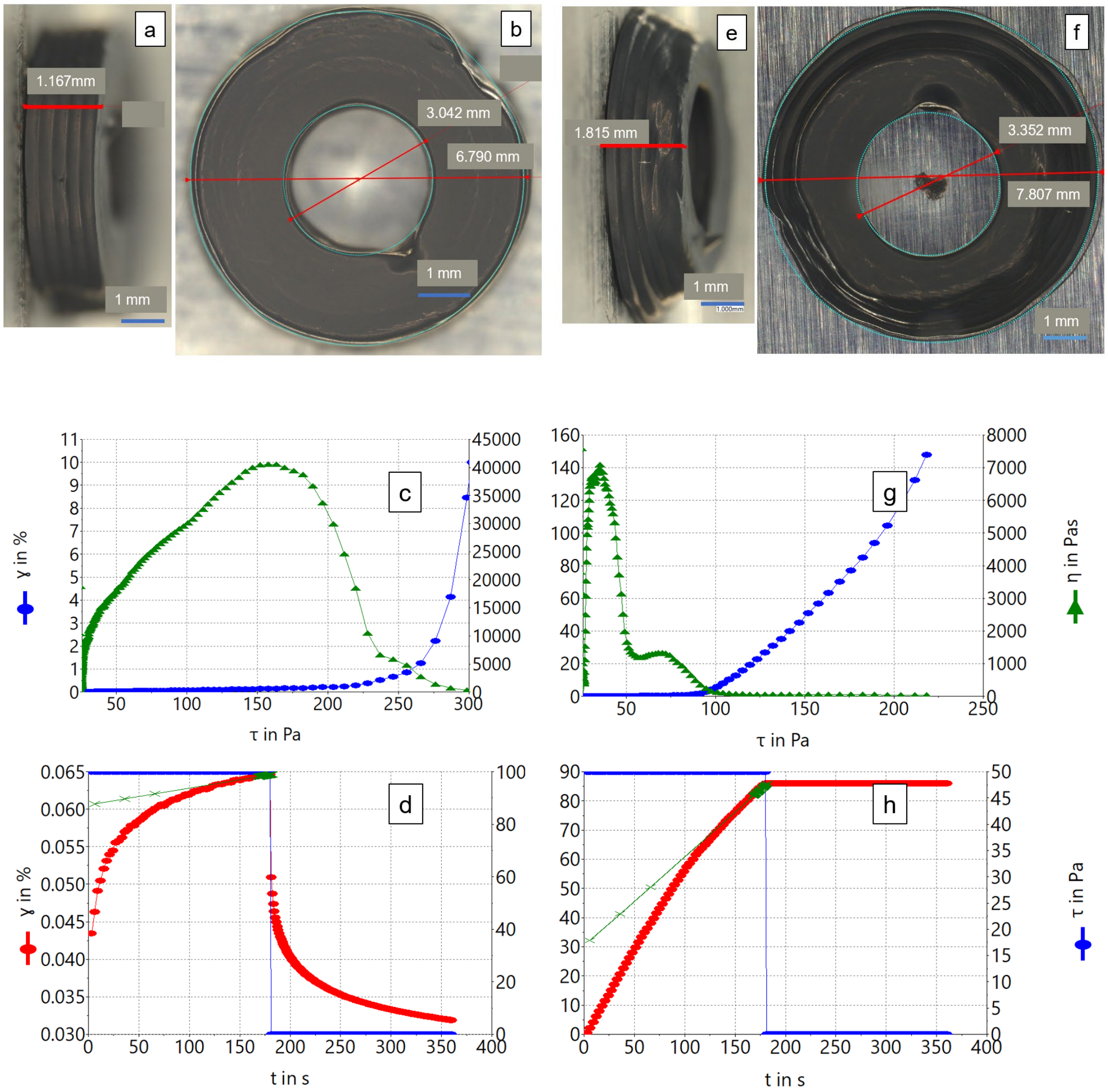

Figure 4.6: (a) Side view and (b) top view of printed iron oxide toroid, (c) strain sweep, and (d) creep test of with 41 vol% solids loading ink. (e) Side and (f) top view, (g) strain sweep, and (h) creep test of 37.5 vol% solids loading ink.

The flow properties and printed ink shape varied as a function of free polymer molecular weight. All samples tested had the same added concentration of PEO at approximately 1.8 wt% per mass of iron oxide powder. The sample with 3k MW PEO had defined layers and sharp edges. Flow properties characterized with a shear stress sweep showed liquid-dominating behavior at all tested stresses, which resulted in a consistent print (Figure 4.7 (a), (d)). The toroid printed with 30k PEO retained its shape and kept its height with added layers, but the ink was tackier and trailed with the moving nozzle. The rheology showed that samples with a higher molecular weight exhibited a gel network that had solid dominating behavior at low stresses but yielded with sufficient applied force to flow uniformly while printing (Figure 4.7 (b), (e)). The 600k PEO had a much higher viscosity and inconsistent flow, with the resulting shape deviating from the tool path. The high MW ink had a stronger network with dominating solid behavior that deformed and yielded without breaking its network (Figure 4.7 (c), (f)). The effect of polymer molecular weight in aqueous solutions has been studied to better understand droplet formation for 3D printing technologies, such as jet printing or aerosol printing. It has been found that increasing the molecular weight of the polymer in solution increases the breakup length of the jet or decreases the frequency of droplet formation. This has been explored specifically for PEO solutions and can be used as a probable explanation for the stringiness of the filaments observed with increasing PEO molecular weight in this study [99], [100].

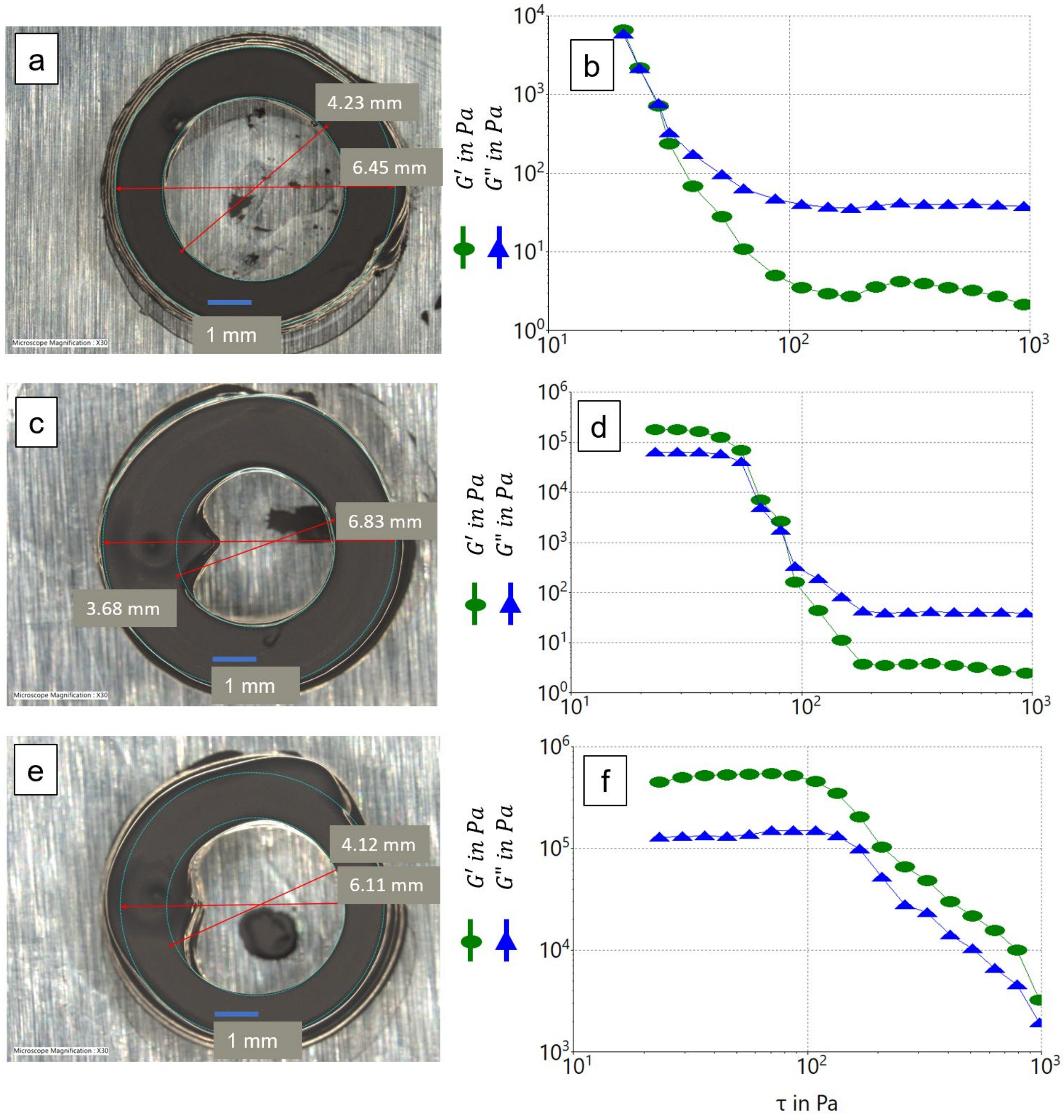

Figure 4.7: (a, c, e) Top view of printed iron oxide toroid and (b, d, f) oscillatory stress sweep of iron oxide ink with (a, b) 3k, (c, d) 30k, and (e, f) 600k MW PEO.

4.2.4 Crystal structure and magnetism changes with sintering

Printed toroids were placed in an oven for 3 hours at 80°C to remove water. The dried samples became brittle and delicate, making the construction of a sample difficult without breaking the printed part. Dried toroids were then sintered to densify in an attempt to improve magnetic and mechanical properties [101]. The volume change upon drying was not measured, but understanding the change in volume with the removal of the solvent could help explain the brittle nature of the dried material.

Iron oxide toroids did not show a significant change in magnetic properties after sintering at low temperatures. Sintering even at 500°C for two hours only decreased the magnetic saturation and relative magnetic permeability (μ_r) by a small amount. Sintering above 800°C, however, even for only a few minutes, nearly eliminated the magnetic properties of the toroid. Mechanical properties did not improve until sintered at temperatures above 800°C, but due to the loss of magnetic properties, the inductance of a constructed device was not improved from the inclusion of the magnetic toroid sintered at this temperature.

MnZn Ferrite printed toroids did not show a change in magnetic properties when sintered at 1050°C compared to the powder as received (Figure 4.8). It was not until sintered at 1400°C that the magnetic properties improved [102], [103]. After sintering, the MnZn doped ferrite toroid had significantly increased magnetic saturation and permeability. Sintering the toroid at 1400°C produced the same magnetic properties regardless of whether it was sintered for two or four hours. The sintered material had negligible coercivity, which is beneficial for its application as an inductor.

Table 4.1: Magnetic properties of MnZn doped ferrite as a function of sintering temperature and oven time

Sample	***T* [°C]**	**Time [hr]**	**B_{max} [T]**	**H_C [Oe]**
Unsintered	0	0	0.005	96
1050°C	1050	4	0.02	54
1400°C 2hr	1400	2	0.4	4.8
1400°C 4hr	1400	4	0.4	7.6

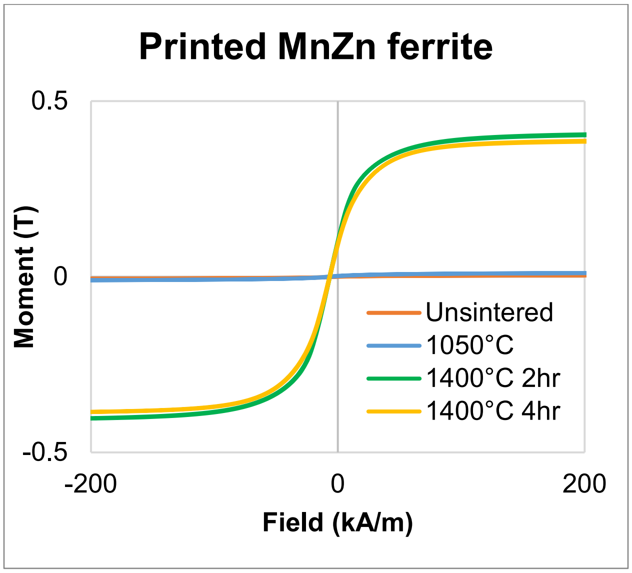

Figure 4.8: VSM of MnZn doped ferrite before and after sintering at 1050°C for two hours and 1400°C for two and four hours

The morphology of MnZn ferrite changed after sintering at 1400°C. The pure powder imaged with SEM shows individual particles that range from submicron to 2 μm in diameter (Figure 4.9 (a)). After sintering there were no longer distinct particles but rather a continuous, crystalline structure (Figure 4.9 (b)). EDS was used to measure the atomic ratio of the Zn:Mn:Fe composition in the sintered and unsintered samples. These values were used as a reference to fix the composition during the Rietveld analysis. Both diffraction patterns were matched to the spinel and hematite phases, suggesting that the as-received powder is a blend of Fe_2O_3 and doped ferrite. Both diffraction patterns fit the spinel phase with the fixed composition of $Zn_{0.5}Mn_1Fe_{1.5}O_4$ [104] and a hematite phase with a fixed composition of $Fe_{1.82}Mn_{0.18}O_3$ [105]. EDS of the unsintered sample did show a higher Mn content than the sintered material which indicated a possible third phase (marked with '*' in Figure 4.9 (c)) mixed within the powder. After sintering there was a higher fraction of the spinel phase at 86 wt% and a reduction of the hematite to 14 wt%. The increase in magnetic properties of this material after sintering was likely due to the increase in the magnetic spinel crystal structure and reduction in weakly magnetic hematite structure.

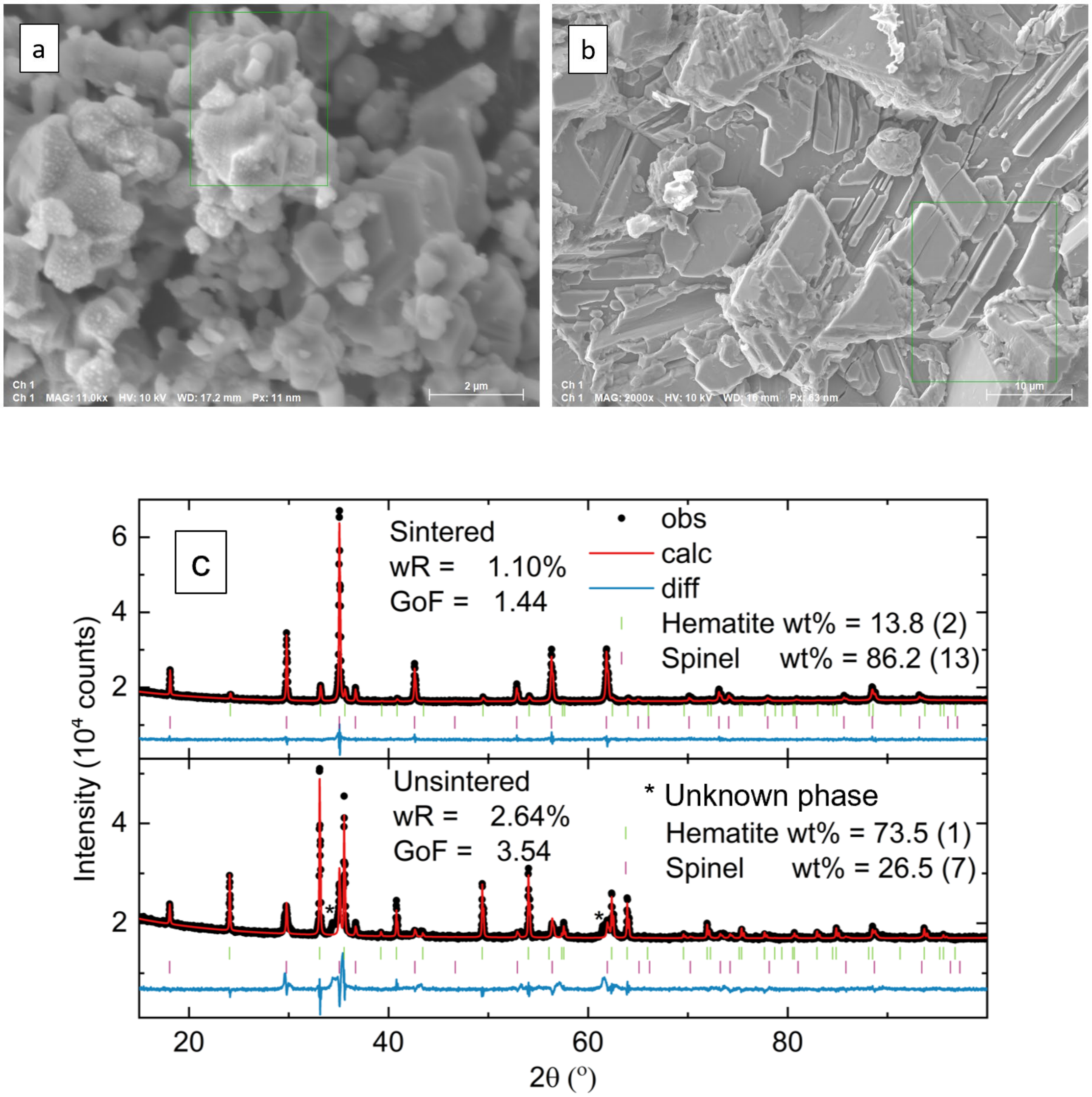

Figure 4.9 SEM of (a) unsintered and (b) sintered printed MnZn ferrite toroids. (c) Rietveld refined XRD patterns of sintered and unsintered MnZn ferrite.

Table 4.2: Atomic positions from Rietveld analysis of sintered MnZn-doped ferrite

Sintered				
EDS atomic %	**Mn**	**O**	**Zn**	**Fe**
	17.34	46.3	8.08	28.28
Spinel phase	**composition**	**Space group**	**Lattice parameter *a***	
	$Zn_{0.5}Mn_1Fe_{1.5}O_4$	Fd-3m (227)	8.4796(1)	
Atomic position	**x**	**y**	**z**	
Mn^{3+}	0.5	0.5	0.5	
O^{-2}	0.26091	0.26091	0.26091	
Zn^{2+}, Mn^{2+}	0.125	0.125	0.125	
Fe^{3+}	0.5	0.5	0.5	
Hematite phase	**composition**	**Space group**	**Lattice parameter *a***	**α**
	$Zn_{1.82}Mn_{0.18}O_3$	R-3c (161)	5.4241(7)	55.321(14)
Atomic position	**x**	**y**	**z**	
Mn^{3+}	0.1461	0.1461	0.1461	
O^{-2}	0.92958	0.57042	0.25	
Fe^{3+}	0.1461	0.1461	0.1461	

Table 4.3: Atomic positions from Rietveld analysis of unsintered MnZn-doped ferrite

Unsintered				
EDS atomic %	**Mn**	**O**	**Zn**	**Fe**
	10.21	53.01	7.04	29.74
Spinel phase	**Composition**	**Space group**	**Lattice parameter *a***	
	$Zn_{0.5}Mn_1Fe_{1.5}O_4$	Fd-3m (227)	8.4580(4)	
Atomic position	**x**	**y**	**z**	
Mn^{3+}	0.5	0.5	0.5	
O^{-2}	0.27659	0.27659	0.27659	
Zn^{2+}, Mn^{2+}	0.125	0.125	0.125	
Fe^{3+}	0.5	0.5	0.5	
Hematite phase	**composition**	**Space group**	**Lattice parameter *a***	**α**
	$Zn_{1.82}Mn_{0.18}O_3$	R-3c (161)	5.4235(24)	55.312(3)
Atomic position	**x**	**y**	**z**	
Mn^{3+}	0.14551	0.14551	0.14551	
O^{-2}	0.94199	0.55801	0.25	
Fe^{3+}	0.14551	0.14551	0.14551	

4.2.5 Inductor Characterization

After printing and sintering at 1400°C, MnZn doped ferrite toroids were hand wound with 12 turns using 130 µm conductive copper nickel alloy wire. The wound toroid was mounted to a substrate and the wire was soldered to an SMA connection (Figure 4.10

(a)). The assembled device was attached to a VNA, and the reflectance parameters (S_{11}) were recorded as a function of frequency. The same was done with a polymer core of the same dimensions to compare performance.

By utilizing reflectance measurement techniques, the impedance value was successfully transformed into its corresponding resistance and reactive components. By referring to the inductor's equivalent circuit [9,25], we were able to approximate the parasitic capacitance and resistance to be a few pF and less than 5 Ω, respectively. Using the values obtained, further circuit simulations revealed that the parasitic capacitance impedance can be ignored when the frequency is below 10 MHz because it is much lower than the self-resonating frequency (SRF). As a result, we can assume that the capacitance can be ignored and proceed to estimate the inductance accordingly.

The inductance calculated from the recorded reflectance of the inductor with the sintered MnZn ferrite core is 4.26 μH at 7 MHz, which is a degree of magnitude below its resonant frequency of 70 MHz (Figure 4.10 (b)). Due to the dispersive behavior of the magnetic material, the permeability and therefore inductance decreases as a function of frequency. The wound toroid with the polymer core has a much lower inductance of only 0.08 μH. The high magnetic permeability of the sintered MnZn ferrite material increases the inductance compared to the polymer core.

The resonance is a result not only of the material within the core but also of the construction of the device itself. The toroid shape placed flat on the substrate produces parasitic capacitances. If the inductor were instead constructed in a conical shape, for example, and oriented away from the substrate, there would be less coupling between the windings and the substrate, less parasitic capacitance, and the device would have a higher resonant frequency and operate at higher frequencies. A future direction of this work is to be able to construct an inductor in the conical shape [69] or in other shapes inducive to operation at high frequencies [54].

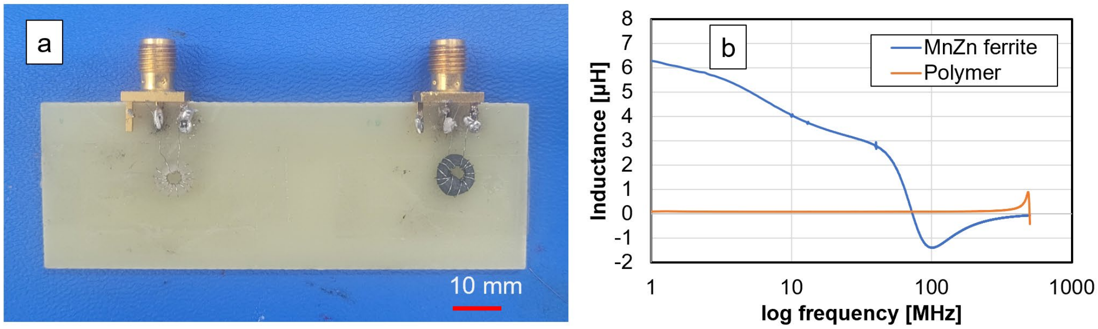

Figure 4.10: (a) Hand-wound and soldered polymer and MnZn ferrite toroids and their (b) inductance as a function of frequency.

Table 4.4: Inductance properties of toroids with polymer and sintered MnZn ferrite cores with 12 windings. L, A_L, L vol^{-1}, Q, and μ_r values were reported at 7 MHz.

	L **[μH]**	***N***	***A_L*** **[nH N^{-2}]**	***L*** **vol^{-1} [nH mm^{-3}]**	***μ_r***	**SRF [MHz]**
Polymer core	0.08	12	0.05	0.22	1	498
Sintered MnZn doped ferrite core	4.26	12	2.96	12.2	85	70

4.3 Conclusion

Ferrite-based nanoparticle inks were fabricated using iron oxide as a model and MnZn ferrite as an example of the ink composition used in this study being translated to other ferrite materials. Both iron oxide and MnZn doped ferrite particles were stabilized by coating with poly(acrylic acid) (PAA) in excess. Particle stability is an essential requirement to produce printable ink. The effect the molecular weight of the free polymer poly(ethylene oxide) (PEO) had on ink flow is observed. Of the molecular weights tested, 30k PEO had the most regular print with no tackiness and adequate shape retention. Shape retention and recoverability of ink as a function of particle loading was explored, with too little resulting in a messy print and too much being impossible to extrude. The optimal amount for the iron oxide ink system was 41 vol%. Premature evaporation of the solvent was resolved using a solvent blend of water with glycerol, which has a higher evaporation rate, and the optimal concentration of 10% glycerol in water was determined. MnZn doped ferrite inks were printed into toroids and sintered to 1400°C for 2 hours to increase relative magnetic permeability from $\mu_r = 1$ to $\mu_r = 85+$ for enhanced device performance compared to unsintered toroids and undoped iron oxide inks. The sintered MnZn ferrite toroids were constructed into toroids and their inductance and device efficiency were measured and compared to a toroid with a polymer core with no magnetic properties. The toroid with the magnetic core had an inductance of 4.26 μH at 8.5 MHz, a magnitude higher than the polymer core which had an inductance of 87 nH at the same frequency. This study lays out a template for ferrite inks with the potential to be fabricated into useful passive electronic devices.

4.4 Experimental Methods

4.4.1 Sample preparation

Iron (II, III) oxide (Sigma Aldrich, 99.99% trace metals basis), MnZn doped Ferrite (MN60, National Magnetic Group, Inc.), Darvan 821-A (Vanderbilt Minerals, 40% ammonium poly(acrylic acid) (PAA) solution), Polyethylene Oxide (PEO) MW 6k, 30k, 6000k (Sigma Aldrich), glycerol, deionized water, Potassium nitrate (Sigma).

PAA solution was prepared by adding PAA (0.375mL Darvan^{TM} solution) to de-ionized (DI) water (40 mL). Iron oxide or MnZn ferrite powder (3 g) was added to the solution and sonicated in a sonicating bath for 1.5 hours at 15-minute intervals to vortex in between. A magnet was used for the iron oxide particles and a centrifuge was used for the MnZn ferrite to collect the coated particles. The supernatant with unadsorbed polymer was discarded. DI water was used to wash the particles of excess PAA five times.

The PEO solution was prepared by adding polymer powder to DI water (350mg/5mL). Polyelectrolyte-coated particles were resuspended in a solution of PEO solution (5mL) and a 10% glycerol-DI water mixture (35 mL). The solution was sonicated for an hour at 15-minute intervals to homogenize and left to sit overnight. Solutions were then centrifuged for 15 minutes at 7800 rpm to achieve a particle concentration of approximately 80 wt%. The supernatant was reserved to alter the particle loading of the ink if necessary.

A HAAS^{TM} 5-axis milling machine has been converted into an additive manufacturing tool. The concentrated nanoparticle ink was transferred into a 3-cc syringe barrel with a plunger and attached to a pressurized airline. The barrel was mounted to the 3D printer. A computer-aided design (CAD) program was used to create the print tool path and converted to G code for automated deposition of the ink into a toroid shape. The ink was printed on a glass slide covered with aluminum foil for easy removal of the dried toroid. A 22 G nozzle (0.4 mm inner diameter) was used for all inks. The pressure required for deposition was within 5-80 psi, depending on the viscosity of the ink. The nozzle speed was kept constant with the printed extrusion volume modified by changing the extrusion pressure. Height was achieved by moving the nozzle up and printing layer-by-layer.

Toroids were sintered using a Nabertherm 1600°C High-temperature furnace (model LHTC(T) 03/16) sintering oven. The rate of heating used was 450°C hour^{-1}. Toroids are held at 700°C for one hour to burn off polymer, and then held at 1050°C for four hours, 1400°C for two hours, and 1400°C for four hours.

4.4.2 Material Characterization

4.4.2.1 Zeta potential

The Malvern^{TM} Zetasizer was used for to study the surface charge of particles coated with polymer. A dilute solution of particles in KNO_3 (10 mM) salt solution was created. The pH of the nanoparticle suspension was adjusted using nitric acid (0.01 M) added dropwise. Particles were analyzed in triplicate in a pH range between 3-8. The pH was measured directly before taking the zeta potential measurement to ensure accuracy.

4.4.2.2 Rheology

Inks are characterized using a dynamic rotational and oscillatory rheometer (HAAKE MARS iQ). Measurements were performed at room temperature using a parallel plate geometry with a diameter of 25 mm and a gap size set to 0.5 mm. A solvent trap was used to limit evaporation.

Shear rate ramp and shear stress ramp tests were performed to investigate shear thinning behavior. The recoverability of the ink was assessed using a creep test, holding at the yield stress for 180 seconds and then removing the stress for 180 seconds. The percent recovery of viscosity within the first 30 seconds was determined as the shear recoverability.

An amplitude sweep was performed to identify the linear viscoelastic region (LVR). The yield stress was defined as the cross-over point between the elastic and storage modulus as a function of yield stress. The frequency sweep was analyzed at a range of 1 to 100 rad s^{-1} within the LVR range. Storage and loss moduli were calculated as a function of frequency.

4.4.2.3 Transmission and Scanning Electron Microscopy (TEM, SEM)

TEM (JEOL JEM 2100 LaB6) and SEM (Hitachi SU-70) were performed to visualize the shape, size, and morphology of bare particles, polymer coatings of particles, and printed devices before and after sintering. Particles were suspended in a dilute ethanol solution and dropped onto a carbon-coated copper grid for TEM imaging. For SEM, samples were stuck using carbon tape and platinum coated to prevent charge build-up during imaging. Energy dispersive X-Ray spectroscopy (EDS) was used to quantify the elemental content of samples.

4.4.2.4 X-Ray Diffraction (XRD)

The crystal structures of iron oxide and MnZn ferrite particles were evaluated using copper-sourced powder X-Ray diffraction (Bruker D8). To determine the change in weight fraction of phases before and after sintering the Rietveld analysis method was used to determine the crystal structures present in the samples using the GSAS-II software [106].

4.4.2.5 Magnetic properties

Magnetic properties were measured using a Vibrating Sample Magnetometer (VSM, Hitachi, Japan). Printed material was dried and crushed into a powder to measure DC magnetic properties. A magnetic field was cycled from 4 kG down to -4 kG, and up to 4 kG again. The area within the curve is integrated to calculate the magnetic hysteresis loss. The slope is calculated to determine the maximum direct current (DC) relative permeability.

4.4.2.6 Inductance properties

A Vector Network Analyzer (VNA, Agilent) that sweeps between 1 kHz to 1.5 GHz using an SMA connection was used to measure reflectance (S_{11}) at high frequencies, in which complex impedance and therefore total resistance and inductance can be calculated. Reflectance is described using scattering-parameters or S-parameters, which illustrate the way a traveling wave responds to an obstruction or passage over a material of differing properties. S-parameters are the ratio of reflected (*b*) to the incident (*a*) complex power waves, which are defined by Kurokawa as a function of wave number, voltage, impedance, and current [107].

$$a = \frac{V+ZI}{2\sqrt{|Re\ Z|}},\ b = \frac{V-ZI}{2\sqrt{|Re\ Z|}}, \tag{1}$$

where *V* and *I* are the voltage and current flowing in the port of a junction, and *Z* is the impedance.

Describing waves is more accurate at high frequencies than describing voltage and current, which in this feedback loop, are constantly readjusting. A scattering wave is recorded as a magnitude and phase at a sweep of frequencies to be converted to a complex value from which complex impedance can be extracted. This relationship is made because the transmission line is terminated by a matched load where the system impedance of the VNA is engineered to be the real value Z_0= 50. Using the relationship of $S = b/a$ and $V = Z_L I$, S_{11} can be expressed in terms of impedances:

$$S_{11} = \frac{Z_L - Z_0}{Z_L + Z_0} \tag{2}$$

where Z_L is the incident impedance.

Impedance is defined as opposition to current flow. As a complex number, it is a sum of the dissipative equivalent circuit resistance and energy storage observed as a phase change. Imaginary impedance encompasses all energy storage components, both inductive and capacitive, with inductive behavior dominating at frequencies below resonance and capacitive behavior dominating at frequencies above resonance. The resonant frequency is dependent on inductance and capacitance with the following relationship:

$$\omega_0 = \frac{1}{\sqrt{LC}} \tag{3}$$

where ω_0 is the resonant frequency, L is inductance, and C is capacitance.

From the reflectance data, we can observe the resonant frequency and calculate the value of inductance at frequencies below resonance. We can also calculate the Q factor, which is the ratio of stored to dissipated energy, or the ratio of imaginary to real impedance.

$$Z_L = R + jX_L, where\ X_L = \omega L, and\ Q = \frac{X_L}{R} \tag{4}$$

where R is resistance, ω is the angular frequency, X_L is inductive reactance, L is inductance, and Q is the quality factor.

The inductance of an inductor device is directly related to the permeability of the material within the core. From the definition of inductance and using the known dimensions of the toroid shape, the inherent permeability of a toroidal core was calculated:

$$L = \frac{\mu_0 \mu_r N^2}{2\pi} h \ln\left(\frac{r_0}{r_i}\right) \quad (5)$$

where L is inductance, μ_0 is the permeability of free space, μ_r is the relative permeability of the core material, N is the number of windings, h is the height of the toroid, r_0 is the outer radius of the toroid, and r_i is the inner radius.

Manipulating this equation knowing the inductance from calculations using the reflectance data acquired through VNA, the relative permeability of the core material was derived. It is of interest to understand the influence of the presented fabrication technique on these calculated properties, recognizing trends to attribute changes in behavior to the material composition.

Chapter 5: Stabilization of Permalloy Nanoparticles for Syringe Printable Inductors

5.1 Introduction

Additive manufacturing opens the possibility of printing custom parts with complex shapes. Improving the technology to make it more consumer accessible will allow problem-solving to be approached from an unlimited source of perspectives. Advancements are being made to improve accuracy and resolution, as well as expand the materials that can be printed. It is of interest to create a single tool that prints multiple material filaments, simplifying and making less expensive the ability to fabricate prototypes and produce products. A common type of 3D printing is syringe printing, which is done using a filament that is liquid during extrusion but solidifies after deposition. Typically, this is accomplished using thermoplastic resin that when heated becomes molten and solidifies again after cooling. Recent efforts have been made to include metal or ceramic particles in these resins to further tailor the properties of the materials printed, such as including ceramic particles for improved dielectric properties, conductive particles for electrical properties, or magnetic particles for magnetic properties. Magnetic composite filaments are the least explored of the three mentioned and have the potential for being used for a wide array of applications, such as generators, transformers, magnetic recording devices, and inductors [76]–[78].

One of the greatest challenges of printing magnetic composites is accomplishing a high enough particle loading to produce a strong magnetic response for the additively manufactured part to be competitive with traditional magnet fabrication methods. Embedding magnetic particles into a polymer feedstock is the most studied approach to printing magnetic composites, using thermoset polymers typically used for fuse deposition method printing. Ferrite particles are a common additive, with Palmero *et al.* mixing MnAlC particles in polyethylene at a final particle loading of 72.3 wt% (31.5 vol%) [108]. Feedstocks containing permalloy ($Ni_{80}Fe_{20}$) particles in polyethylene were explored by Arboui *et al.* at a particle loading of 40 vol% [109]. In another study, permalloy nanoparticles were mixed into polydimethylsiloxane at 50 wt% and printed into an inductor using silver traces [67]. In all these ink formulations, magnetic content was limited by the high viscosity of the polymer binder.

This study investigates syringe printing of high magnetic nanoparticle content parts using permalloy ($Ni_{80}Fe_{20}$), a commonly used magnetic material for inductor applications due to its high permeability. Two different particle sizes of 250 nm and 30 nm are synthesized to observe the effect of particle size on stability. Previous studies by our group used polyelectrolyte poly(acrylic acid) (PAA) to stabilize ferrite materials. Here we investigate the applicability of similar coating procedures for permalloy. The use of silica as a coating was also explored as an intermediate layer between permalloy and polyelectrolytes in an attempt to stabilize the permalloy particles. Histidine has also been shown to have an affinity to nickel and its function as a stabilizer for permalloy is explored [110]. Zeta potential is measured to discern a change in surface charge after the various coating procedures. Settling behavior is documented to perceive the success of attempted coating procedures on particle stability in water. Permalloy nanoparticle inks are concentrated with polyethylene oxide to increase viscosity and glycerol to decrease evaporation rates while printing according to previous ink studies by our group. The roles of PEO and glycerol on the stability of permalloy are also examined. Finally, permalloy inks are printed into toroid shapes to exhibit their viability in fabricating three-dimensional magnetic structures as well as being manufactured into inductors whose electronic properties are dependent on using permalloy magnetic ink as the core.

5.2 Results and Discussion

5.2.1 Permalloy particle stability

To create a printable nanoparticle ink, the particles need to be stabilized in solution and irreversible, strong flocculation should be prevented. Samples were made into inks using polyethylene oxide (PEO, 30k MW) and glycerol to modify the viscosity and evaporation rate as previously studied.

Many coating procedures were studied, but the sample that printed the most uniformly was surprisingly the control, which had no surface modification before mixing with PEO and glycerol to make it into an ink. It was predicted that the two additives used in modifying the viscosity of the ink also had the role of stabilizing the permalloy particles. Performing a coating procedure in excess and washing off what doesn't adsorb, small permalloy was coated with PEO and glycerol and left to settle overnight. The results show that both coatings suspend the 30 nm permalloy and allow them to remain homogeneous in water after 24 hours – and even after three weeks (Figure 5.1

(a)). Zeta potential measurements (Figure 5.1 (b)) show that these neutrally charged polymers decrease the magnitude of the zeta potential of permalloy. This indicates that although they are coating permalloy, electrostatic repulsion is not responsible for its stability in solution. The suspension stability is instead likely due to steric hindrance.

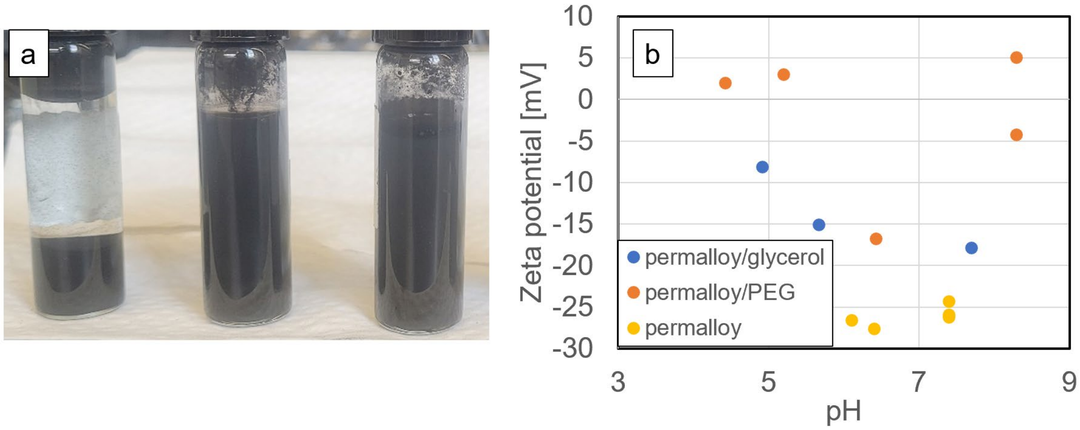

Figure 5.1: (a) settling behavior of 30 nm diameter permalloy uncoated, coated with PEO, and glycerol after sitting overnight, and (b) comparison of zeta potential of permalloy coated with glycerol and PEO.

5.2.2 Behavior of permalloy inks

The success criteria for an ink were continuous, homogeneous extrusion at pressures achievable by the syringe printer and shape retention with multiple layers. All coating attempts were made into ink and checked for print viability by performing a smear test. The only tested ink in this study that successfully extruded through the printer nozzle when pressure was applied and retained its shape after deposition was the small diameter permalloy with no initial surface modification before mixing with PEO and glycerol ink additives. To study the stability of permalloy with PEO and glycerol, particles were coated in excess and then washed to remove anything that did not adsorb.

For the ink, more polymer was in the solution than needed to coat and stabilize the particles. The excess polymer increases the viscosity and results in adequate shape retention of the printed part [94].

To exhibit the regularity of the inks, toroids were printed by depositing ink in three concentric rings and then moving up the nozzle and repeating the same path to add layers to the desired height. Observing the microscope images, the individual layers are distinct (Figure 5.2). The printed structures were placed in an oven to dry. The toroids were extremely fragile upon drying due to their high particle content and very low binder content. Thermogravimetric analysis (TGA) of these inks shows a water content of 33 wt% while printing, a glycerol content of 3 wt%, and a PEO content of 8 wt%. It seems that although this high magnetic particle content may have beneficial magnetic properties for the printed device, the mechanical properties suffer due to the lack of a polymer binder.

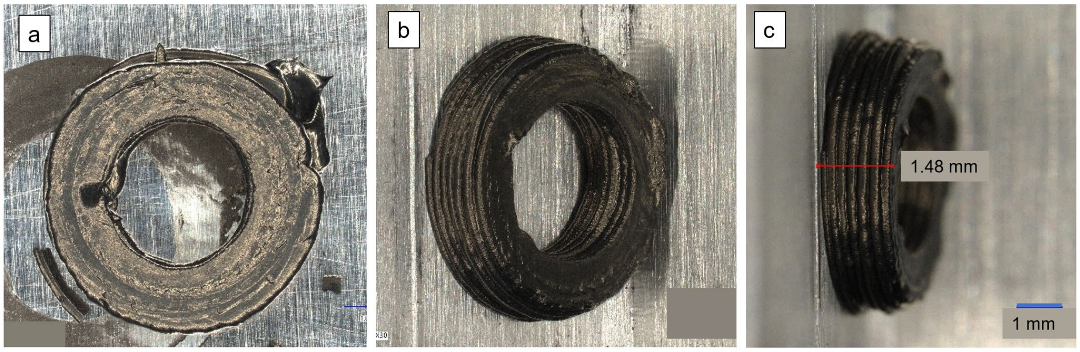

Figure 5.2: (a) top view (b) 45° (c) side views of printed permalloy toroids after drying. The toroid shape is regular, and the layers are distinct.

5.2.3 Printed inductor

Due to the fragility of the dried permalloy ink, a dielectric adhesive was applied using aerosol jet (AJ) printing to coat the magnetic ink and provide mechanical strength and protection as well as electrical insulation. The inductor shape was determined to compare to a permalloy ink with a lower particle content [67]. A silver nanoparticle ink (DOWA) was used with the AJ printer to make 10 conductive windings and a circuit path to make a connection to the VNA for reflectance parameter measurements (Figure 5.3 (a)). The silver ink was AJ printed with the bottom windings first and then the dielectric insulator. The substrate was then moved to the syringe printer to print the magnetic permalloy ink, and then moved again to the AJ printer to apply the final insulating layer and to complete the top conductive silver windings. The aqueous ink did not have a strong adhesion to the cured dielectric insulating polymer, and if left for too long the ink would dry, crack, and easily be blown away from the substrate. The printing process had to be quick to ensure that the magnetic material stayed intact for the final added layers applied with the AJ printer.

Only the small diameter permalloy was made into ink and printed into an inductor. The printed inductor experiences an initial resonance at 85 MHz, and below its resonance, it behaves as an inductor. At 30 MHz, the inductance is 180 nH. An inductor with the dielectric resin core instead of the magnetic material was constructed as a comparison. The polymer core material only has an inductance of 30 nH at 30 MHz, but a much higher resonant frequency at 850 MHz. The resonant frequency is inversely related to the inductance, so the higher inductance from the magnetic material results in a lower resonance.

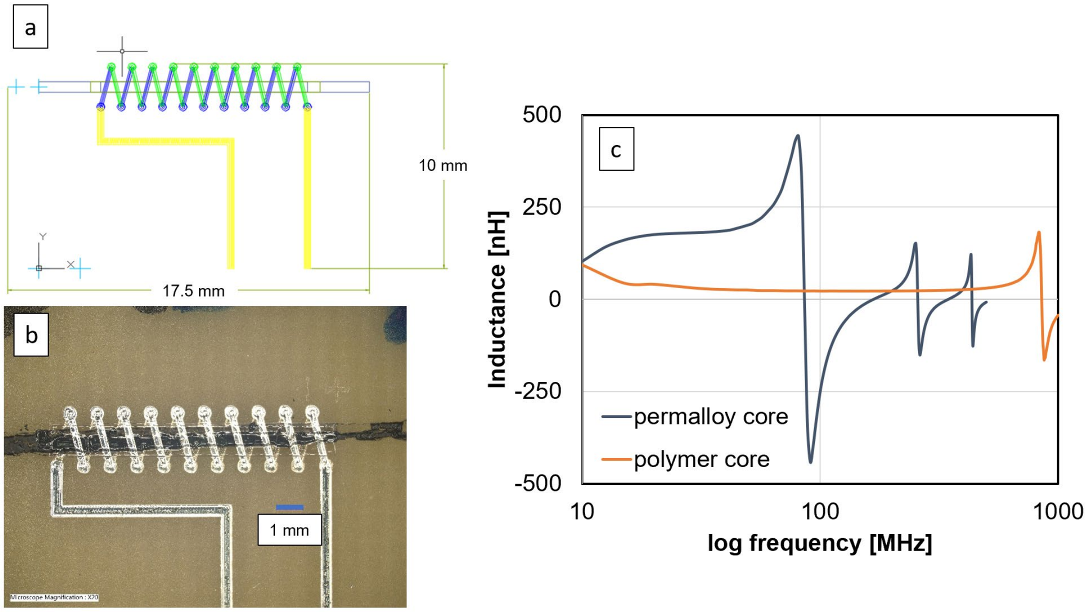

Figure 5.3: (a) The AJ printer tool path for making silver conductive windings and circuit traces, (b) printed inductor with permalloy ink as the magnetic core, and (c) inductance of syringe printed inductors with a polymer core and the permalloy ink core.

5.2.4 Small and large diameter permalloy

Permalloy was synthesized into two sizes, 30 nm, and 250 nm in diameter. VSM magnetic hysteresis measurements (Figure 5.4) show that the larger diameter nanoparticles (Figure 5.4 (b)) have a higher magnetic saturation of 0.59 T and a higher coercivity of 175 Oe than the small diameter permalloy (Figure 5.4 (a)) which has a magnetic saturation of 0.15 T and a coercivity of only 20 Oe. The relative permeability of small permalloy is $\mu_r = 5$ while the large permalloy has a permeability of $\mu_r = 9$. If an inductor could be made with the larger permalloy with higher permeability, the inductance would likely increase.

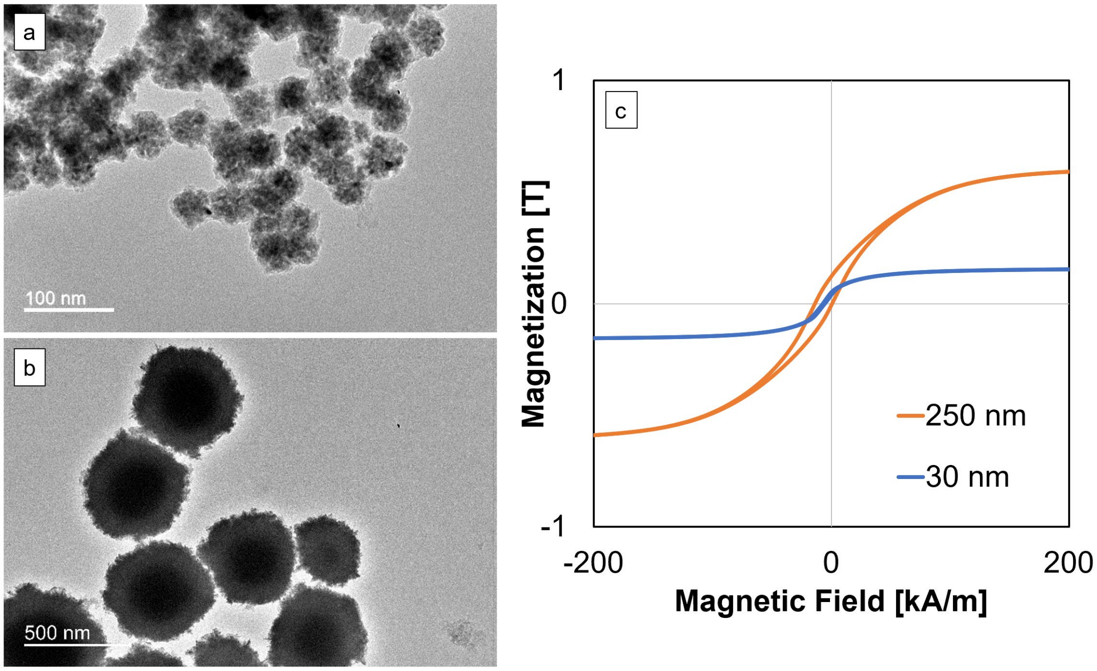

Figure 5.4: TEM of (a) 30 nm and (b) 250 nm diameter permalloy and (c) magnetic hysteresis of the two permalloy particle sizes

Particles of both sizes were coated in excess with poly(acrylic) acid, histidine, silica, and poly(styrene sulfonate), and settling behavior was observed over 24 hours (Figure 5.5). Of all the tested coating procedures, the ones that remained suspended even after 24 hours were the small permalloy particles. The vials that appeared unchanged in homogeneity of the suspended particles were those with small permalloy coated with silica and histidine. All of these coated samples, including the ones that did not remain stable during the settling experiment, were made into inks by mixing with poly(ethylene oxide) and glycerol in water and concentrating. The 30 nm diameter permalloy ink with no additional surface coating was extruded easily and had acceptable shape retention, so the inductor device was constructed with this formulation.

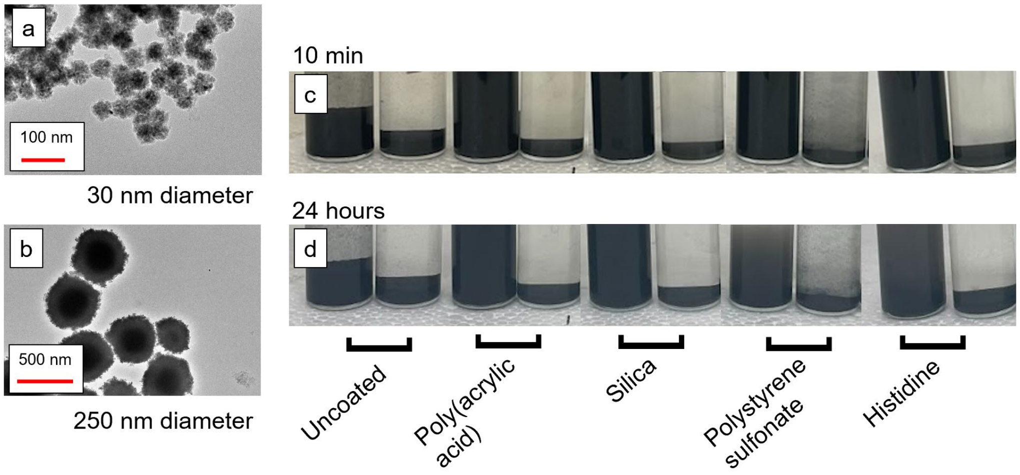

Figure 5.5: (a) TEM of 30 nm diameter permalloy and (b) 250 nm diameter permalloy used for settling experiments. Settling behavior of permalloy of the two different sizes (30 nm diameter on the left of the pairings and 250 nm diameter on the right) with various coatings (c) after 20 minutes and (d) after 24 hours.

5.2.6 Coating with poly(acrylic acid) (PAA)

Although a permalloy ink was successfully formulated with the 30 nm diameter permalloy particles with no additional coating aside from the polymers included in the ink formulation as viscosity enhancers, printing with large permalloy was still of interest. The remainder of the experiments in this study are on attempting to coat 250 nm diameter permalloy to stabilize and formulate into a shape retentive ink.

Syringe printing of colloidal inks has been demonstrated for ceramic systems using polyelectrolytes as a stabilizer [92]. The charge provided by adsorbed polyelectrolytes creates an electrostatic repulsion that isolates particles in an aqueous solution and prevents aggregate formation [95]. In this study, we explore the use of polyelectrolytes with varying charge groups in an attempt to coat and stabilize permalloy.

In a previous study, poly(acrylic acid) (PAA) ammonium salt successfully adsorbed to and stabilized iron oxide and doped ferrites for syringe printable nanoparticle inks. Using a procedure of coating in excess, it is ensured that the particles are interacting with the polymer dissolved in solution so that they would have the opportunity to adsorb. Zeta potential and settling studies were performed to observe the effect of the coating procedures on stabilizing permalloy nanoparticles. After mixing large permalloy with PAA in excess and washing away what does not adsorb, the particles settle in water within 10 minutes. The lack of change in surface charge of the permalloy after the coating procedures reveals that PAA does not adsorb to the permalloy with the zeta potential reading remaining the same at all tested pHs before and after coating. The Zeta potential of 250 nm diameter permalloy before and after interacting with PAA is the same. The particles settle in solution after 10 minutes.

5.2.7 Coating with silica

Syringe printable inks using silica or mixtures with silica have been reported in the literature [111], [112]. Coating permalloy with silica changes the surface properties of the permalloy without changing its crystal structure or magnetic properties. At a pH around 7, the zeta potential of permalloy with no coating (Figure 5.6 (a)) is measured to be around -35 mV. Silica particles (Figure 5.6 (b)) have a zeta potential of -42 mV. Permalloy coated with silica using citrate as an intermediate layer (Figure 56 (c)) has a zeta potential reading beyond -50 mV, which is more negative than the uncoated permalloy particles. We have demonstrated using zeta potential studies that the surface charge of the permalloy coated with silica alters the surface charge and acts more like that of silica and can therefore be further functionalized as if it were silica (Figure 5.6 (d)).

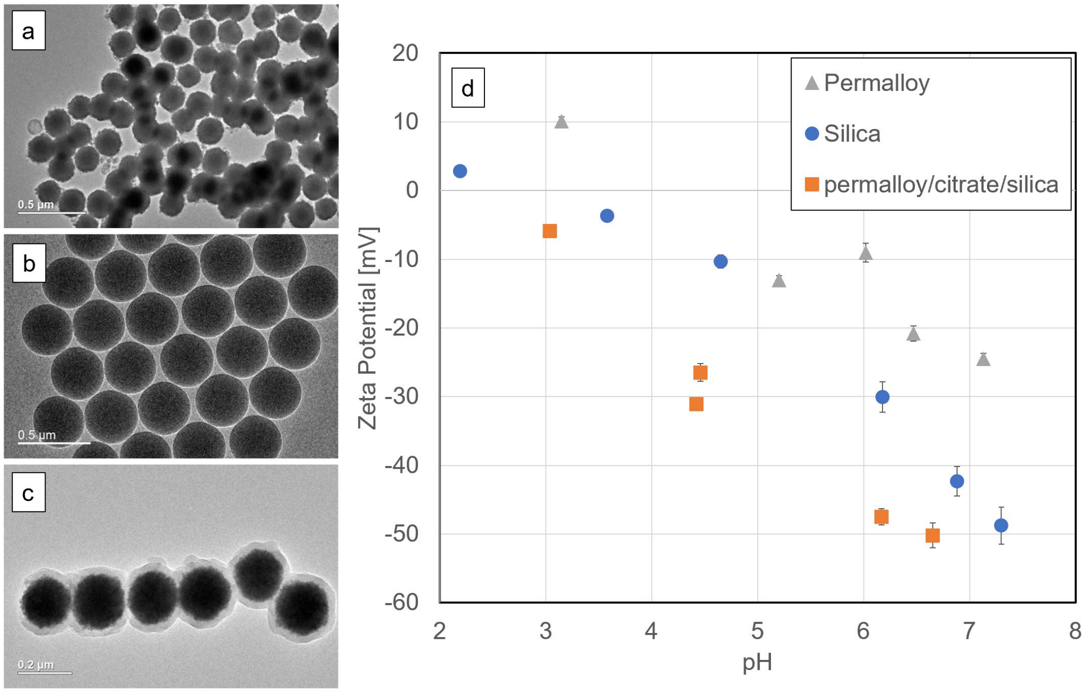

Figure 5.6: TEM images of (a) 250 nm diameter (b) silica particles, and (c) 250 nm diameter permalloy particles coated with citrate and then silica. (d) Comparison of zeta potential of the three particles.

Large permalloy particles coated with citrate/silica still settled in solution. According to the TEM picture of permalloy coated with silica, it is inconclusive whether particles are coated individually or in clusters. Citrate was used as an intermediate coating to see if it would help isolate the silica coating on the permalloy particles (Figure 5.7 (a)). Other attempts include using polypropylene glycol as an intermediate coating (Figure 5.7 (b)) because it is the polymer used to stabilize permalloy during its synthesis and a silica coating procedure in dilute solution (Figure 5.7 (c)) to mitigate permalloy agglomeration. Permalloy coated with citrate and then silica had a uniform silica layer with a 30 nm thickness, while particles coated with propylene glycol as an intermediate layer had a similar thickness but a more inconsistent morphology. The silica coating that has citrate as an intermediate layer but is coated in a more dilute solution has a thickness of only 10 nm and is also feathery. The DLS analysis of permalloy with these various coating attempts measures particle diameters much larger than what is observed visually with TEM (Table 5.1). The bare particles have a DLS-measured diameter over 10 times the TEM-measured diameter. The DLS measures agglomerations of the particles instead of their true particle diameter because they flocculate in water. Coating with silica reduces the DLS measured diameter compared to the uncoated permalloy, but they are still much larger than the individual particle diameter. These silica coating procedures cover clusters of permalloy.

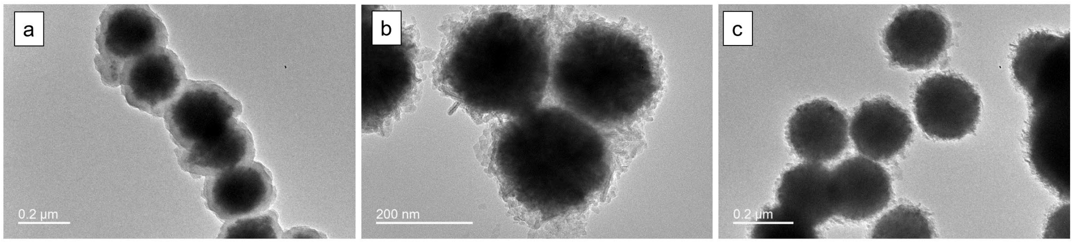

Figure 5.7: TEM images of permalloy with various methods of coating with silica (a) base layer citrate, (b) base layer propylene glycol, (c) dilute silica coating with intermediate citrate layer

Table 5.1: DLS particle size and description of the morphology of silica-coated 250 nm diameter permalloy

Sample	Average measured diameter (nm)	STD	Description of surface morphology
Uncoated permalloy	3200	400	-
(a) permalloy/citrate/silica	1600	20	Uniform, in clusters
(b) permalloy/PG/silica	1120	180	Non-uniform and clustered
(c) permalloy/citrate/silica dilute	2130	270	Thin and non-uniform

After determining that citrate was the best intermediate for coating with silica compared to the other tested methods because its DLS-measured diameter was the smallest, the silica was functionalized further. Silica itself is negatively charged at the surface at neutral pHs. Positive polyelectrolytes often do not have a strong charge when dissociated. Silica has been shown to be coated with an anionic polyelectrolyte by using a cationic polyelectrolyte as an intermediate layer [110]. The cationic polyelectrolyte used here was poly(allylamine hydrochloride) (PAH). Due to its positive charge when dissociated, it readily adsorbed to silica nanoparticles or permalloy coated with silica. Zeta potential measurements show an increase in surface charge after coating procedures with PAH due to the charge neutralization that occurs when PAH adsorbs to the negatively charged silica surface. This more positive surface charge is not enough to stabilize the particles in aqueous solution (Figure 5.8). The anionic polyelectrolyte used in this study was poly(styrene sulfonate) (PSS). Particles coated with PAH and then PSS showed a decrease in surface charge, which confirms the adsorption of the negatively charged polymer to the particle surface. The opposing charges promote the adsorption of the polymer to the surface, and then the surface charge exhibits that negative charge. Silica nanoparticles coated with the double layer also exhibit the same surface charge as the permalloy particles coated with double-layered silica. DLS measurements of particle diameters show that after all of these functionalization steps, the measured value is lowest at the final stage of coating (Table 5.2). Even still, with this multi-step coating procedure that successfully stabilizes silica in solution, large permalloy particle solutions did not remain homogeneously suspended in water. Even after 10 minutes, silica/PAH/PSS coated permalloy completely settled to the bottom of their vial.

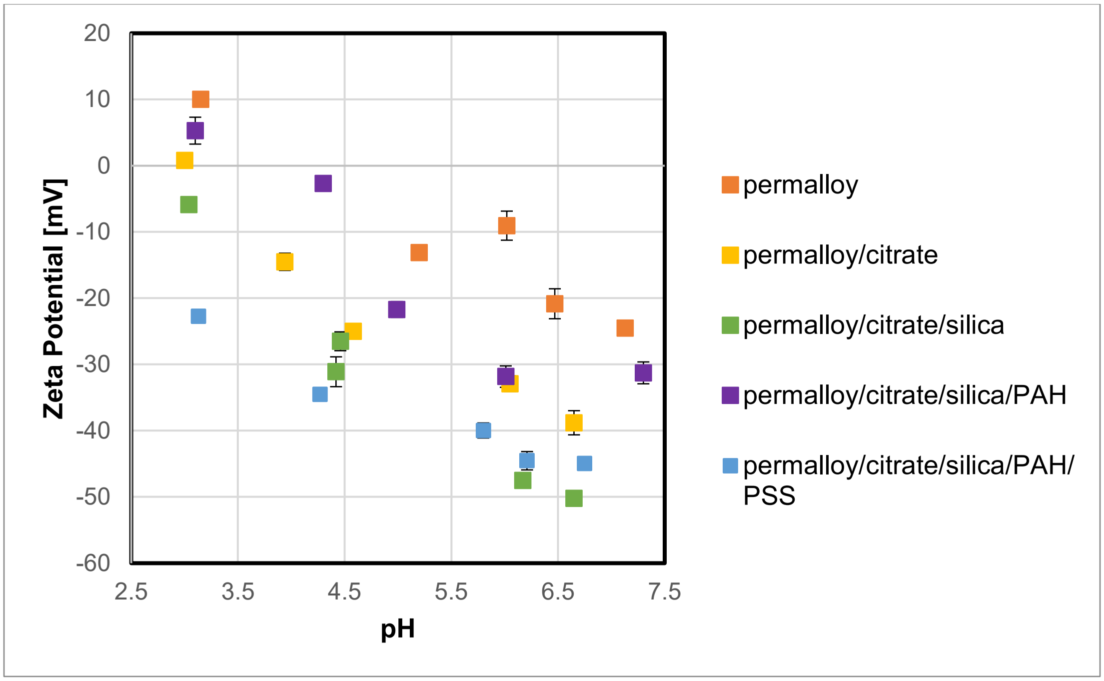

Figure 5.8: Zeta potential of 250 nm diameter permalloy uncoated, with citrate, then silica, then PAH, then PSS.

Table 5.2: DLS measured size and zeta potential between pH 6.5-7.5 of large diameter permalloy with each successive coating.

Sample	**Average measured diameter [nm]**	**STD**	**Zeta Potential between pH 6.5-7.5 [mV]**
Permalloy	3522	1115	-24.5
Permalloy/citrate	2846	836	-38.8
Permalloy/citrate/silica	2777	395	-50.2
Permalloy/citrate/silica/PAH	6571	1205	-31.3
Permalloy/citrate/silica/PAH/PSS	1637	134	-45.0

Even though the large permalloy particles showed a strong surface charge after some of the coating procedures, they were still settling in water. Inks were made with coated large permalloy, and they did not extrude, but instead phase separated and precipitated from solution. All of the solvent was pushed through the nozzle and appeared clear with no particles observed in the droplets. The clustered particles were clogged at the nozzle.

These silica coating studies were only performed on large diameter (250 nm) permalloy. Due to the successful functionalization of the polyelectrolytes to the silica on the permalloy surface, it is predicted that if small diameter (30 nm) particles are used or if the silica coating procedure was optimized further to coat isolated particles instead of clusters, particle stability is more likely. Other particle sizes between 30 nm and 250 nm diameters could be synthesized to explore the size limit of stability for these dense permalloy nanoparticles.

5.3 Conclusion

Permalloy nanoparticles with a 30 nm diameter were synthesized, stabilized, and concentrated into a syringe printable ink to be made into an inductor core and characterized as an inductor. A series of experiments were performed using various coating techniques to ultimately discover that the same polymer used to enhance viscosity also successfully stabilizes the particles in water. Two different particle sizes were studied, but the large diameter permalloy (250 nm) did not stay suspended in water due to its large size, even after many successful functionalization procedures. Zeta potential and TEM measurements confirmed the successful coating of silica and adsorption of PAH and PSS on the silica coating of large permalloy particles, but the electrostatic repulsion was not enough to keep the large, dense particles suspended. The smaller diameter permalloy (30 nm), however, remained homogeneous in water with histidine, silica, polyethylene oxide (PEO), and glycerol as a coating. The small permalloy ink was formulated with only PEO and glycerol. The particle loading while printing was 67 wt% and the final particle concentration of the printed part after drying was 83 wt% (37 vol%) with a total polymer content of 17 wt% (62 vol%). The permalloy ink was demonstrated to print consistently and exhibit shape retention that allowed multiple layers of ink to be deposited without sagging. Parts with multiple layers of ink did not crack as readily as single printed passes, but even thick (1.5-2 mm height) parts were very delicate once dried. Permalloy core inductors were fabricated by insulating the printed permalloy with an AJ-printed dielectric adhesive and silver conductive nanoparticle ink were printed as the windings and circuitry. A polymer core inductor was also fabricated to observe the enhancement in inductance with the inclusion of magnetic material. The inductance was measured to be 180 nH at 30 MHz, below its resonant frequency of 80 MHz, much higher than the inductance of the polymer core which is only 30 nH at the same frequency. This study showcases various stabilization methods for permalloy nanoparticles and a method for a syringe printable magnetic ink that can be used to construct three-dimensional electronic devices.

5.4 Experimental Procedures

5.4.1 Materials

Hydrous nickel chloride, hydrous ferrous chloride, sodium hydroxide, propylene glycol, potassium tetrachloroplatinate (K_2PtCl_4), citrate, tetraethylorthosilicate (TEOS), ammonium hydroxide (NH_3OH), acetone, ethanol, DI water, poly(acrylic acid) (PAA, Darvan), polyallylamine hydrochloride (PAH), polystyrene sulfonate (PSS), L-histidine, polyethylene oxide (PEO, 30k MW), glycerol, potassium nitrate, silver nanoparticle ink (DOWA), mercapto ester UV and thermally curable dielectric adhesive (NEA121, Nordland Prod)

5.4.2 Methods

Permalloy nanoparticles were synthesized using a procedure adapted from Qin *et al* [72]. The procedure was quadrupled to produce a higher yield at a time, from approximately 0.5 g per synthesis to about 2 g. Hydrous nickel chloride and hydrous ferrous chloride were mixed at a 1:1 molar ratio with 32 g sodium hydroxide in 400 mL of propylene glycol. The size of the particles can be reduced by adding the nucleating agent K_2PtCl_4 at varying concentrations. We used 16 mg of the nucleating agent to produce particles with a 30 nm diameter. Without the nucleating agent, the nanoparticles are 250 nm in diameter. The kinetics of the reduction reaction were adjusted so the final molar ratio of the crystallites was 4:1 nickel to iron ($Ni_{80}Fe_{20}$). The solution was mixed using a mechanical mixing arm at 1300 rpm. The synthesis solution was heated in an oil bath at 80°C for 2 hours to dissolve all the salts, and then raised to 180°C for 2 hours to allow the particles to grow. After cooling overnight, a cleaning solution of 1:1:1 acetone, ethanol, and DI water was added to the flask and placed in a sonicating bath to dilute and decrease the viscosity of the synthesis solution. A magnet was used to collect the particles and the supernatant was discarded. The cleaning solution was added, and the solution was sonicated at least five times, using the magnet to collect the particles and discard the supernatant. DI water or ethanol was then used an additional five times to wash the particles with the same sonicating and magnet collecting steps depending on the following coating procedure.

For the synthesis of silica nanoparticles, 6 mL of TEOS was added to 70 mL of ethanol and magnetically stirred. A solution was made of 1.5 mL ammonium hydroxide in 25 mL of water and then added to the ethanol and TEOS solution. The solution was mixed with a magnetic stir rod for two hours. The solution was transferred to centrifuge tubes and washed with DI water using the centrifuge to collect.

To coat permalloy with polyacrylic acid (PAA), 0.375 mL of 30% aqueous PAA solution (Darvan) was added to 40 mL of water. 3 g of permalloy was added and sonicated for 1.5 hours, shaking the vial in 15-minute intervals. The coated particles were washed with DI water five times.

To coat the permalloy with citrate, 0.5 g of wet permalloy was mixed into 40 mL of citrate solution (0.45 M) and mixed with a mechanical mixing arm for one hour. The particles were then separated from the solution using a magnet and the supernatant was discarded. Another 40 mL of the citrate solution was added to the particles and mixed for a total of three times.

To coat with propylene glycol (PG), 0.5 g of wet permalloy was mixed into a solution of 1 mL of PG in 20 mL of water and sonicated for one hour. The coated particles were washed with water.

To coat permalloy with silica, a magnet was used to collect the bare, citrate-coated, or propylene glycol-coated permalloy particles, and the supernatant was discarded. 0.5 g of the wet mass of permalloy was measured out, added to a solution of 100 mL of ethanol and 20 mL of water, and sonicated for 30 minutes to homogenize. TGA confirms an approximate 30 wt% fraction of solvent consistently in the wet mass. Varying amounts of TEOS were added (0.1, 0.5, 1 mL), and then 10 mL of a 10% aqueous ammonium hydroxide solution. The solution was either sonicated or mixed with a mechanical mixing arm for 1.5 hours, agitating the vial every 10 minutes to ensure even coating. Silica-coated particles were collected with a magnet and DI water was used to wash them, sonicating in between. Whenever the solution needed to be upscaled, everything was multiplied by the same factor. To achieve a coating of 2 g of wet permalloy instead of 0.5 g, all ingredients were multiplied by four.

Coating permalloy nanoparticles, silica nanoparticles, or silica-coated permalloy nanoparticles with poly(allylamine hydrochloride) (PAH) or poly(styrene sulfonate) (PSS) was done using an adapted procedure from Feng et al [113]. 40 mg of PAH or PSS was added to 20 mL of KNO_3 solution (0.5 M). Then, nanoparticles were added to make a solution of 2% particles in water and stirred vigorously with a mixing arm for two hours. The coated particles were then washed with water. Whenever needed to coat in larger quantities, all ingredients were multiplied by the same scale factor.

To coat with L-histidine, 2 g of permalloy (from a wet pellet) was added to 6 mL of DI water with 0.014 mL of L-histidine (Sigma) dissolved in water (1 mg / 200 mL water), adapted from a published procedure[110]. Washed permalloy particles were never completely dried to prevent irreversible aggregation. Therefore, a centrifuge was used to form a wet pellet of the particles and the excess DI water was discarded. About 30 mg of wet permalloy was sacrificed to determine the water content of the pellet using thermogravimetric analysis (TGA). For the 20 nm permalloy nanoparticles, the water content of the pellet was approximately 35-40 wt%. This value was used to weigh out 2 g of permalloy, or around ~2.5 g of wet permalloy depending on the water content. 2 g of permalloy was added to a solution of DI water with 1 mL of L-histidine solution and sonicated for two hours. The excess polymer was removed by using DI water to clean, using the same sonicating-magnetizing cleaning procedure.

To coat with poly(ethylene oxide) or glycerol, a wet pellet containing 0.5 g of permalloy was added to 5 mL of PEO (70 mg / mL) or glycerol (1 mL / 10 mL) aqueous solutions, sonicated for an hour, and left overnight. The particles were then washed with DI water five times.

Thermogravimetric analysis (TGA) was used to determine the water content of centrifuged pellet of permalloy. To formulate permalloy ink, 3 g of coated or uncoated permalloy particles were measured out of the wet, centrifuged permalloy pellet and were suspended in 31 mL of DI water. 5 mL of polymer solution of polyethylene oxide (30,000 g/mol MW) (70 mg / mL) was added, as well as 4 mL of glycerol for a total solution of 40 mL. The solution was sonicated for an hour and left to stand overnight. The solution was then centrifuged to form a pellet of the ink and the supernatant was reserved. The TGA was used to quantify the water content of the pellet, and the reserved supernatant was added to adjust the water content if necessary. If more or less ink needed to be made, everything was scaled by the same factor.

Permalloy inductor cores were printed by loading a centrifuged pellet of permalloy ink into 3 cc syringe barrels and printed using a 5-axis mill (HAAS^{TM}) that was modified to perform additive manufacturing by integrating a syringe print head into the system. A 22 G nozzle was used for a minimum line width of 0.4 mm and inks were extruded using compressed air at a pressure between 20-50 psi depending on the viscosity of the ink.

To construct a complete device, conductive windings were printed using an aerosol jet (AJ) printer for the thin, flat silver traces and insulation while the syringe printer was used for the three-dimensional magnetic structure. On a heat-resistant substrate (FR4), a single flat layer of dielectric adhesive was applied (NEA121) using the AJ printer with UV light attachment to cure in situ. Then the silver layer was applied (DOWA) using an AJ printer with traces 15 μm thick and oven sintered at 150°C. Another layer of dielectric adhesive was printed and cured. The substrate was then transferred to the syringe printer for the deposition of the magnetic permalloy ink in a single or two consecutive 10 mm lines. The substrate was transferred again to the AJ printer so that another dielectric adhesive layer can be deposited. Seams were also printed to ensure that the final layer of silver would not be printed over a sharp edge which would cause cracking and prevent current flow.

5.4.3 Characterization

5.4.3.1 Transmission Electron Microscopy (TEM)

Transmission Electron Microscopy (JEOL-2100F field emission) has a point-to-point resolution of 0.19 nm and was used to evaluate the regularity of permalloy particle shape and to observe polymer coating on the surface. Dilute suspensions of permalloy in ethanol were deposited on copper sample holders with a carbon grid. The purpose of this characterization was to evaluate the shape and size of the particles only, without any polymer viscosity modifier.

5.4.3.2 Zeta potential

A Zetasizer (Malvern^{TM}) was used to measure the zeta potential of pure particles before and after coating with various polymers. Particles were suspended in KNO_3 solution (10 mM) just until there was a notable color change in the solution but still transparent. The pH was adjusted by adding nitric acid dropwise (0.01 M). Measurements were made in triplicate in the pH range of 3-8.

5.4.3.3 Dynamic light scattering (DLS)

DLS (Malvern^{TM}) was used to measure particle or aggregate size after various coating procedures. Samples are prepared by adding droplets of the washed solution to 3 mL of DI water that had been filtered through a 0.45 μm filter until the solution is slightly turbid. The solution was passed through a 1 μm filter into the sample container for analysis.

5.4.3.4 Settling behavior

A 2% aqueous solution of coated or uncoated particles was sonicated for 30 minutes and then left untouched for 24 hours. Pictures were taken periodically to observe changes in turbidity over time.

5.4.3.5 Thermogravimetric analysis (TGA)

Permalloy ink composition and solvent concentration were analyzed using TGA (Shimadzu TGA-50). A 30-100 mg pellet of wet ink was heated to 400°C at 10°C / min.

5.4.3.6 Magnetic properties

Magnetic properties were measured using a Vibrating Sample Magnetometer (VSM, Hitachi, Japan). Permalloy powder was dried in a desiccator under vacuum for measurement. A magnetic field was cycled between -4 kG and 4 kG. From VSM, magnetic saturation, coercivity, and hysteresis loss, and direct current (DC) permeability were observed.

5.4.3.7 Inductance properties

A vector network analyzer (VNA, Agilent) that sweeps between 1 MHz and 10 GHz was used to measure reflectance (S_{11}) at high frequencies. From this measurement, complex impedance and therefore total resistance and inductance were calculated and the resonant frequency was observed.

Chapter 6: Perspectives and Future Work

The major takeaways from the presented work are:

- Particle loading increases inductance.
- High viscosity resin limits magnetic particle loading.
- Iron oxide and doped ferrite inks are translatable.
- Particle size influences the efficiency of polymer coating for stability.
- Steric stabilization of nanoparticles is effective in making a syringe printable ink.
- High particle-loaded magnetic inductor cores are brittle without sintering.

In Chapter 3, magnetic particles were mixed in resin to create toroid structures and measure inductance. A general trend was observed that increasing particle loading increases inductance while decreasing operating temperature. The particle loading was limited by the viscosity of the matrix resin. From the work shown in this chapter, it was interesting to make inks from scratch instead of using proprietary resins to investigate further how to control ink viscosity and particle stability for an optimized print, which is explored in the following chapters.

In Chapter 4, nanoparticle inks were fabricated using iron oxide as a model and MnZn ferrite as an example of the ink composition being translated to other ferrite materials.

Both iron oxide and MnZn doped ferrite particles were stabilized as particle stability is an essential requirement to produce printable ink. The effect the molecular weight of the free polymer poly(ethylene oxide) (PEO) has on ink flow was observed and an optimal molecular weight was determined. Shape retention and recoverability of ink as a function of particle loading was explored, with too little resulting in a messy print and too much being impossible to extrude. The optimal amount for the iron oxide ink system during extrusion was 41 vol%. Premature evaporation of solvent was resolved using a solvent blend of water with glycerol, which has a higher evaporation rate, and the optimal concentration of 10% glycerol in water was determined. MnZn doped ferrite inks were printed into toroids and sintered to increase relative magnetic permeability from $\mu_r = 1$ to $\mu_r = 85+$ for enhanced device performance compared to unsintered toroids and undoped iron oxide inks. The sintered MnZn ferrite toroids were constructed into inductors and their inductance and device efficiency were measured and compared to a toroid with a polymer core and no magnetic properties. This chapter laid out a template for ferrite inks with the potential to be fabricated into useful passive electronic devices.

In Chapter 5, permalloy nanoparticles were synthesized, stabilized, and concentrated into a syringe printable ink to be made into and characterized as an inductor. Of the two particle sizes studied, the 250 nm diameter permalloy did not stay suspended in water due to its large size, even after many successful functionalization procedures. Zeta potential and TEM measurements confirmed successful coating of silica and adsorption of PAH and PSS on the silica coating of large permalloy particles, but the electrostatic repulsion was not enough to keep the large, dense particles suspended. The particle loading while printing was 67 wt% and the final particle concentration of the printed part after drying was 83 wt% (37 vol%) with a total polymer content of 17 wt% (62 vol%). The permalloy ink was demonstrated to print consistently and exhibit shape retention that allowed multiple layers of ink to be deposited without sagging. Parts with multiple layers of ink did not crack as readily as single printed passes, but even thick (1.5-2 mm height) parts were very delicate once dried. Permalloy core inductors were fabricated and an inductance of 180 nH was measured at 30 MHz, below its resonant frequency of 80 MHz, much higher than the inductance of the polymer core comparison which is only 30 nH at the same frequency. This study showcases various stabilization methods for permalloy nanoparticles and a method for a syringe printable magnetic ink that can be used to construct three-dimensional electronic devices.

The mechanical robustness of the printed device was a major hurdle. Even if the print rheology was well optimized, the final product often was brittle and difficult to handle without breaking. In Chapter 4, sintering was used to densify the printed MnZn doped ferrite part to improve mechanical robustness and magnetic permeability. In Chapter 5, the permalloy ink was insulated using an adhesive to prevent the brittle structure from breaking and falling off the substrate. Post-processing by sintering or coating complexes the process and still requires external tooling or expensive specialized equipment.

Laser-assisted direct ink writing seems to be a promising technique for metallic nanoparticle printing, which uses a focused laser to rapidly heat and melt particles together in situ and has been demonstrated by Skylar-Scott et al., printing free-standing silver nanoparticle structures with high mechanical properties and conductivity. This would eliminate post-processing sintering steps and reduce opportunities for cracking [114]. Laser sintering in situ with a DIW printer has been shown to pattern conductive metallic interconnects and free-standing spiral structures on both flexible and rigid substrates [114]. It has also been used to print single spherical gold nanoparticles with a precision of 50 nm [115], as well as silicon nanoparticles for dielectric and optical materials [116]. These lasers are attached to syringe printing systems and the printed part then does not require transfer to another manufacturing stage. The advantages of powder bed fusion are in this technology without the excess material and waste.

Another challenge faced was inconsistencies in particle behavior across purchased or synthesized batches that caused re-optimizing of ink compositions. The rheological window that allows printing or shape retention is narrow enough that even insufficient washing of synthesized particles could cause a change in a final ink formula suitable as an ink. Throughout the ink formulation steps, there should be quality control to ensure that particle surfaces are clean and consistent in behavior between batches.

The HAAS printer used throughout the studies presented in this thesis has pressurized air-controlled extrusion mechanics. The built-up air pressure in the syringe would lead to continued deposition even after the command was sent to stop extruding. This resulted in unintended features in the final printed part. More work can be done to optimize the print code to stop extrusion at a set time before finishing the tool path. This would likely change depending on the viscosity of the ink being printed.

Throughout this study, water was used as a solvent so that the polyelectrolyte coatings (if used) could be used as stabilizers to conform to the literature on ceramic nanoparticle ink systems and to avoid using harsh, synthetic solvents. The current trends in the additive manufacturing industry do not consider carbon footprint. My suggestion is not to use a system that better assimilates to current technologies in the printed electronics industry, but for the electronics industry to contemplate the end-of-life cycle of the materials, solvents, and processes they use and reconsider more sustainable alternatives. Additive manufacturing has the potential to produce on demand. Will commercial users consider the waste produced? It's up to the developers to make the technology less harmful in the long term.

Appendix

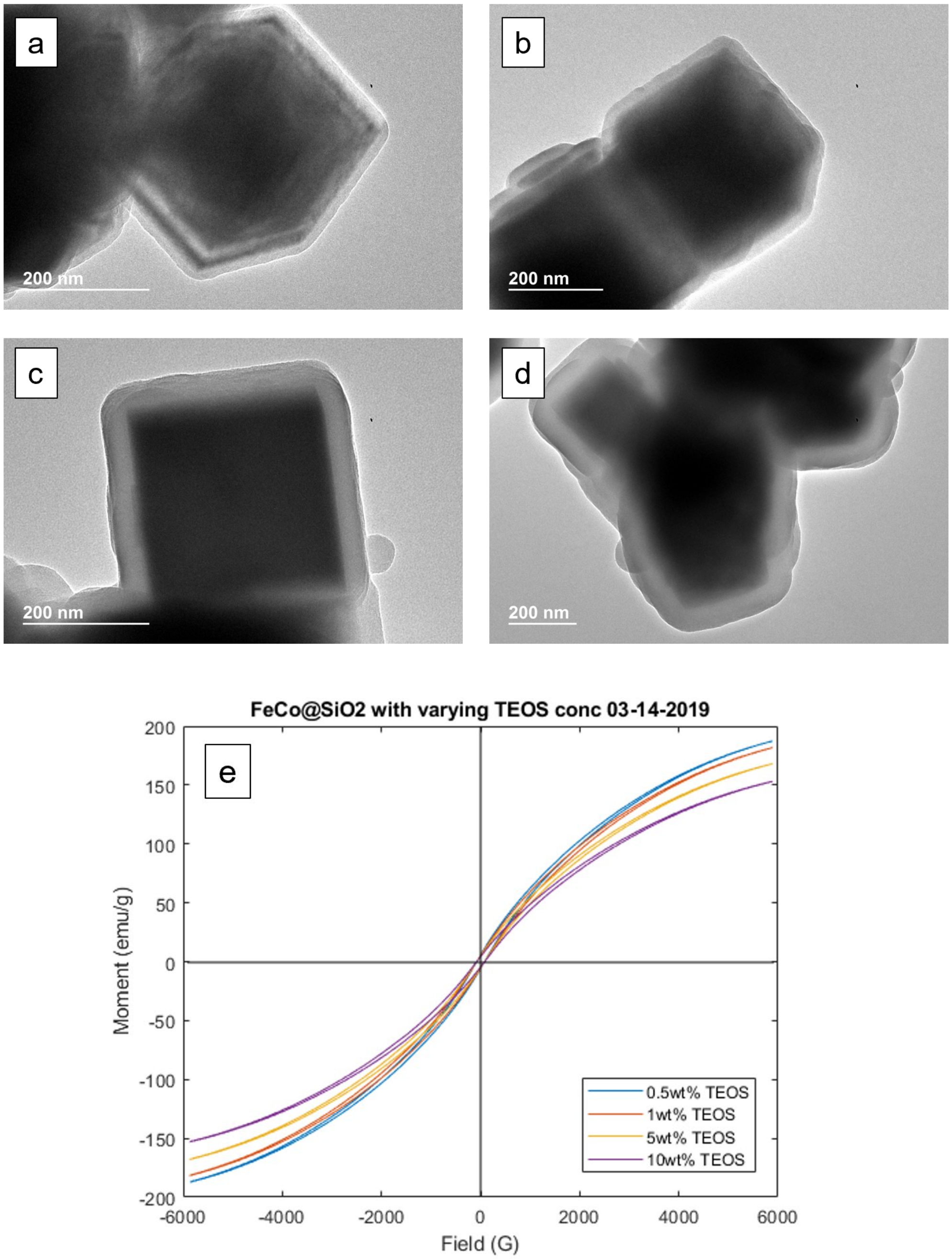

Figure A1: TEM images of FeCo cubic nanoparticles with a silica shell made with (a) 0.5 wt% TEOS (10 nm silica shell) (b) 1wt% TEOS (20 nm silica shell) (c) 5 wt% TEOS (35 nm silica shell) and (d) 10 wt% TEOS (60 nm silica shell thickness). (e) VSM of FeCo with varying silica shell thicknesses shows a slight decrease in magnetic saturation but no effect on coercivity.

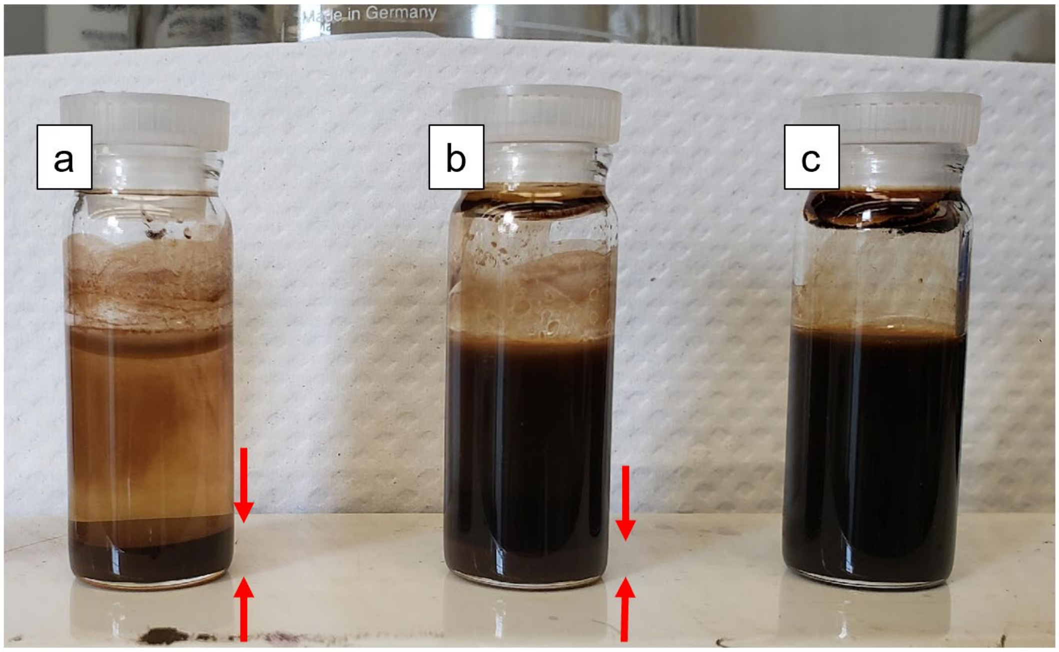

Figure A2: Iron oxide in water with (a) 0.4 wt% poly(acrylic acid):iron oxide, (b) 0.2 wt%, and (c) 0.1 wt%. Decreasing the amount of stabilizing polymer increases the homogeneity of particles in solution indicating an optimal concentration required for particle stability in water. Adding polymer beyond that concentration causes particles to settle.

Bibliography

[1] L. Li *et al.*, “Big Area Additive Manufacturing of High Performance Bonded NdFeB Magnets,” *Sci. Rep.*, vol. 6, no. 1, pp. 1–7, Oct. 2016, doi: 10.1038/srep36212.

[2] J. W. Sutherland, D. P. Adler, K. R. Haapala, and V. Kumar, “A comparison of manufacturing and remanufacturing energy intensities with application to diesel engine production,” *CIRP Ann.*, vol. 57, no. 1, pp. 5–8, Jan. 2008, doi: 10.1016/j.cirp.2008.03.004.

[3] W. Zhao, Y. Yan, X. Chen, and T. Wang, “Combining printing and nanoparticle assembly: Methodology and application of nanoparticle patterning,” *The Innovation*, vol. 3, no. 4, p. 100253, Apr. 2022, doi: 10.1016/j.xinn.2022.100253.

[4] M. a. S. R. Saadi *et al.*, “Direct Ink Writing: A 3D Printing Technology for Diverse Materials,” *Adv. Mater.*, vol. 34, no. 28, p. 2108855, 2022, doi: 10.1002/adma.202108855.

[5] E. B. Joyee, L. Lu, and Y. Pan, “Analysis of mechanical behavior of 3D printed heterogeneous particle-polymer composites,” *Compos. Part B Eng.*, vol. 173, p. 106840, Sep. 2019, doi: 10.1016/j.compositesb.2019.05.051.

[6] B. Derby and N. Reis, “Inkjet Printing of Highly Loaded Particulate Suspensions,” *MRS Bull.*, vol. 28, no. 11, pp. 815–818, Nov. 2003, doi: 10.1557/mrs2003.230.

[7] J. Cesarano, “A Review of Robocasting Technology,” *MRS Online Proc. Libr. Arch.*, vol. 542, ed 1998, doi: 10.1557/PROC-542-133.

[8] B. Y. Ahn *et al.*, “Omnidirectional Printing of Flexible, Stretchable, and Spanning Silver Microelectrodes,” *Science*, vol. 323, no. 5921, pp. 1590–1593, Mar. 2009, doi: 10.1126/science.1168375.

[9] S. S. Hossain, B. Gao, S. Park, and C.-J. Bae, “Incorporating Nanoparticles in Alumina Ink for Improved Solid-Loading and Sinterability of Extrusion-Based 3D Printing,” *ACS Appl. Nano Mater.*, vol. 5, no. 12, pp. 17828–17838, Dec. 2022, doi: 10.1021/acsanm.2c03792.

[10] Y. Hirata, “Theoretical aspects of colloidal processing,” *Ceram. Int.*, vol. 23, no. 1, pp. 93–98, Jan. 1997, doi: 10.1016/0272-8842(95)00144-1.

[11] M. Guvendiren, H. D. Lu, and J. A. Burdick, “Shear-thinning hydrogels for biomedical applications,” *Soft Matter*, vol. 8, no. 2, pp. 260–272, Dec. 2011, doi: 10.1039/C1SM06513K.

[12] J. A. Lewis, “Direct-write assembly of ceramics from colloidal inks,” *Curr. Opin. Solid State Mater. Sci.*, vol. 6, no. 3, pp. 245–250, Jun. 2002, doi: 10.1016/S1359-0286(02)00031-1.

[13] K. Sun, T.-S. Wei, B. Y. Ahn, J. Y. Seo, S. J. Dillon, and J. A. Lewis, “3D Printing of Interdigitated Li-Ion Microbattery Architectures,” *Adv. Mater.*, vol. 25, no. 33, pp. 4539–4543, 2013, doi: 10.1002/adma.201301036.

[14] S. Ghosh, S. T. Parker, X. Wang, D. L. Kaplan, and J. A. Lewis, “Direct-Write Assembly of Microperiodic Silk Fibroin Scaffolds for Tissue Engineering Applications,” *Adv. Funct. Mater.*, vol. 18, no. 13, pp. 1883–1889, Jul. 2008, doi: 10.1002/adfm.200800040.

[15] J. N. Stuecker, J. Cesarano, and D. A. Hirschfeld, “Control of the viscous behavior of highly concentrated mullite suspensions for robocasting,” *J. Mater. Process. Technol.*, vol. 142, no. 2, pp. 318–325, Nov. 2003, doi: 10.1016/S0924-0136(03)00586-7.

[16] J. Cesarano and I. A. Aksay, “Processing of Highly Concentrated Aqueous α-Alumina Suspensions Stabilized with Polyelectrolytes,” *J. Am. Ceram. Soc.*, vol. 71, no. 12, pp. 1062–1067, 1988, doi: 10.1111/j.1151-2916.1988.tb05792.x.

[17] J. Cesarano, I. A. Aksay, and A. Bleier, “Stability of Aqueous α-Al2O3 Suspensions with Poly(methacrylic acid) Polyelectrolyte,” *J. Am. Ceram. Soc.*, vol. 71, no. 4, pp. 250–255, 1988, doi: https://doi.org/10.1111/j.1151-2916.1988.tb05855.x.

[18] J. A. Lewis, “Colloidal Processing of Ceramics,” *J. Am. Ceram. Soc.*, vol. 83, no. 10, pp. 2341–2359, 2000, doi: https://doi.org/10.1111/j.1151-2916.2000.tb01560.x.

[19] S. Asakura and F. Oosawa, “On Interaction between Two Bodies Immersed in a Solution of Macromolecules,” *J. Chem. Phys.*, vol. 22, no. 7, pp. 1255–1256, Jul. 1954, doi: 10.1063/1.1740347.

[20] T. Patton, *Paint Flow and Pigment Dispersion*, Second. John Wiley & Sons, Inc., 1979.

[21] T. F. Tadros, “Control of stability/flocculation and rheology of concentrated suspensions,” *Pure Appl. Chem.*, vol. 64, no. 11, pp. 1715–1720, Jan. 1992, doi: 10.1351/pac199264111715.

[22] “Adsorption Effects on the Rheological Properties of Aqueous Alumina Suspensions with Polyelectrolyte - Guo - 1998 - Journal of the American Ceramic Society - Wiley Online Library.” https://ceramics.onlinelibrary.wiley.com/doi/abs/10.1111/j.1151-2916.1998.tb02373.x (accessed Jan. 06, 2021).

[23] M. Acosta, V. L. Wiesner, C. J. Martinez, R. W. Trice, and J. P. Youngblood, “Effect of Polyvinylpyrrolidone Additions on the Rheology of Aqueous, Highly Loaded Alumina Suspensions,” *J. Am. Ceram. Soc.*, vol. 96, no. 5, pp. 1372–1382, 2013, doi: 10.1111/jace.12277.

[24] L. Rueschhoff, W. Costakis, M. Michie, J. Youngblood, and R. Trice, “Additive Manufacturing of Dense Ceramic Parts via Direct Ink Writing of Aqueous Alumina Suspensions,” *Int. J. Appl. Ceram. Technol.*, vol. 13, no. 5, pp. 821–830, 2016, doi: 10.1111/ijac.12557.

[25] A. L. O. and and J. A. Lewis*, “Effect of Nonadsorbed Polymer on the Stability of Weakly Flocculated Suspensions,” Jul. 10, 1996. https://pubs.acs.org/doi/pdf/10.1021/la950953o (accessed Jan. 06, 2021).

[26] V. L. Wiesner, J. P. Youngblood, and R. W. Trice, “Room-temperature injection molding of aqueous alumina-polyvinylpyrrolidone suspensions,” *J. Eur. Ceram. Soc.*, vol. 34, no. 2, pp. 453–463, Feb. 2014, doi: 10.1016/j.jeurceramsoc.2013.08.017.

[27] P. Scherz and S. Monk, *Practical Electronics for Inventors, Fourth Edition*. 2016. Accessed: May 14, 2023. [Online]. Available:

https://www.mheducation.com/highered/product/practical-electronics-inventors-fourth-edition-scherz-monk/9781259587542.html

[28] J. C. Maxwell and W. D. Nivin, *The scientific papers of James Clerk Maxwell*. New York, Dover Publications, 1890. Accessed: Mar. 19, 2020. [Online]. Available: http://archive.org/details/scientificpapers01maxw

[29] J. N. Calata, G.-Q. Lu, and K. Ngo, "Soft Magnetic Alloy–Polymer Composite for High-Frequency Power Electronics Application," *J. Electron. Mater.*, vol. 43, no. 1, pp. 126–131, Jan. 2014, doi: 10.1007/s11664-013-2866-7.

[30] Z. Hashin and S. Shtrikman, "A Variational Approach to the Theory of the Effective Magnetic Permeability of Multiphase Materials," *J. Appl. Phys.*, vol. 33, no. 10, pp. 3125–3131, Jun. 2004, doi: 10.1063/1.1728579.

[31] S.-Y. Wu, C. Yang, W. Hsu, and L. Lin, "3D-printed microelectronics for integrated circuitry and passive wireless sensors," *Microsyst. Nanoeng.*, vol. 1, no. 1, Art. no. 1, Jul. 2015, doi: 10.1038/micronano.2015.13.

[32] N. Lazarus, S. S. Bedair, and G. L. Smith, "Creating 3D printed magnetic devices with ferrofluids and liquid metals," *Addit. Manuf.*, vol. 26, pp. 15–21, Mar. 2019, doi: 10.1016/j.addma.2018.12.012.

[33] L. H. Dixon, *Magnetics Design Handbook*. Unitrode Products from Texas Instruments, 2001.

[34] C. Brunetti and R. W. Curtis, "Printed-Circuit Techniques," *Proc. IRE*, vol. 36, no. 1, pp. 121–161, Jan. 1948, doi: 10.1109/JRPROC.1948.231246.

[35] J. Perelaer *et al.*, "Printed electronics: the challenges involved in printing devices, interconnects, and contacts based on inorganic materials," *J. Mater. Chem.*, vol. 20, no. 39, pp. 8446–8453, 2010, doi: 10.1039/C0JM00264J.

[36] M. C. Dang, T. M. D. Dang, and E. Fribourg-Blanc, "Silver nanoparticles ink synthesis for conductive patterns fabrication using inkjet printing technology*," *Adv. Nat. Sci. Nanosci. Nanotechnol.*, vol. 6, no. 1, p. 015003, Dec. 2014, doi: 10.1088/2043-6262/6/1/015003.

[37] M. G. Mohammed and R. Kramer, "All-Printed Flexible and Stretchable Electronics," *Adv. Mater.*, vol. 29, no. 19, p. 1604965, 2017, doi: 10.1002/adma.201604965.

[38] Z. Hou, H. Lu, Y. Li, L. Yang, and Y. Gao, "Direct Ink Writing of Materials for Electronics-Related Applications: A Mini Review," *Front. Mater.*, vol. 8, 2021, Accessed: May 14, 2023. [Online]. Available: https://www.frontiersin.org/articles/10.3389/fmats.2021.647229

[39] S. D. Lacey *et al.*, "Extrusion-Based 3D Printing of Hierarchically Porous Advanced Battery Electrodes," *Adv. Mater.*, vol. 30, no. 12, p. 1705651, 2018, doi: 10.1002/adma.201705651.

[40] E. Quain *et al.*, "Direct Writing of Additive-Free MXene-in-Water Ink for Electronics and Energy Storage," *Adv. Mater. Technol.*, vol. 4, no. 1, p. 1800256, 2019, doi: 10.1002/admt.201800256.

[41] Y. Chen *et al.*, "Direct Ink Writing of Flexible Electronics on Paper Substrate with Graphene/Polypyrrole/Carbon Black Ink," *J. Electron. Mater.*, vol. 48, no. 5, pp. 3157–3168, May 2019, doi: 10.1007/s11664-019-07085-x.

[42] G. Shi *et al.*, "A versatile PDMS submicrobead/graphene oxide nanocomposite ink for the direct ink writing of wearable micron-scale tactile sensors," *Appl.*

Mater. Today, vol. 16, pp. 482–492, Sep. 2019, doi: 10.1016/j.apmt.2019.06.016.

[43] Y. L. Kong *et al.*, “3D Printed Quantum Dot Light-Emitting Diodes,” *Nano Lett.*, vol. 14, no. 12, pp. 7017–7023, Dec. 2014, doi: 10.1021/nl5033292.

[44] P. Kamby, A. Knott, and M. A. E. Andersen, “Printed circuit board integrated toroidal radio frequency inductors,” in *IECON 2012 - 38th Annual Conference on IEEE Industrial Electronics Society*, Oct. 2012, pp. 680–684. doi: 10.1109/IECON.2012.6388746.

[45] G. McKerricher, J. G. Perez, and A. Shamim, “Fully Inkjet Printed RF Inductors and Capacitors Using Polymer Dielectric and Silver Conductive Ink With Through Vias,” *IEEE Trans. Electron Devices*, vol. 62, no. 3, pp. 1002–1009, Mar. 2015, doi: 10.1109/TED.2015.2396004.

[46] V. Subramanian *et al.*, “Progress Toward Development of All-Printed RFID Tags: Materials, Processes, and Devices,” *Proc. IEEE*, vol. 93, no. 7, pp. 1330–1338, Jul. 2005, doi: 10.1109/JPROC.2005.850305.

[47] S. Raju, R. Wu, M. Chan, and C. P. Yue, “Modeling of Mutual Coupling Between Planar Inductors in Wireless Power Applications,” *IEEE Trans. Power Electron.*, vol. 29, no. 1, pp. 481–490, Jan. 2014, doi: 10.1109/TPEL.2013.2253334.

[48] Y. Gu, D. Park, D. Bowen, S. Das, and D. R. Hines, “Direct-Write Printed, Solid-Core Solenoid Inductors with Commercially Relevant Inductances,” *Adv. Mater. Technol.*, vol. 4, no. 1, p. 1800312, 2019, doi: 10.1002/admt.201800312.

[49] N. Zhou, C. Liu, J. A. Lewis, and D. Ham, “Gigahertz Electromagnetic Structures via Direct Ink Writing for Radio-Frequency Oscillator and Transmitter Applications,” *Adv. Mater.*, vol. 29, no. 15, p. 1605198, Apr. 2017, doi: 10.1002/adma.201605198.

[50] M. L. F. Bellaredj, A. K. Davis, P. Kohl, and M. Swaminathan, “Magnetic Core Solenoid Power Inductors on Organic Substrate for System-in-Package Integrated High-Frequency Voltage Regulators,” *IEEE J. Emerg. Sel. Top. Power Electron.*, vol. 8, no. 3, pp. 2682–2695, Sep. 2020, doi: 10.1109/JESTPE.2019.2914215.

[51] M. Madsen, A. Knott, M. A. E. Andersen, and A. P. Mynster, “Printed circuit board embedded inductors for very high frequency Switch-Mode Power Supplies,” in *2013 IEEE ECCE Asia Downunder*, Jun. 2013, pp. 1071–1078. doi: 10.1109/ECCE-Asia.2013.6579241.

[52] M. L. F. Bellaredj, A. K. Davis, P. Kohl, M. Swaminathan, and S. Sandler, “Design, Fabrication, and Characterization of Package Embedded Solenoidal Magnetic Core Inductors for High-Efficiency System-In-Package Integrated Voltage Regulators,” *IEEE Trans. Magn.*, vol. 55, no. 7, pp. 1–7, Jul. 2019, doi: 10.1109/TMAG.2019.2901780.

[53] C. H. Ahn, Y. J. Kim, and M. G. Allen, “A fully integrated planar toroidal inductor with a micromachined nickel-iron magnetic bar,” *IEEE Trans. Compon. Packag. Manuf. Technol. Part A*, vol. 17, no. 3, pp. 463–469, Sep. 1994, doi: 10.1109/95.311757.

[54] Y. Gu, D. Park, D. Bowen, S. Das, and D. R. Hines, “Direct-Write Printed, Solid-Core Solenoid Inductors with Commercially Relevant Inductances,” *Adv. Mater. Technol.*, vol. 4, no. 1, p. 1800312, 2019, doi: 10.1002/admt.201800312.

[55] Y. Yan, J. Moss, K. D. T. Ngo, Y. Mei, and G.-Q. Lu, “Additive Manufacturing of Toroid Inductor for Power Electronics Applications,” *IEEE Trans. Ind. Appl.*, vol. 53, no. 6, pp. 5709–5714, Nov. 2017, doi: 10.1109/TIA.2017.2729504.

[56] Y. Wang, F. Castles, and P. S. Grant, “3D Printing of NiZn ferrite/ABS Magnetic Composites for Electromagnetic Devices,” *MRS Online Proc. Libr.*, vol. 1788, no. 1, pp. 29–35, Dec. 2015, doi: 10.1557/opl.2015.661.

[57] L. M. Bollig, P. J. Hilpisch, G. S. Mowry, and B. B. Nelson-Cheeseman, “3D printed magnetic polymer composite transformers,” *J. Magn. Magn. Mater.*, vol. 442, pp. 97–101, Nov. 2017, doi: 10.1016/j.jmmm.2017.06.070.

[58] B. J. Kang, C. K. Lee, and J. H. Oh, “All-inkjet-printed electrical components and circuit fabrication on a plastic substrate,” *Microelectron. Eng.*, vol. 97, pp. 251–254, Sep. 2012, doi: 10.1016/j.mee.2012.03.032.

[59] E. J. Brandon, E. E. Wesseling, V. Chang, and W. B. Kuhn, “Printed microinductors on flexible substrates for power applications,” *IEEE Trans. Compon. Packag. Technol.*, vol. 26, no. 3, pp. 517–523, Sep. 2003, doi: 10.1109/TCAPT.2003.817641.

[60] M. Vaseem, F. A. Ghaffar, M. F. Farooqui, and A. Shamim, “Iron Oxide Nanoparticle-Based Magnetic Ink Development for Fully Printed Tunable Radio-Frequency Devices,” *Adv. Mater. Technol.*, vol. 3, no. 4, p. 1700242, 2018, doi: 10.1002/admt.201700242.

[61] M. Bissannagari and J. Kim, “Inkjet printing of NiZn-ferrite films and their magnetic properties,” *Ceram. Int.*, vol. 41, no. 6, pp. 8023–8027, Jul. 2015, doi: 10.1016/j.ceramint.2015.02.151.

[62] M. L. F. Bellaredj, S. Mueller, A. K. Davis, P. Kohl, M. Swaminathan, and Y. Mano, “Fabrication, Characterization and Comparison of FR4-Compatible Composite Magnetic Materials for High Efficiency Integrated Voltage Regulators with Embedded Magnetic Core Micro-Inductors,” in *2017 IEEE 67th Electronic Components and Technology Conference (ECTC)*, May 2017, pp. 2008–2014. doi: 10.1109/ECTC.2017.187.

[63] Y. Yan, C. Ding, K. D. T. Ngo, Y. Mei, and G.-Q. Lu, “Additive manufacturing of planar inductor for Power Electronics applications,” in *2016 International Symposium on 3D Power Electronics Integration and Manufacturing (3D-PEIM)*, Jun. 2016, pp. 1–16. doi: 10.1109/3DPEIM.2016.7570536.

[64] L. Liu, T. Ge, Y. Yan, K. D. T. Ngo, and G.-Q. Lu, “UV-assisted 3D-printing of soft ferrite magnetic components for power electronics integration,” in *2017 International Conference on Electronics Packaging (ICEP)*, Apr. 2017, pp. 447–450. doi: 10.23919/ICEP.2017.7939416.

[65] A. Hodaei *et al.*, “Single Additive Enables 3D Printing of Highly Loaded Iron Oxide Suspensions,” *ACS Appl. Mater. Interfaces*, vol. 10, no. 11, pp. 9873–9881, Mar. 2018, doi: 10.1021/acsami.8b00551.

[66] C. Huber *et al.*, “3D Printing of Polymer-Bonded Rare-Earth Magnets With a Variable Magnetic Compound Fraction for a Predefined Stray Field,” *Sci. Rep.*, vol. 7, p. 9419, Aug. 2017, doi: 10.1038/s41598-017-09864-0.

[67] Q. Shi *et al.*, “Permalloy/polydimethylsiloxane nanocomposite inks for multimaterial direct ink writing of gigahertz electromagnetic structures,” *J. Mater. Chem. C*, vol. 8, no. 43, pp. 15099–15104, Nov. 2020, doi: 10.1039/D0TC03244A.

[68] P. F. Flowers, C. Reyes, S. Ye, M. J. Kim, and B. J. Wiley, “3D printing electronic components and circuits with conductive thermoplastic filament,” *Addit. Manuf.*, vol. 18, pp. 156–163, Dec. 2017, doi: 10.1016/j.addma.2017.10.002.

[69] C. Yi *et al.*, “Fully printed resonance-free broadband conical inductors using engineered magnetic inks,” *Addit. Manuf.*, vol. 44, p. 102034, Aug. 2021, doi: 10.1016/j.addma.2021.102034.

[70] T. C. Choy, *Effective Medium Theory: Principles and Applications*, Second Edition, Second Edition. in International Series of Monographs on Physics. Oxford, New York: Oxford University Press, 2016.

[71] J. Yuan, C.-F. Li, Z.-Q. Liu, D. Wu, and L. Cao, “Synthesis of variously shaped magnetic FeCo nanoparticles and the growth mechanism of FeCo nanocubes,” *CrystEngComm*, vol. 19, no. 43, pp. 6506–6515, Nov. 2017, doi: 10.1039/C7CE01353A.

[72] G. W. Qin *et al.*, “Ni80Fe20 permalloy nanoparticles: Wet chemical preparation, size control and their dynamic permeability characteristics when composited with Fe micron particles,” *J. Magn. Magn. Mater.*, vol. 321, no. 24, pp. 4057–4062, Dec. 2009, doi: 10.1016/j.jmmm.2009.08.004.

[73] “NEA 121.” https://www.norlandprod.com/adhesives/nea%20121.html (accessed May 12, 2023).

[74] Y. Liu, X.-Y. Zhao, Y.-G. Sun, W.-Z. Li, X.-S. Zhang, and J. Luan, “Synthesis and applications of low dielectric polyimide,” *Resour. Chem. Mater.*, vol. 2, no. 1, pp. 49–62, Mar. 2023, doi: 10.1016/j.recm.2022.08.001.

[75] P. K. Sharma, N. Gupta, and P. I. Dankov, “Analysis of Dielectric Properties of Polydimethylsiloxane (PDMS) as a Flexible Substrate for Sensors and Antenna Applications,” *IEEE Sens. J.*, vol. 21, no. 17, pp. 19492–19504, Sep. 2021, doi: 10.1109/JSEN.2021.3089827.

[76] S.-M. Jang, H.-J. Seo, Y.-S. Park, H.-I. Park, and J.-Y. Choi, “Design and Electromagnetic Field Characteristic Analysis of 1.5 kW Small Scale Wind Power Generator for Substitution of Nd-Fe-B to Ferrite Permanent Magnet,” *IEEE Trans. Magn.*, vol. 48, no. 11, pp. 2933–2936, Nov. 2012, doi: 10.1109/TMAG.2012.2203111.

[77] O. Gutfleisch, M. A. Willard, E. Brück, C. H. Chen, S. G. Sankar, and J. P. Liu, “Magnetic Materials and Devices for the 21st Century: Stronger, Lighter, and More Energy Efficient,” *Adv. Mater.*, vol. 23, no. 7, pp. 821–842, 2011, doi: 10.1002/adma.201002180.

[78] X. Wei, M.-L. Jin, H. Yang, X.-X. Wang, Y.-Z. Long, and Z. Chen, “Advances in 3D printing of magnetic materials: Fabrication, properties, and their

applications," *J. Adv. Ceram.*, vol. 11, no. 5, pp. 665–701, May 2022, doi: 10.1007/s40145-022-0567-5.

[79] H. Wang, T. N. Lamichhane, and M. P. Paranthaman, "Review of additive manufacturing of permanent magnets for electrical machines: A prospective on wind turbine," *Mater. Today Phys.*, vol. 24, p. 100675, May 2022, doi: 10.1016/j.mtphys.2022.100675.

[80] C. Huber *et al.*, "3D print of polymer bonded rare-earth magnets, and 3D magnetic field scanning with an end-user 3D printer," *Appl. Phys. Lett.*, vol. 109, no. 16, p. 162401, Oct. 2016, doi: 10.1063/1.4964856.

[81] J. Laureto, J. Tomasi, J. A. King, and J. M. Pearce, "Thermal properties of 3-D printed polylactic acid-metal composites," *Prog. Addit. Manuf.*, vol. 2, no. 1, pp. 57–71, Jun. 2017, doi: 10.1007/s40964-017-0019-x.

[82] Y. Kim, H. Yuk, R. Zhao, S. A. Chester, and X. Zhao, "Printing ferromagnetic domains for untethered fast-transforming soft materials," *Nature*, vol. 558, no. 7709, Art. no. 7709, Jun. 2018, doi: 10.1038/s41586-018-0185-0.

[83] J. Cesarano, "A Review of Robocasting Technology," *MRS Online Proc. Libr.*, vol. 542, no. 1, pp. 133–139, Dec. 1998, doi: 10.1557/PROC-542-133.

[84] L. M. Rueschhoff, W. J. Costakis, M. Michie, J. P. Youngblood, and R. W. Trice, "Additive Manufacturing of Dense Ceramic Parts via Direct Ink Writing of Aqueous Alumina Suspensions," *Int. J. Appl. Ceram. Technol.*, vol. 13, no. 5, pp. 821–830, Sep. 2016, doi: 10.1111/ijac.12557.

[85] Y. Hirata, "Theoretical aspects of colloidal processing," *Ceram. Int.*, vol. 23, no. 1, pp. 93–98, Jan. 1997, doi: 10.1016/0272-8842(95)00144-1.

[86] M. Guvendiren, H. D. Lu, and J. A. Burdick, "Shear-thinning hydrogels for biomedical applications," *Soft Matter*, vol. 8, no. 2, pp. 260–272, Dec. 2011, doi: 10.1039/C1SM06513K.

[87] Q. Li and J. a. Lewis, "Nanoparticle Inks for Directed Assembly of Three-Dimensional Periodic Structures," *Adv. Mater.*, vol. 15, no. 19, pp. 1639–1643, 2003, doi: 10.1002/adma.200305413.

[88] J. E. Smay, J. Cesarano, and J. A. Lewis, "Colloidal Inks for Directed Assembly of 3-D Periodic Structures," *Langmuir*, vol. 18, no. 14, pp. 5429–5437, Jul. 2002, doi: 10.1021/la0257135.

[89] A. Kondo, H. Xu, H. Abe, and M. Naito, "Thermoresponsive gelling behavior of concentrated alumina suspensions containing poly(acrylic acid) and PEO–PPO–PEO copolymer," *J. Colloid Interface Sci.*, vol. 373, no. 1, pp. 20–26, May 2012, doi: 10.1016/j.jcis.2011.09.071.

[90] J. Cesarano Iii and I. A. Aksay, "Processing of Highly Concentrated Aqueous α-Alumina Suspensions Stabilized with Polyelectrolytes," *J. Am. Ceram. Soc.*, vol. 71, no. 12, pp. 1062–1067, 1988, doi: 10.1111/j.1151-2916.1988.tb05792.x.

[91] J. Cesarano Iii, I. A. Aksay, and A. Bleier, "Stability of Aqueous α-Al2O3 Suspensions with Poly(methacrylic acid) Polyelectrolyte," *J. Am. Ceram. Soc.*, vol. 71, no. 4, pp. 250–255, 1988, doi: 10.1111/j.1151-2916.1988.tb05855.x.

[92] J. A. Lewis, "Colloidal processing of ceramics," *J. Am. Chem. Soc.*, vol. 83, no. 10, pp. 2341–2359, 2000, doi: 10.1111/j.1151-2916.2000.tb01560.x.

[93] S. Asakura and F. Oosawa, “On Interaction between Two Bodies Immersed in a Solution of Macromolecules,” *J. Chem. Phys.*, vol. 22, pp. 1255–1256, Jul. 1954, doi: 10.1063/1.1740347.

[94] L.-C. Guo, Y. Zhang, N. Uchida, and K. Uematsu, “Adsorption Effects on the Rheological Properties of Aqueous Alumina Suspensions with Polyelectrolyte,” *J. Am. Ceram. Soc.*, vol. 81, no. 3, pp. 549–556, 1998, doi: 10.1111/j.1151-2916.1998.tb02373.x.

[95] J. A. Lewis, “Direct-write assembly of ceramics from colloidal inks,” *Curr. Opin. Solid State Mater. Sci.*, vol. 6, no. 3, pp. 245–250, Jun. 2002, doi: 10.1016/S1359-0286(02)00031-1.

[96] L. M. Sanchez, D. A. Martin, V. A. Alvarez, and J. S. Gonzalez, “Polyacrylic acid-coated iron oxide magnetic nanoparticles: The polymer molecular weight influence,” *Colloids Surf. Physicochem. Eng. Asp.*, vol. 543, pp. 28–37, Apr. 2018, doi: 10.1016/j.colsurfa.2018.01.050.

[97] M. Acosta, V. L. Wiesner, C. J. Martinez, R. W. Trice, and J. P. Youngblood, “Effect of Polyvinylpyrrolidone Additions on the Rheology of Aqueous, Highly Loaded Alumina Suspensions,” *J. Am. Ceram. Soc.*, vol. 96, no. 5, pp. 1372–1382, 2013, doi: 10.1111/jace.12277.

[98] P. Jenkins and M. Snowden, “Depletion flocculation in colloidal dispersions,” *Adv. Colloid Interface Sci.*, vol. 68, pp. 57–96, Nov. 1996, doi: 10.1016/S0001-8686(96)90046-9.

[99] G. M. Harrison and D. V. Boger, “Well-Characterized Low Viscosity Elastic Liquids,” *Appl. Rheol.*, vol. 10, no. 4, pp. 166–177, Aug. 2000, doi: 10.1515/arh-2000-0010.

[100] S. Sur and J. Rothstein, “Drop breakup dynamics of dilute polymer solutions: Effect of molecular weight, concentration, and viscosity,” *J. Rheol.*, vol. 62, no. 5, pp. 1245–1259, Sep. 2018, doi: 10.1122/1.5038000.

[101] N. Ashrafi *et al.*, “Magnetic, Electrical, and Physical Properties Evolution in Fe3O4 Nanofiller Reinforced Aluminium Matrix Composite Produced by Powder Metallurgy Method,” *Materials*, vol. 15, no. 12, Art. no. 12, Jan. 2022, doi: 10.3390/ma15124153.

[102] K. Sun *et al.*, “Optimizing the Soft Magnetic Properties of Mn-Zn Ferrite by a Proper Control of Sintering Process,” *J. Electron. Mater.*, vol. 50, no. 3, pp. 1467–1473, Mar. 2021, doi: 10.1007/s11664-020-08700-y.

[103] A. Verma and R. Chatterjee, “Effect of zinc concentration on the structural, electrical and magnetic properties of mixed Mn–Zn and Ni–Zn ferrites synthesized by the citrate precursor technique,” *J. Magn. Magn. Mater.*, vol. 306, no. 2, pp. 313–320, Nov. 2006, doi: 10.1016/j.jmmm.2006.03.033.

[104] B. Antic, A. Kremenović, A. S. Nikolic, and M. Stoiljkovic, “Cation Distribution and Size-Strain Microstructure Analysis in Ultrafine Zn−Mn Ferrites Obtained from Acetylacetonato Complexes,” *J. Phys. Chem. B*, vol. 108, no. 34, pp. 12646–12651, Aug. 2004, doi: 10.1021/jp036214v.

[105] V. Baron, J. Gutzmer, H. Rundlöf, and R. Tellgren, “Neutron powder diffraction study of Mn-bearing hematite, α-Fe2−xMnxO3, in the range 0⩽x⩽0.176,” *Solid State Sci.*, vol. 7, no. 6, pp. 753–759, Jun. 2005, doi: 10.1016/j.solidstatesciences.2004.11.021.

[106] B. H. Toby and R. B. Von Dreele, “*GSAS-II* : the genesis of a modern open-source all purpose crystallography software package,” *J. Appl. Crystallogr.*, vol. 46, no. 2, pp. 544–549, Apr. 2013, doi: 10.1107/S0021889813003531.

[107] K. Kurokawa, “Power Waves and the Scattering Matrix,” *IEEE Trans. Microw. Theory Tech.*, vol. 13, no. 2, pp. 194–202, Mar. 1965, doi: 10.1109/TMTT.1965.1125964.

[108] E. M. Palmero *et al.*, “Development of permanent magnet MnAlC/polymer composites and flexible filament for bonding and 3D-printing technologies,” *Sci. Technol. Adv. Mater.*, vol. 19, no. 1, pp. 465–473, Dec. 2018, doi: 10.1080/14686996.2018.1471321.

[109] H. O. Gupta, H. Niedoba, L. J. Heyderman, I. Tomas, I. B. Puchalska, and C. Sella, “Magnetic properties and domain structure studies in dc triode-sputtered permalloy/carbon multilayer films,” *J. Appl. Phys.*, vol. 69, no. 8, pp. 4529–4531, Apr. 1991, doi: 10.1063/1.348349.

[110] G. W. Qin, F. Darain, H. Wang, and K. Dimitrov, “Surface modification of permalloy (Ni80Fe20) nanoparticles for biomedical applications,” *J. Nanoparticle Res.*, vol. 13, no. 1, pp. 45–51, Jan. 2011, doi: 10.1007/s11051-010-0101-5.

[111] D. T. Nguyen *et al.*, “3D-Printed Transparent Glass,” *Adv. Mater.*, vol. 29, no. 26, p. 1701181, 2017, doi: 10.1002/adma.201701181.

[112] J. A. Lewis, “Direct Ink Writing of 3D Functional Materials,” *Adv. Funct. Mater.*, vol. 16, no. 17, pp. 2193–2204, 2006, doi: 10.1002/adfm.200600434.

[113] W. Feng *et al.*, “Polyelectrolyte multilayer functionalized mesoporous silica nanoparticles for pH-responsive drug delivery: layer thickness-dependent release profiles and biocompatibility,” *J. Mater. Chem. B*, vol. 1, no. 43, pp. 5886–5898, Nov. 2013, doi: 10.1039/C3TB21193B.

[114] M. A. Skylar-Scott, S. Gunasekaran, and J. A. Lewis, “Laser-assisted direct ink writing of planar and 3D metal architectures,” *Proc. Natl. Acad. Sci.*, vol. 113, no. 22, pp. 6137–6142, May 2016, doi: 10.1073/pnas.1525131113.

[115] A. S. Urban, A. A. Lutich, F. D. Stefani, and J. Feldmann, “Laser Printing Single Gold Nanoparticles,” *Nano Lett.*, vol. 10, no. 12, pp. 4794–4798, Dec. 2010, doi: 10.1021/nl1030425.

[116] U. Zywietz, A. B. Evlyukhin, C. Reinhardt, and B. N. Chichkov, “Laser printing of silicon nanoparticles with resonant optical electric and magnetic responses,” *Nat. Commun.*, vol. 5, no. 1, Art. no. 1, Mar. 2014, doi: 10.1038/ncomms4402.